TECHNISCHE UNIVERSITÄT WIEN
Vienna University of Technology

Unterschrift des Betreuers

Diplomarbeit

Measurements and Irradiation Analysis of Silicon Structures for the CMS Upgrade

ausgeführt am

Institut für Hochenergiephysik
der Österreichischen Akademie der Wissenschaften
und am
Atominstitut der Österreichischen Universitäten

unter der Anleitung von

Univ.Doz. Dipl.-Ing. Dr. techn. Manfred KRAMMER
Dipl.-Ing. Dr. techn. Thomas BERGAUER

durch

Maria Bernard-Schwarz, B.Sc.

Matrikelnummer: 0725308
Wehlistrasse 154/5/17
1020 Wien

Unterschrift des Students

Wien, am _____

Kurzfassung

Bei dem sich in Genf befindlichen Teilchenbeschleuniger Large Hadron Collider LHC werden zwei Protonenstrahlen zur Kollision gebracht, um die Wechselwirkung von Elementarteilchen zu untersuchen. Nach 10 Jahren Betrieb erfolgt mit der Erhöhung der Luminosität ein Upgrade des LHCs, dass zu höherer Strahlungsbelastung der Detektoren führt. Eines der vier Hauptexperimente ist CMS. Es handelt sich dabei um einen Mehrzweckdetektor, der versucht alle Teilchen, die in der Proton-Proton Kollision entstehen, zu identifizieren. Der innerste Teil des CMS Experiments ist ein Halbleiterdetektor, der sogenannte Tracker, der die Spuren der Teilchen identifiziert. Die Lebensdauer des derzeitigen Tracker ist auf die Zeit bis zum LHC Upgrade optimiert und wird dann ersetzt.

Eine Arbeitsgruppe, die innerhalb von CMS gegründet wurde, untersucht verschiedene Detektortechnologien. Dazu wurden Wafer mit 6 inch Durchmesser bestellt um ein strahlungshartes Detektordesign für das CMS Upgrade zu ermitteln. Die Testreihe beinhaltet Sensoren als n-in-p und p-in-n Variante mit verschiedenen Dicken von 50 μm bis 320 μm. Weiters wird auch auf Unterschiede in den verschiedenen Siliziumherstellungsverfahren, wie Floating Zone, Magnetic Czochralski and Epitaxiewachstum eingegangen. Als Isolationstechnologie für die n-in-p Sensoren wird p stop und p spray getestet. Die Bestrahlung erfolgt mit Protonen und Neutronen, die der erwarteten Belastung des Upgrades entsprechen.

Diese Diplomarbeit wurde am Institut für Hochenergiephysik der Österreichischen Akademie der Wissenschaften durchgeführt. Es beinhaltet die Ergebnisse nicht bestrahlter und mit Neutronen bestrahlter Test Strukturen.

Abstract

The Large Hadron Collider LHC is a particle accelerator where two beams of protons are colliding. After 10 years of operation, LHC will be upgraded to a higher luminosity. This introduces a more severe radiation environment as it is in the current experiments. One of the main experiments is CMS which is a general purpose detector to identify any particles which are generated in the proton-proton collision. The innermost layer of the CMS detector is the tracker where the particle tracks are determined. It consists of semiconductor detectors which reach their end of lifetime when the upgrade of LHC starts.

A campaign within CMS started to investigate different technologies, where 6 inch silicon wafers were ordered to study the radiation hardness. The variety of structures under study concern sensor versions n-in-p and p-in-n in thicknesses from 50 μm to 320 μm. In terms of the sensor material the difference between floating zone, magnetic Czochralski and epitaxial grown silicon is investigated. For the n-in-p sensors also different isolation technologies, p stop and p spray, are tested. The irradiation is performed with protons and neutrons which represents the hadrons that are expected in the CMS tracker after the upgrade.

This diploma thesis was conduced at the Institute of High Energy Physics of the Austrian Academy of Sciences. It contains the measurement results of non-irradiated and neutron irradiated Test Structures.

Contents

1. The Large Hadron Collider

The choice of particles that are accelerated depends on the objective of the experiment. Hadrons have an internal structure which leads to the uncertainty which parts of the hadrons are collided. On the contrary, in a lepton collision the whole energy is transferred but there is a limitation of the energy level due to high synchrotron radiation. The Large Hadron Collider LHC is used as a discovery machine and therefore protons are colliding.

1.1. Accelerator System

Protons are extracted from hydrogen plasma and enter a linear accelerating structure first. This system consists of several electrodes interleaved by acceleration gaps. The distance between the electrodes has to increase as particles get faster. Therefore a circular accelerator, like the LHC, is needed as the linear accelerator tube would become very long. The LHC forms a ring where the particles are accelerated only at one point to reach the center of mass energy of 14 TeV. The other parts of the ring are dipole magnets for bending and quadrupole magnets for focusing or defocusing the beam. An overview of the LHC is seen in figure 1.1 a), it is sectioned into 8 important points. There are four Intersection Regions IR with the experiments, two IRs of beam collimation, the RF cavity for accelerating the protons and the beam dumping system which is part of machine protection. The total energy stored in the superconducting magnetic system is about 10 GJ to reach the magnetic field of 8 T. If the critical temperature of the superconducting magnets is exceeded, the LHC could be damaged and a beam dumping request must be transmitted within 100 μs. The communication is based on fail safe logics and is carried over fiber optic channels. A continuous signal is generated at IR6 and the beam will be dumped if an incorrect frequency of the signal is detected.

Luminosity is a key parameter of particle accelerators. The first fraction in equation 1.1 is a constant, it is either nature or fixed trough machine parameters. The second fraction is given by the intensity and the cross section. The aim is to get a very high luminosity because it represents a probability for a collision, for LHC: $L = 1 \cdot 10^{34} \cdot cm^{-2} s^{-1}$. Therefore the intensity must be as high as possible and the cross section as little as possible. The two terms beam and bunch have to be declared in this context. In case of LHC, 10^{11} protons build one bunch and several bunches are the synonym for the beam. Of these large number of particles only about 20 protons are interacting at a collision. This fact reveals the importance of luminosity.

$$L = \frac{1}{4 \cdot \pi \cdot e^2 \cdot f_0 \cdot n_b} \cdot \frac{I_{b1} \cdot I_{b2}}{\sigma_x \cdot \sigma_y} \tag{1.1}$$

f_0 ...   circumference frequency (LHC: $f_0 = 11.3 kHz$)
n_b ...   number of bunches (LHC: $n_b = 2808$)
I_{b1} ...   intensity beam1 (LHC: $I_{b1} = 0.6A$)
I_{b2} ...   intensity beam2 (LHC: $I_{b2} = 0.6A$)
σ_x ...   cross section or beam size in x (LHC: $\sigma_x = 17\mu m$)
σ_y ...   cross section or beam size in y (LHC: $\sigma_y = 17\mu m$)

1.2. Experiments

All the experiments have the same basic construction. The first layer of the detector is the tracker system where the trajectories of the particles are reconstructed. It is encased with the calorimeter where the energy of a particle is determined. A further layer is the magnet system to make it easier to distinguish different particles as Lorentz force causes different deflection. The muon spectrometer as the last basic element is needed to identify muons as they penetrate the further layers of the detector. The experiments installed at the LHC are ATLAS (A Toroidal Lhc ApparatuS) and CMS (Compact Muon Solenoid) as general-purpose detector to find any kind of new physics. This two experiments complement each other so that the search for phenomena is extended and provided corroborative. The other two main experiments are ALICE (A Large Ion Collider Experiment) which is optimized for heavy ion collisions and LHC-B (Large Hadron Collider Beauty) for precise measurements of the decay of b and anti-b quark.

The construction design of the CMS detector is seen in figure 1.1 b). The tracker consists of silicon strip detectors that are described in chapter 1.3. Scintillators are used for the electromagnetic calorimeter *ECAL* and the hadron calorimeter *HCAL*. The energy of penetrating particles can be determined because of the production of light pulses in scintillating materials. The magnet is superconducting to reach a magnetic field of 4 T. For the muon detector *MyonD* a gaseous detector is used where a signal is produced due to gas ionization.
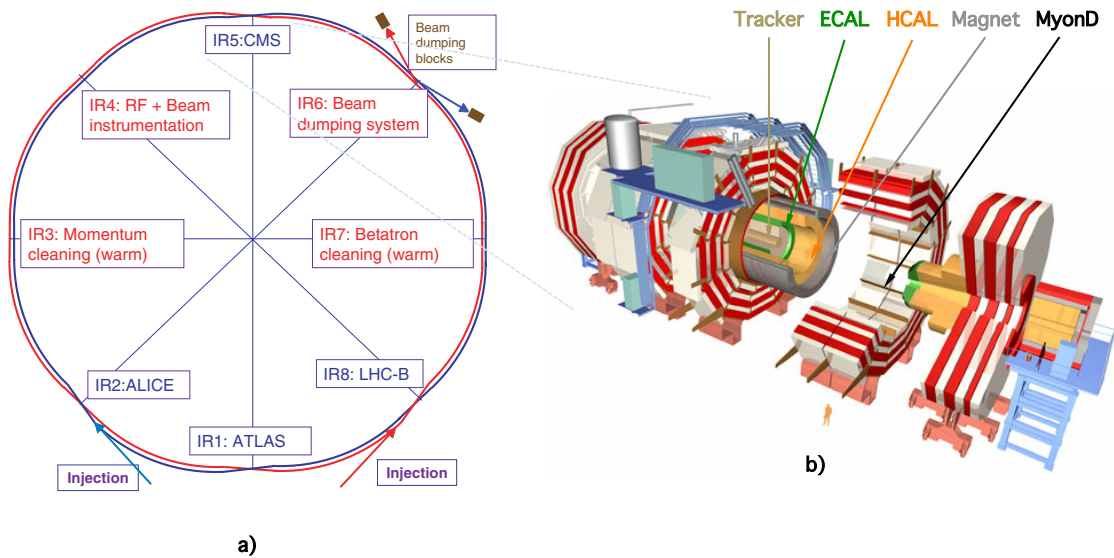

Figure 1.1.: overview of the a) LHC [1] and b) CMS detector [12]

1.3. CMS Tracker Upgrade

The current CMS tracker is the baseline for the upgrade. The silicon strip detectors are arranged in the tracker as seen in figure 1.2. The point in the center of the figure is the interaction point where the two particle beams are colliding. The innermost detector is the silicon pixel tracker in a range of 4 cm to 10 cm of radii. The silicon strip tracker includes the radii from 20 cm to 110 cm which consists of different modules with either 512 or 768 strips. There are four sub detectors defined, the Tracker Inner Barrel (TIB), the Tracker Outer Barrel (TOB), the Tracker End Caps (TEC) and the Tracker Inner Disks (TID). These sub detectors differ in the modules where for example TIB uses a 320 um thick sensor with strip pitches of 80 um to 120um whereas TOB has 500 um thick sensors with pitches from 120 um to 180 um.
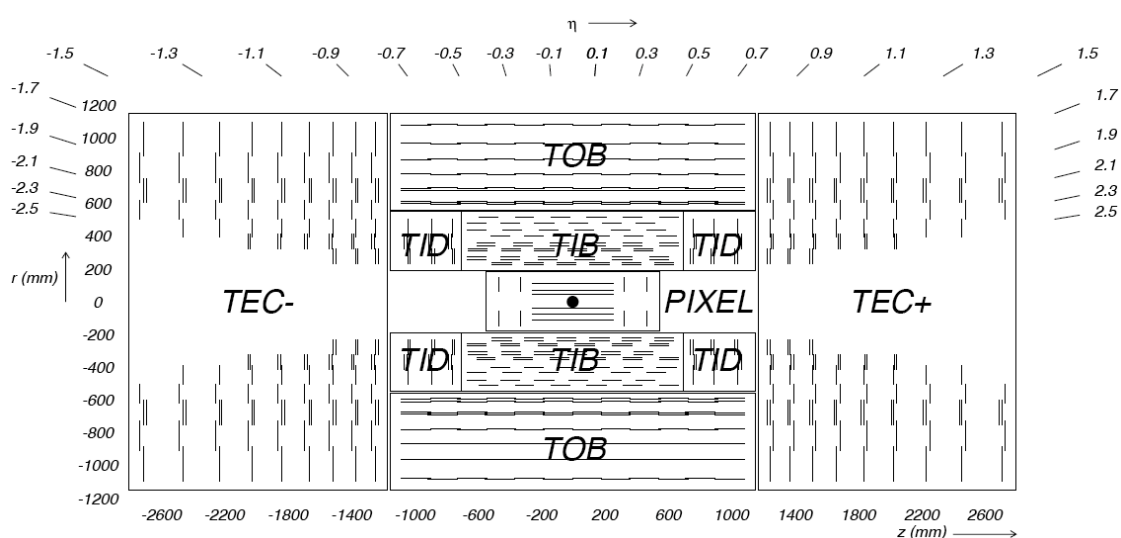

Figure 1.2.: strip sensor implementation of the current CMS tracker [4]

The luminosity upgrade of LHC will introduce an increase to $L = 5 \cdot 10^{34} \cdot cm^{-2} s^{-1}$ whereas the center-of-mass energy of 14 TeV will be the same. An exchange of the magnet system or a larger circumference of the LHC were needed if the energy would be also increased. The number of collision is expected to increase by a factor of 20 [8].

1.3.1. Tracker Specification

The higher the luminosity the higher the density of tracks which leads to more hits on a single strip. One possible solution is to increase the granularity of the strips by using shorter strips as in the current CMS experiment. This introduces further challenges for the readout electronics as there are more channels to handle. All this improvements cause the need of a new powering and cooling system. The challenge for powering is to reduce heat losses of existing supply cables and cooling has to be more efficient with the constrains of reducing the mass of cooling pipes.

1.3.2. Sensor Specification

The current strip detector in the CMS tracker reaches the end of lifetime when radiation damage increases the full depletion voltage to the maximum voltage of the power supply. With higher luminosity the hadron and neutron fluxes increases significantly. The fluence depends on the different radii from the interaction point which has to be taken into account when investigating the material. The expected fluence of inner layers is about $10^{16} \cdot n_{eq} \cdot cm^{-2}$ whereas for the outer layer it is about $10^{14} \cdot n_{eq} \cdot cm^{-2}$ [4], where n_{eq} refers to the equivalent damage of 1 MeV neutrons.

The Central European Consortium CEC is a collaboration of several research institutes which was formed to construct parts of the new CMS tracker. For the sensor design, 6 inch silicon wafers were ordered from Hamamatsu Photonics K.K. (HPK) to answer question like radiation tolerance and annealing behavior of different silicon materials. The technology decision is deduced from the irradiation with protons and neutrons. An overview of the investigated materials is shown in table 1.1. The letters refer to the detector type where N means n bulk, Y means p bulk with p-spray and P with p-stop. A second metallization layer (2nd metal) indicates direct routing on the detector whereas otherwise pitch adapters connect the detector and readout electronic. In this thesis the electrical measurements of test structures are presented where the results lead to characteristics of the manufacturing process. The set of different test structures, as indicated with TS_1 in figure 1.3, is called Halfmoon in the following. The wafer cut has a similar shape of a halfmoon and therefore this abbreviation has been chosen.

There is a consistent labeling of wafers. An example of the Halfmoon labeling is FZ320N_01_TS_1, where the first letters refer to the bulk material (FZ, MCZ, Epi), the digits to the thickness of the wafer (320, 200, 120, 100, 50). Then the bulk type is stated by N, P or Y. After the first underline, the wafer number is declared, after the second one the type corresponding to the wafer cut is specified. In this case it is TS which stands for Test Structure. There are always two Halfmoons on the wafer specified by the digit after the third underline. The upper left TS refers to 1 and the lower right one to 2, which is indicated in figure 1.3.

	FZ 320um	FZ 200um	FZ 120um	MCZ 200um	epi 100um	epi 50um
N	x	x	x	x	x	x
Y	x	x	x	x	x	x
P	x	x	x	x	x	x
2nd metal N		x				
2nd metal Y		x				
2nd metal P		x				

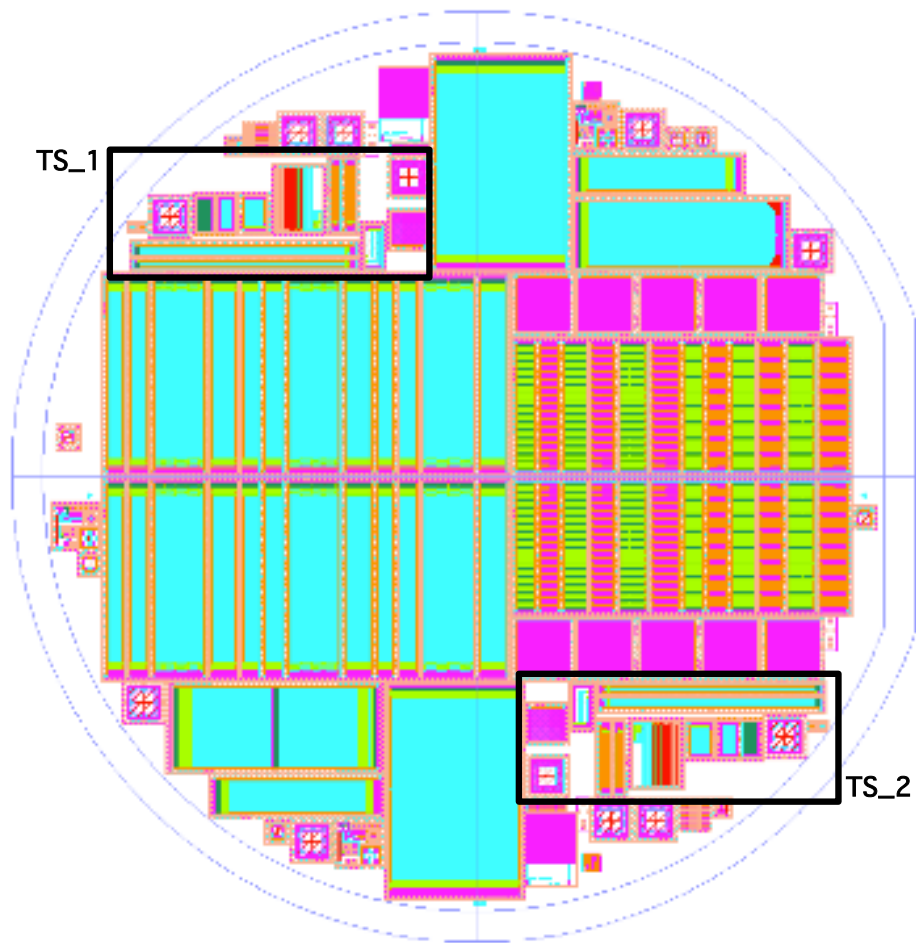**Table 1.1.:** overview of investigated sensor technologies

Figure 1.3.: overview of the silicon wafer from HPK [4]

2. Semiconductor Detector

In high energy physics semiconductor detectors are usually used to determine tracks, momentum and charge of particles. The advantages are a low mean ionization energy, no need of cryogenic temperatures, high radiation tolerance compared to gaseous detectors and a fast signal response.

2.1. Working Principle

The structure of a semiconductor detector is shown in figure 2.1. It mainly consists of three layers, a bulk material and two electrodes. The bulk refers to a doped semiconductor, the electrodes to a highly doped one which is marked with p+ and n+. Aluminum Al is used for the electrical contact. The bulk has to be depleted of intrinsic charge carriers and therefore a voltage in the reverse direction of the p-n junction is applied. If a particle, indicated with the orange arrow, passes through the bulk, electrons and holes are generated. A signal at the electrodes is generated due to the drift of the electrons to the n+ layer and the holes to the p+ layer. In this example tracking is possible, as the p+ layer is segmented. Amplifier and readout electronics are connected to the aluminum with so called DC pads as there is a direct connection with the p+ layer. Capacitances are needed before amplifying because the reverse current of the p+ strips would flow directly to the readout electronics.
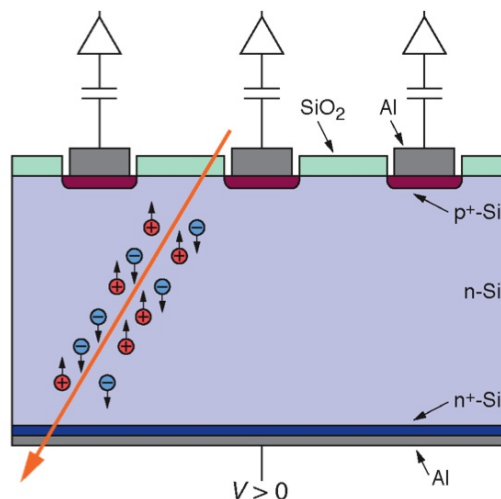

Figure 2.1.: principle of a semiconductor detector [2]

A detailed lateral cut of a semiconductor detector is seen figure 2.2 where the readout strip correspond to the so called AC pad. In this case the coupling capacitance is already implemented during processing with an additional SiO_2 between the p+ and aluminum. The three terms polysilicon resistor, bias line and guard rings have to be explained. At the bias line the needed depletion voltage is applied. The polysilicon resistor connects the p+ strips with the bias line which should have a high resistance value for isolating each strip from each other. The guard rings are additional p+ layers as cutting the wafer causes imperfection in the crystal and this introduces a dark current. In other applications guard rings are responsible to form the electric field and then a connection with a certain potential would be necessary.

The spatial resolution of a silicon strip detector is within μm. The concept of intermediate strips is used to improve spatial resolution. Diffusion influences charge carriers near the electrodes less than the charge carriers near the point of generation, as they need more time to drift. Therefore the more strips, which means the distance between strips is less, the better the spatial resolution. At intermediate strips no readout electronic is connected directly. If a signal is generated, it is transmitted via capacitive coupling to the readout strips.
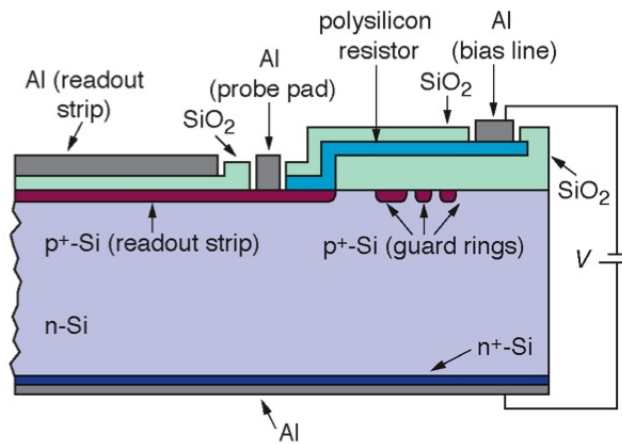

Figure 2.2.: lateral cut of a semiconductor detector [2]

The standard material, which is used for the current CMS experiment, is a p-in-n semiconductor detector. This means that p+ strips are used with a n bulk material, whereas n-in-p refers to n+ strips with a p bulk material which introduces difficulties. Between the oxide layer and the bulk material fixed oxide charges are always present. Therefore spatial resolution is not possible anymore as electrons are accumulated beneath the SiO_2 layer which is indicated in figure 2.3. To make tracking possible either p stop or p spray is used. With p stop an additional p+ layer in between the n+ strips intercept the short-cut. The pspray technology introduces p doping at the full surface of the wafer.
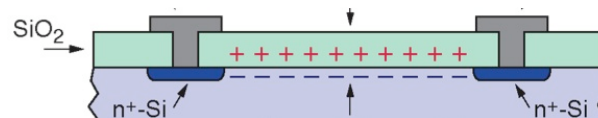

Figure 2.3.: electron accumulation beneath fixed oxide charges [2]

2.2. Manufacturing Process

Silicon is gained from silicon dioxide which is melted to liquid silicon with a purity of 99%. After physical and chemical processes a purity of 0.01ppb is reached. This so called Electronic Grade Silicon has to be transformed into a single crystal by a growth technique. Silicon sensors from the following different growth techniques are investigated in this work.

Floating Zone (FZ)
The polysilicon crystal is rotated while a RF coil melts on a small region of the rod. The melted rod is in contact with a seed crystal where the silicon solidifies in a perfect single crystal. Impurities are gathered to the end. The advantage of this this growth technique is high purity.

Magnetic Czochralski (MCZ)
The Electronic Grade Silicon is melted in a crucible. A seed crystal which is mounted on a rod is rotated in the molten silicon. By controlling temperature and the rate of pulling the rod upwards a single crystal can be gained. Additionally a magnetic field is implied to minimize the mixing between the liquid in the center of the bath and with that at the edge. The advantage of this method is that the oxygen concentration can be regulated.

Epitaxial (Epi)
The method is to deposit a monocrystalline film on a monocrystalline substrate. There are mainly two different methods to gain such an epitaxial film either chemical or physical vapour deposition. The difference between them is that either a chemical reaction or a beam of particles interact with the substrate. The silicon grown epitaxial is more homogenous compared to the others processes.

Single wafers are sliced of such so called ingots. After edge rounding, surface polishing a final cleaning process, the wafer is ready for further processing. The first step of processing is the oxidation. At high temperature a SiO_2 layer is placed superficially via thermal oxidation. Photolithography and etching is used to get different elements like strips on the detector. There are two methods for doping, either ion implantation or diffusion is used. To get stable p+ layer and n+ layer the detector is annealed for a certain time and temperature, so that the dopants are on regular atomic places. In figure 2.4 boron B is used for p+ layer and arsenic As for n+ layer. The last step is the metallization where aluminum Al is added as a thin film. The methods here are either sputtering or evaporating. For structuring photolithography and etching are used again.
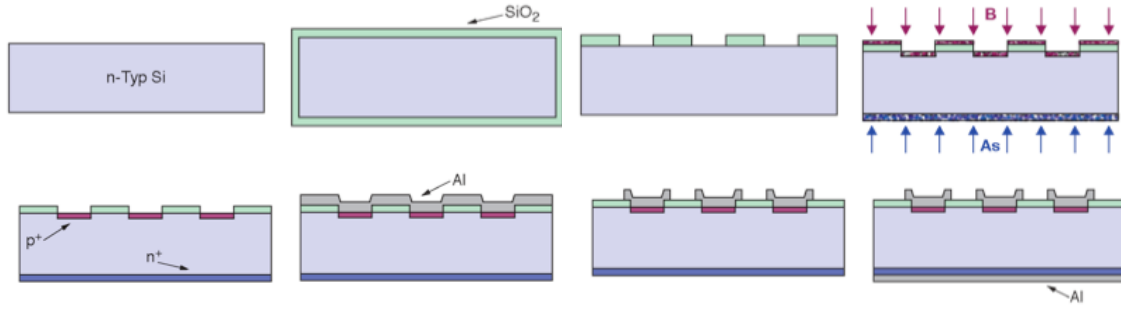
Figure 2.4.: schematic overview of manufacturing process [2]

2.3. Radiation Damage Theory

There are two damages to distinguish, surface and bulk damages. Hadrons interact with the silicon lattice and cause bulk damage whereas photons introduces defects in the oxide. Those induced charges in the oxide can not be removed easily and this leads to fixed oxide charges. The oxide capacitance increases and spatial resolution is reduced as the fixed oxide charges influence the selectivity of the readout strips. The bulk damage, like point defects, are produced from Coulomb interactions and nuclear reactions. A further source of damages is nuclear scattering where also cluster defects are generated.

2.3.1. Non Ionizing Energy Loss hypotheses

The Non Ionizing Energy Loss hypotheses NIEL is used for scaling as radiation damage depends on the particle energy, on the different kind of particles and on the different interactions. This hypotheses leads to the hardness factor which is used for the comparison of different radiation sources.
NIEL is expressed by the displacement damage cross section $D(E)$ which is seen in figure 2.5. For the calculation of $D(E)$ the probability of all possible interactions between the silicon atoms and the incoming particle with energy E is needed. The significant spectra which of interest for the inner detectors of LHC are in the MeV range. The proton damage is dominated by Coulomb interaction at lower energies and therefore $D(E)$ is higher compared to the neutron damage. For higher energies the Coulomb interaction is very small compared to the nuclear reactions and this leads to the same $D(E)$ values for protons and neutrons.

As mentioned before, the hardness factor κ is needed to compare different radiation sources. κ is defined as the ratio between the damage by a specific irradiation and the damage of 1 MeV neutrons at the same fluence $\phi(E)$ which can be calculated with equation 2.1.

$$\kappa = \frac{\int D(E) \cdot \phi(E) \cdot dE}{D(E_n = 1MeV) \cdot \int \phi(E) \cdot dE} \tag{2.1}$$
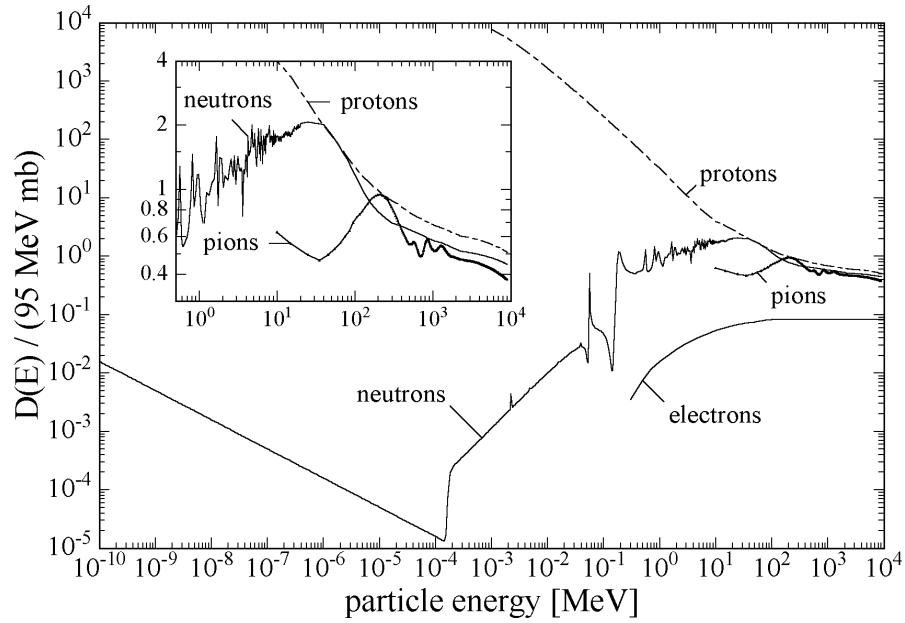
Figure 2.5.: discplacement damage cross section [5]

The parameters describing the changes of a detector are commonly scaled by the equivalent fluence of 1 MeV neutron ϕ_{eq} which can be calculated with equation 2.2.

$$\Phi_{eq} = \kappa \cdot \phi = \kappa \cdot \int \phi(E) \cdot dE \qquad (2.2)$$

2.3.2. Macroscopic Changes

There are three main macroscopic changes in the detector properties after irradiation damage, the change of depletion voltage, the decrease of Charge Collection Efficiency CCE and the increase of the dark current which is illustrated in figure 2.6. The depletion voltage is proportional to effective doping concentration N_{eff} as seen in equation 2.9 and therefore acceptor or donor like states introduce this changes. The generation and recombination of charge carriers in the depletion area cause the increase of the dark current. Trapping leads to a smaller readout signal as trapped charges are released too late. It influences CCE as it is a parameter of the collected charges after and before irradiation.
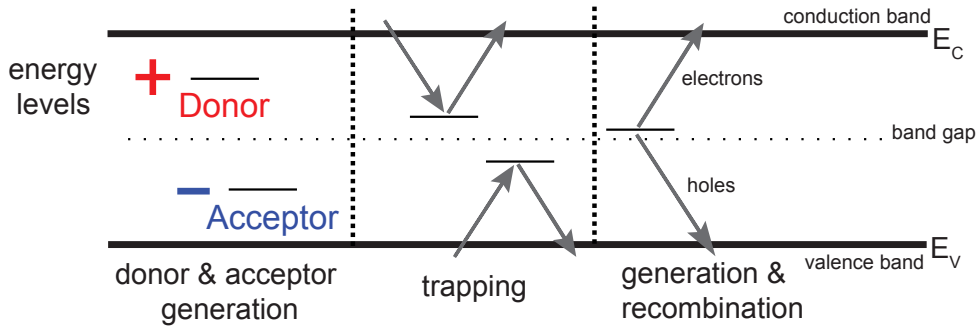
Figure 2.6.: overview of the irradiation damage in silicon [6]

The increase of the dark current depends on the fluence as given in equation 2.3 where V refers to the volume of the detector and α to the current related damage rate. The change of the dark current also depends on annealing temperature and time as defects are moveable which is taken into account with α.

$$\Delta I = \alpha \cdot \Phi_{eq} \cdot V \qquad (2.3)$$

The current related damage rate $\alpha(t)$ is calculated with equation 2.4 and the fit parameters are taken from figure 2.7. The results for different annealing temperatures is seen in figure 2.8.

$$\alpha(t) = \alpha_I \cdot exp(-\frac{t}{\tau_I}) + \alpha_0 - \beta \cdot ln(\frac{t}{t_0}) \qquad (2.4)$$

T_a [°C]	α_I 10^{-17} A/cm	τ_I [min]	α_0 10^{-17} A/cm	β 10^{-18} A/cm	t_0 [min]
21	1.23	1.4×10^4	7.07	3.29	1
49	1.28	260	5.36	3.11	1
60	1.26	94	4.87	3.16	1
80	1.13	9	4.23	2.83	1
106	–	–	3.38	2.97	1

Figure 2.7.: fit parameter for the current related damage rate (table 5.2 in [5])
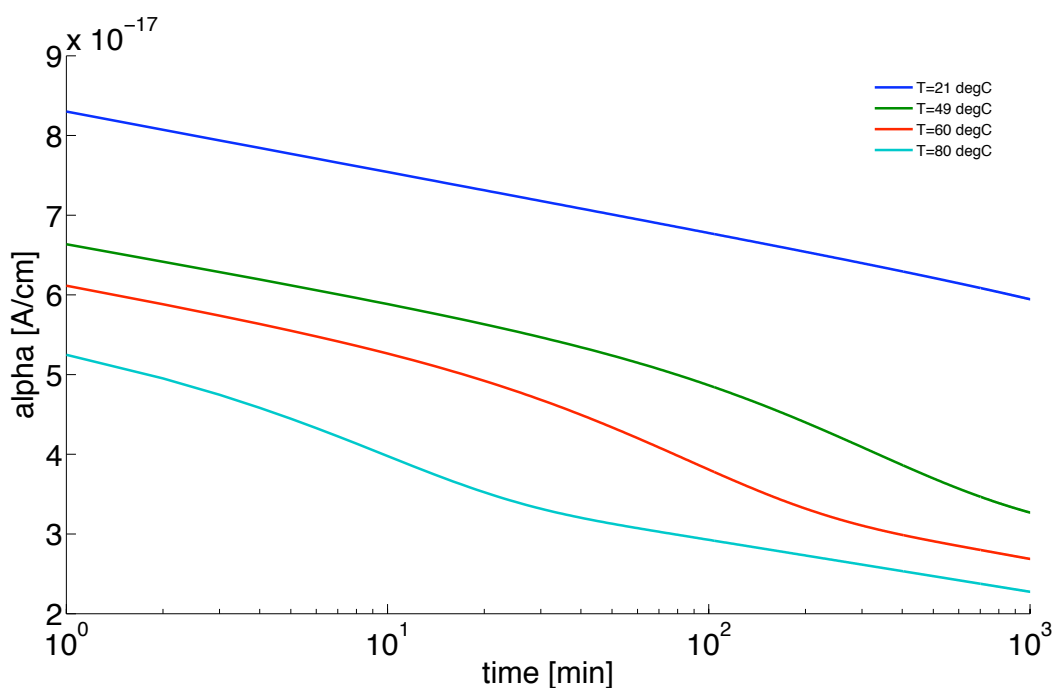
Figure 2.8.: current related damage rate α

Generally, there are two different annealing behaviors distinguished. Beneficial annealing refers to the defects that are recombined with other defects or impurities whereas new defects are built at reverse annealing. To prevent reverse annealing the temperature of the current CMS tracker has to be below 0°C all the time. For defect studying, annealing is necessary for accelerating defect migration as it may take years to follow the defects at room temperature.

The energy levels that introduces the change in N_{eff} are seen in figure 2.9. There are the nuclear reaction to an donator atom P, the deep acceptor levels H(116K), H(140K), H(151K), the donor levels E(30K) and the bistable donor BD. N_{eff} depends on the ratio between acceptors and donors. The number of donors and acceptors levels increases with irradiation where at a certain fluence, the change of the number of acceptors levels is more compared to donors. This leads to type inversion from a n bulk to a p bulk sensor.
The two main defects which are responsible for the increase of the dark current are the E5 level ($E_c - 0.5eV$) and E205a ($E_c - 0.4eV$), where E_c refers to the edge of the conduction band. These defects can be related to triplex vacancies. For trapping, only possible candidates are known so far [6].
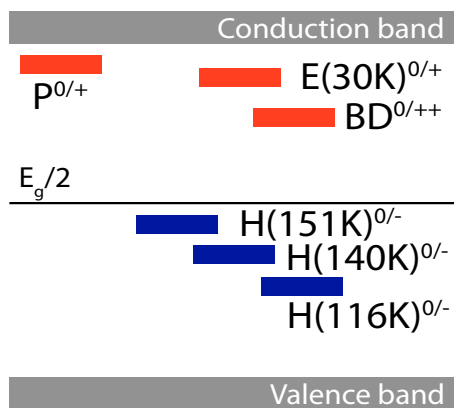
Figure 2.9.: energy levels which are responsible for the change in N_{eff} [6]

The change of the effective doping concentration N_{eff} depending on the equivalent fluence of 1 MeV neutrons is seen in figure 2.10. In case of a n bulk with p+ strips, irradiation changes the direction of the p-n junction, which is now performed with the n+ layer and the p bulk. To ensure spatial resolution, the depletion area has to reach beneath the p+ strips.
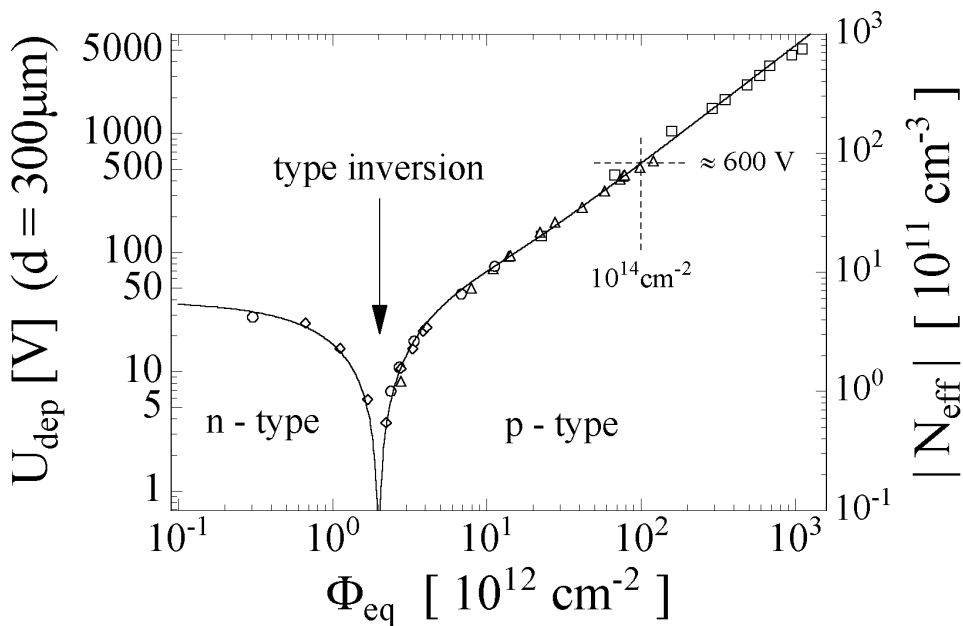

Figure 2.10.: change of the effective doping concentration after irradiation [5]

N_{eff} can be determined with equation 2.5 where N_a refers to *short term annealing*, N_y to *reverse annealing* and N_c to *stable damage*. The dependency in terms of the different annealing states is seen in figure 2.11 for an annealing temperature of $T_a = 60°C$. N_a is dominant for short time annealing, N_y starts to increase and saturates after a large time of annealing whereas N_c does not depend on annealing.

$$\Delta N_{eff}(\Phi_{eq}, t(T_a)) = N_a(\Phi_{eq}, t(T_a)) + N_y(\Phi_{eq}, t(T_a)) + N_c(\Phi_{eq}, t(T_a)) \tag{2.5}$$
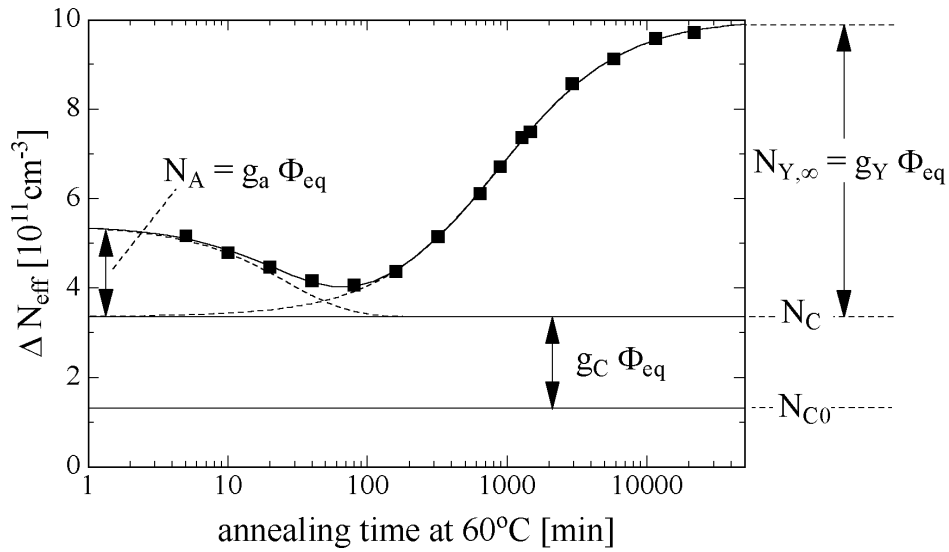

Figure 2.11.: change of the effective doping concentration depending on annealing [5]

The equations for the different annealing states of N_{eff} indicated in figure 2.11 can be used for a rough calculation. In the following, the equations for each annealing state are listed in more detail where the mean values for the fit parameters are taken from [5].

Stable damage is described with equation 2.6, the mean value for the fit parameters are $c = 1.76E\text{-}13 cm^2$, $N_{c_0} = 5.87E12 cm^{-3}$ and $g_c = 0.0149\ cm^{-1}$.

$$N_c = N_{c_0} \cdot (1 - exp(-c \cdot \Phi_{eq})) + g_c \cdot \Phi_{eq} \tag{2.6}$$

For the calculation of reverse annealing, first the reverse time constant has to be determined with $\tau_y = k_{0_y} \cdot exp(-E_y/(k_b \cdot T_a))$ where k_b refers to Boltzmann constant. N_y can be calculated with equation 2.7, the mean values are $k_{0_y} = 1.5E15 s^{-1}$, $E_y = 1.33eV$, $N_{y,\infty} = g_y \cdot \Phi_{eq}$ and $g_y = 0.0516 cm^{-1}$.

$$N_y = N_{y,\infty} \cdot \left(1 - \frac{1}{1 + (t/\tau_y)}\right) \tag{2.7}$$

Short term annealing depends exponentially on time as seen in equation 2.8 where τ_{ai} refers to the time constant parameters. For the LHC experiments annealing periods takes over years and therefore the simplified equation $N_a = g_a \cdot \Phi_{eq}$ is used commonly. The mean value of the short term annealing fit parameter is $g_a = 0.0181 cm^{-1}$.

$$N_a = \Phi_{eq} \cdot \sum_i g_{ai} \cdot exp(\frac{-t}{\tau_{ai}}) \approx g_a \cdot \Phi_{eq} \tag{2.8}$$

Apart from using fit parameters, the change of N_{eff} can also be determined with the depletion voltage U_{depl} as seen in equation 2.9 where d refers to the thickness of the sensor and e to the unit charge.

$$N_{eff} = \frac{2 \cdot U_{depl} \cdot \varepsilon_0 \cdot \varepsilon_{Si}}{e \cdot d^2} \tag{2.9}$$

The understanding of defects leads to the radiation hard design. Highly n doping causes the type inversion at a later time. The benefit of oxygen rich silicon is that the generation of the oxygen vacancy is high whereas the donor removal is suppressed.

3. Measurement Setup

A schematic overview of the measurement setup in Vienna is seen in Figure 3.1. The bias table and needles are arranged in a light tight box. The measurement equipment for the individual Test Structures on the Halfmoon are connected via a switching system. In this work the synonym cold chuck is used for the term bias table.

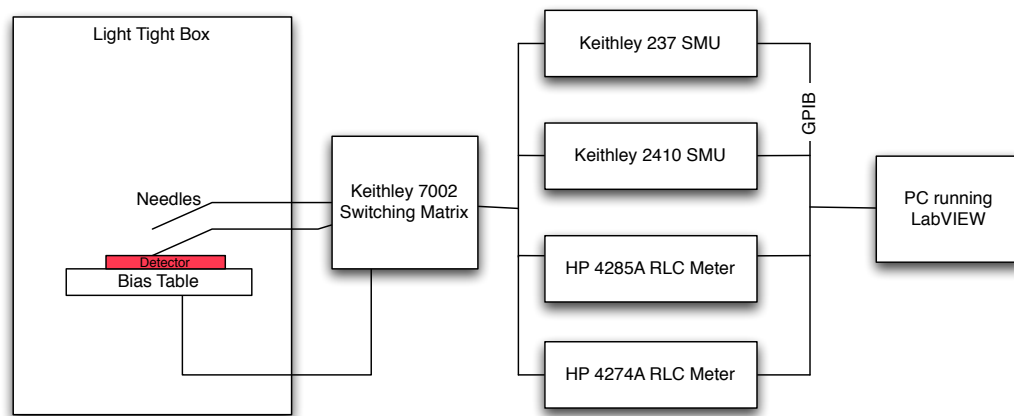More information about the setup can be found in [8].

Figure 3.1.: schematic overview of the measurement setup [8]

3.1. Cold Chuck Improvement

Measurements can be performed at different temperatures which is important for irradiation analysis as damages are made stable at low temperatures and irradiated Halfmoons can be annealed at higher temperatures.

An overview of the cold chuck design is seen in figure 3.5 where the left pictures show the layers of the cold chuck. The upper two pictures refer to the initial design. This system induces a leakage current identical to the measurement current at T=-20°C which is seen in figure 3.2.
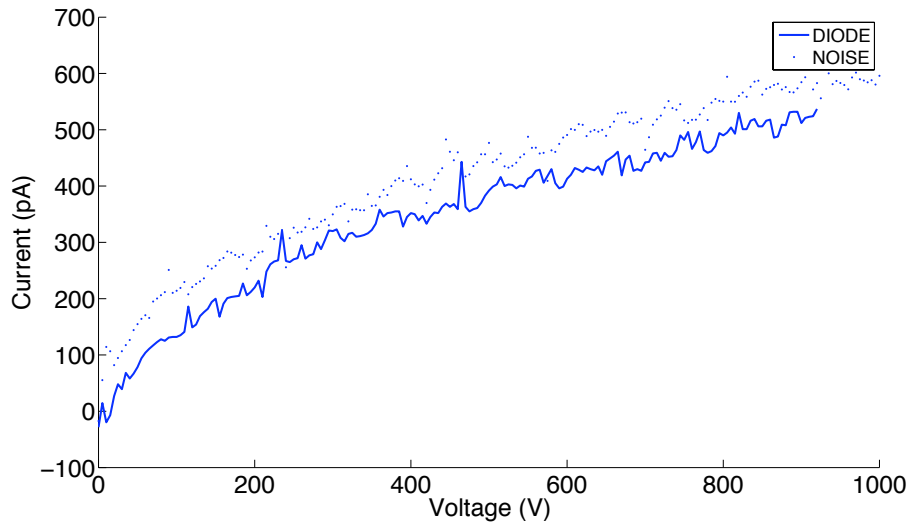
Figure 3.2.: IV of FZ diode and leakage current with the initial design, T=-20°C

This complex measurement setup introduces a lot of leakage current sources. One idea could be to isolate the cold chuck from the equipment but this does not significantly reduce the current. Unshielded cable for example are connected to the chuck which behave as antenna and even open ended connected ones introduce a leakage current.

For reducing the leakage current, everything connected to the chuck has to be on the same potential. The cables of the peltier power supply are exchanged with shielded ones, earth straps are used for the common ground connection and adhesive insulating tapes are used for ribbon cables.

For further improvements the cold chuck had to be redesigned. The initial design consisted of a thin SilPad as an insulator between two metal plates. The upper metal plate is connected with high voltage whereas the lower metal case consists of the peltier elements and water cooling. The minimum temperature of one side of the peltier elements depends on the difference in temperature and therefore an additional water cooling is needed. The problem with this chuck design is that the thin insulator introduces a high capacitance and therefore a high time constant. Every voltage step causes a change of the capacitance and therefore relaxation takes a lot of time.
So the capacitance has to be reduced with a thick insulating material which has a high thermal conductivity and a high electric isolation. An aluminum oxide (Al_2O_3) with a purity of 99.7% has a thermal conductivity of 30 W/mK and a dielectric strength of >25kV/mm [14]. The SilPad is exchanged with an aluminum oxide plate with a thickness of 2 cm. Also one of the metal cases is removed. The active Peltier side is directly connected with the aluminum oxide plate via a thermal conductance paste.

This design correspond to the center pictures in figure 3.5. The results measured with the same diode are seen in figure 3.3. The measured current is now higher but it is still influenced by the leakage current.
The unexpected source that introduces current in the pA range are the temperature sensors which

are attached to the aluminum oxide plate. The measurement principle of those sensors is that temperature changes cause frequency changes which are transmitted via rectangle pulses. The high harmonics of those pulses cause the leakage current.

For the second redesign, the advantage of triaxial cables are used. Compared to the coaxial cable, which consists of an inner conductor, an insulator, a shield and a cable coating, the triaxial cable consists of three connectors. The inner conductor is called the sense line, the additional shield is called the guard line and the third is the shielding. The problem with coaxial cable is that the insulation resistance is not ideally high and therefore a small leakage current can flow. Introducing the guard, which is on the same potential as the sense, causes the perfect isolation between sense and guard. Low currents can be measured with the sense line as any current flows between guard and shielding.

The layers of the final version is seen in the lower left pictures of figure 3.5. The plate which is connected to high voltage is separated in two parts corresponding to the triaxial connector. There is an inner plate connected to the sense which is surrounded with an outer plate corresponding to the guard. An air gap between sense and guard plate is used as insulator between them. An experimental result also shows that the leakage current can be even more reduced by using an additional metal plate corresponding to the guard. As mentioned before the temperature sensors on the Al_2O_3 plate also introduce leakage current, to reduce this source a thin SilPad is used as an insulator between the sense and guard plate. The IV behavior of the diode without the influence of a leakage current is seen in figure 3.4.
As last improvement step also the cooling water has been replaced with a SilOil (M60.115.05) as the pump is more prevented from damage due to better viscosity quality at lower temperature.

A closer look to the current range of the IV plots in figure 3.2 - 3.4 reveals that the improvement reduced the leakage current from the pA range to the fA range, so each improvement step reduced the leakage current by a factor 10. Now it is possible to measure the IV characteristic of a few pA at T=-20°C.
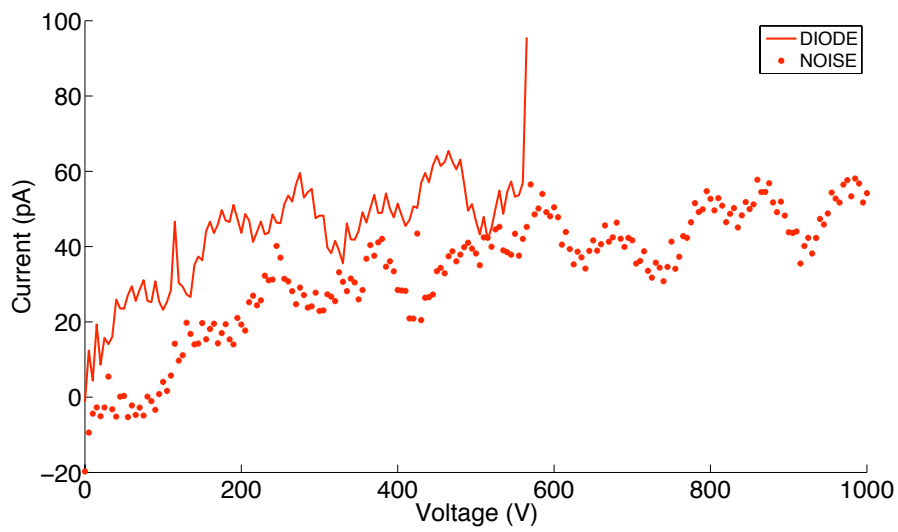The CAD drawing of the additional parts of the cold chuck are seen in appendix A.1.

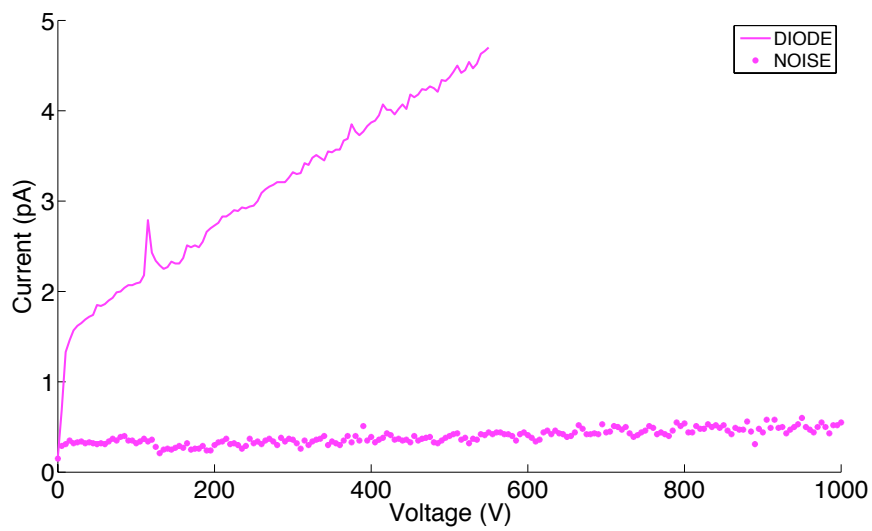**Figure 3.3.:** IV of FZ diode and leakage current with the first redesign, T=-20°C

Figure 3.4.: IV of FZ diode and leakage current with the second redesign, T=-20°C
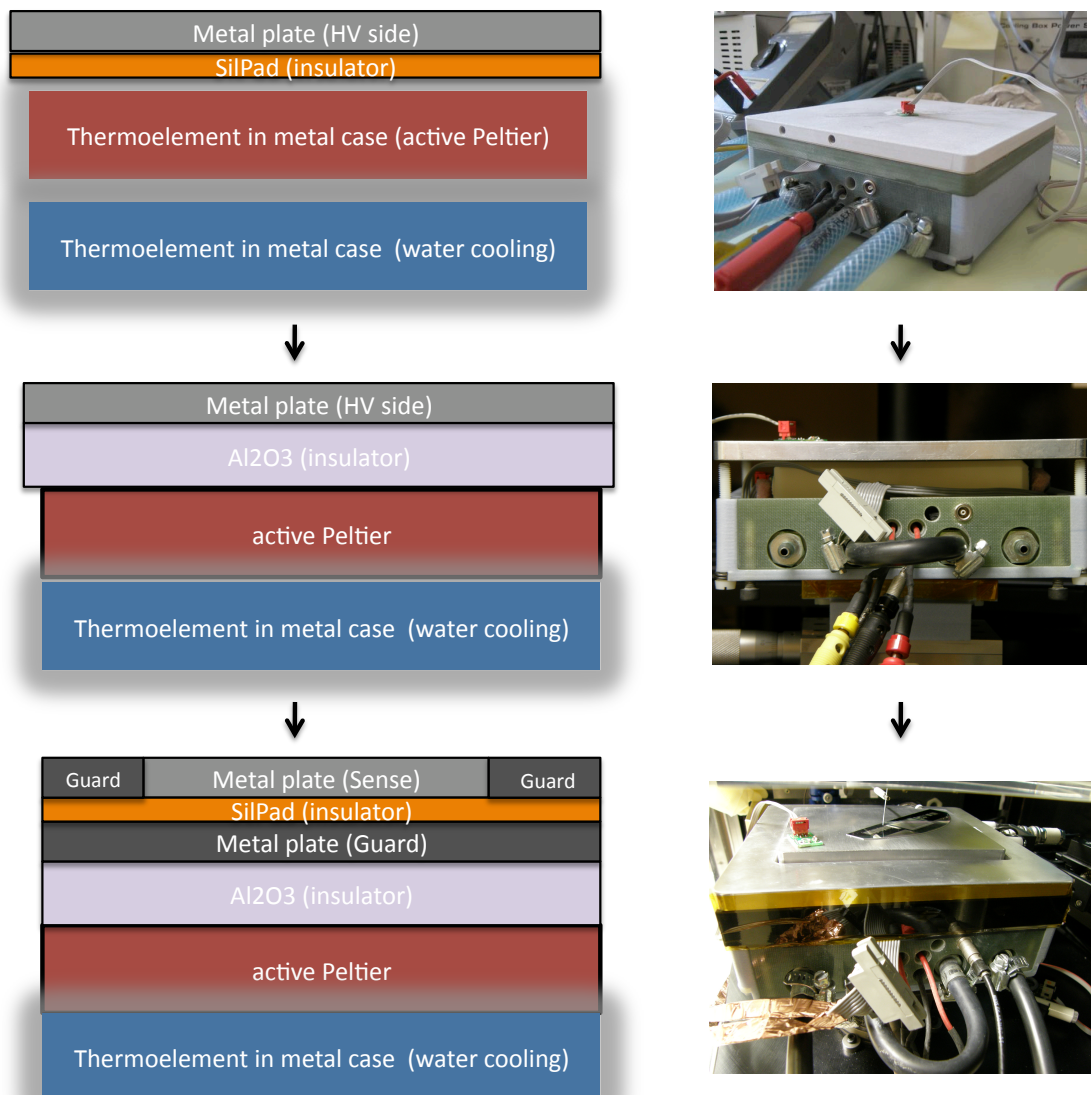
Figure 3.5.: overview of cold chuck designs

3.2. Relative Humidity and Leakage Current

Relative Humidity has still a dominant effect on the leakage current. The increasing leakage current depending on external control behavior is seen in figure 3.6. The chiller has been switched on independent of starting the pump for the liquid cooling system. Therefore the leakage current introduced electrically by the chiller has not been investigated in this measurement. The power supply of the peltier elements is also switched on all the time. The IV result leads to an open measurement where the backplane is connected to SMU high and the needle to SMU low without the matrix device. The voltage is set to 0 V and the pressure of dry air is 0.3 MPa. The four different external control condition lead to the following:

(1) RH on: only relative humidity control was switched on for RH set point = 5%
(2) RH on: only relative humidity control was switched on for RH set point = 0.01%
(3) Chiller on: additionally chiller temperature set point= -10 °C, rpm = 4400
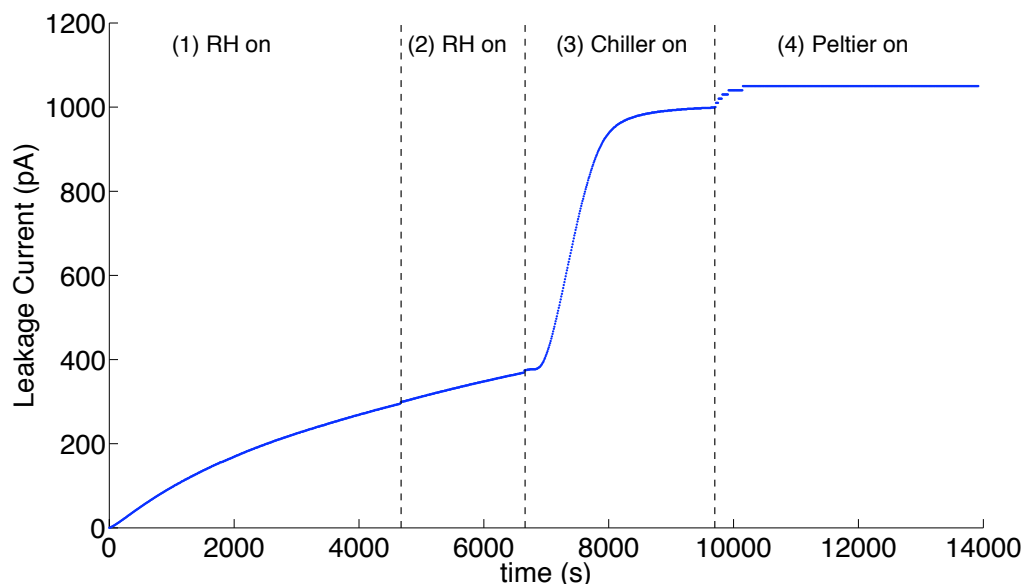(4) Peltier on: additionally temperature control set point= -20 °C

Figure 3.6.: leakage current current over time dependency

In figure 3.6 the relative humidity range is from 40% to 0.1% whereas a detail look on the dependency of the leakage current on relative humidity for each condition is seen figure 3.7. The initial leakage current value at each condition is taken as zero point. The time dependency is also seen in figure 3.7 in the decrease of relative humidity. The difference between the first and second RH control condition is that due to different temperature set points also the set point for relative humidity is different. With the temperature set point of 20 °C, the leakage current increases with decreasing relative humidity and starts to level off as the valve is switched on and off to retain the set point of 5 %. In the second condition the temperature set point is -20°C and this causes a constant dry air flow. Comparing the leakage current change in the RH range from 50 % to 5 % and in the second case from 5 % to 2 % leads to 2 pA/s for (1) and 1 pA/s for (2).

In condition (3) the pump of the Chiller has been switched on and the set point temperature of the chiller is -10 °C. The peltier elements are still switched off. The leakage current change during chiller ramping is 16 pA/s and after stable condition it reduces to 0.5 pA/s. The remarkable leakage current change of 0.01 pA/s is reached after stable conditions of the tempering elements and reaching the RH range lower 1 %.

The conclusion leading from this measurement is that a constant dry air flow at low relative humidity reduces variations in the leakage current significantly. The cold chuck design still corresponds to a low capacitance that is charged while achieving operating conditions. During charging, the leakage current increases and therefore the saturation value has to be waited for. This saturated current can be subtracted as an offset current. There are two further improvements for low temperature measurements, where the current of diodes is lower compared to room temperature. As the enclosed box behaves as a Faraday cage, some relaxation time should be waited after re-closing it. The motor control of the microscope should also be switched off as it also behaves as a leakage current source inside the box.
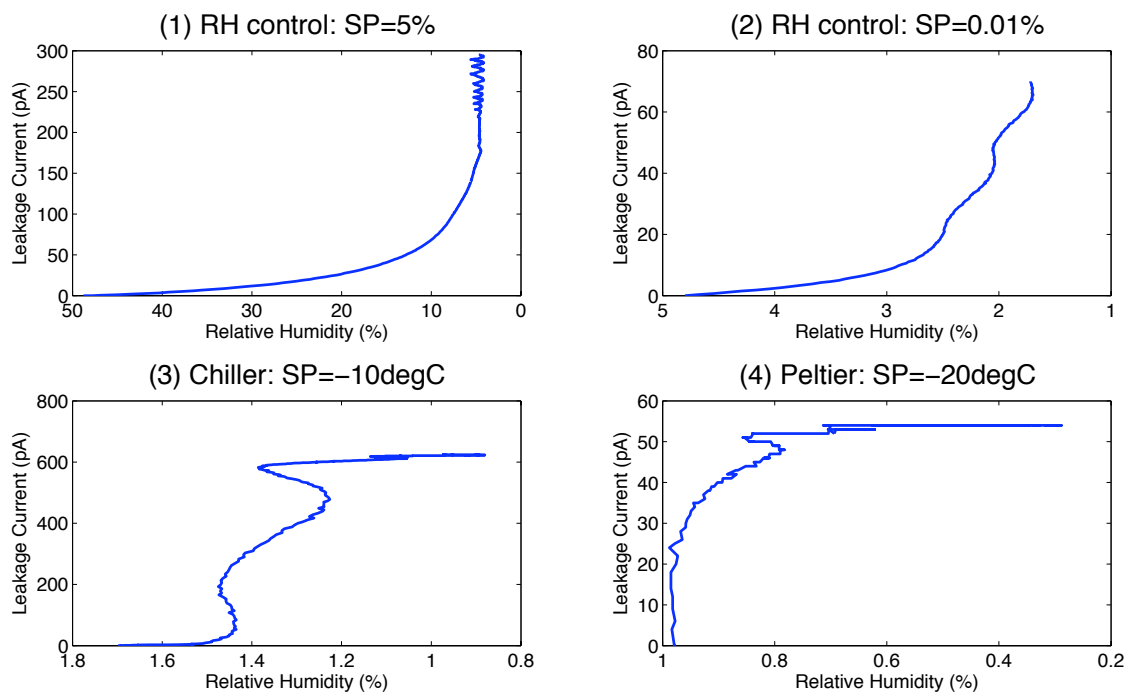

Figure 3.7.: leakage current over relative humidity dependency

3.3. Measurement Circuits

An overview of the standard CMS upgrade Halfmoon is seen in figure 3.8. It consists of several test structures leading to 10 different measurements.
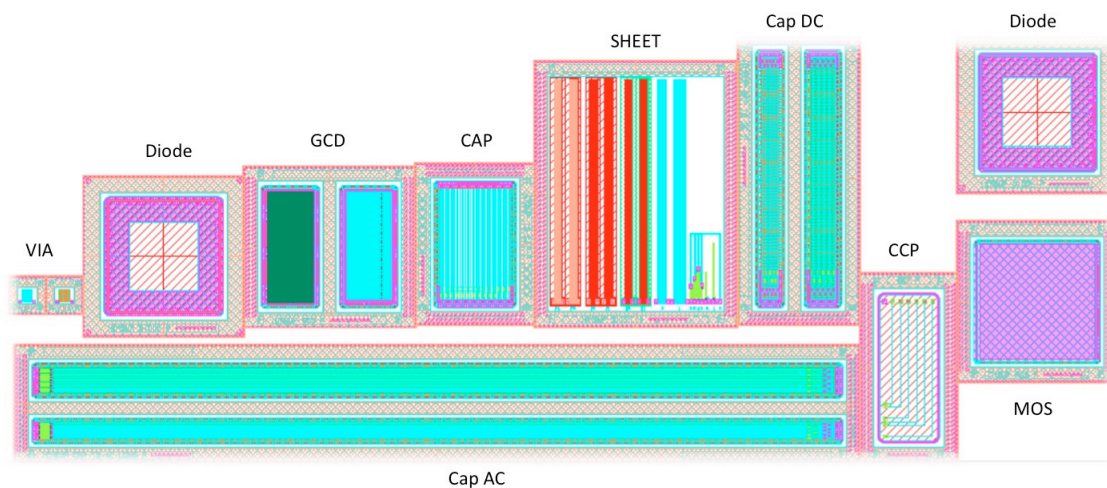

Figure 3.8.: design drawing of the CMS upgrade Halfmoon

The following subsections include an overview of all measurements. Each circuit is indicated with a design picture, a lateral sketch and a photo of the real test structure. The arrows on the photo correspond to the needles. The abbreviations listed in table 3.1 are used for the labeling of the measurement devices. A detailed information about the measurement schemes for n types is described in [3].

N1, N2, N3, N4	...	needle 1, needle 2,needle 3, needle 4
BP	...	BackPlane
HV	...	SMU 237
V	...	SMU 2410
lfLCR	...	lowfrequency LCR meter (100Hz - 100kHz)
LCR	...	LCR meter (75kHz - 30MHz)

Table 3.1.: used abbreviations for the measurement devices

3.3.1. I-V at diode

The p-n junction of the diode consists of the strip implant and the bulk material of the detector. Applying a negative bias voltage leads to the dark current of detector. The break down of the diode in reverse direction can also be determined.

Measurement parameter

Voltage Max [V]	=	700	for n type
		-700	for p type
Stepsize [V]	=	1 (for 0..10V), 5 (for 10..100V), 10 (for 100..Vmax)	for n type
		1 (for 0..-10V), 5 (for -10..-100V), 10 (for -100..Vmax)	for p type
Compliance [A]	=	10u	
Wait [ms]	=	1000	

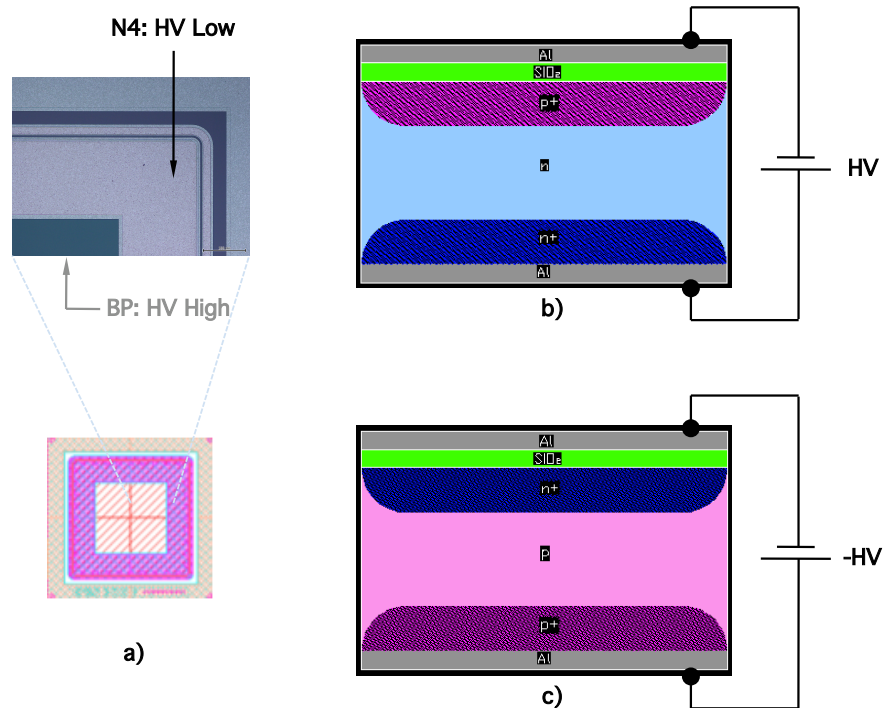**Table 3.2.:** IV diode measurement parameter

Figure 3.9.: a) schematic circuit and lateral sketches of b) N and c) P diode

3.3.2. C-V at diode

Applying a reverse bias voltage depletes the charge carriers in the bulk material. The capacitance decreases with the applied voltage until the bulk is fully depleted. The voltage value for full depletion can be extracted from the C-V plot.

Measurement parameter

Voltage Max [V]	=	700	for n type
		-700	for p type
Stepsize [V]	=	1 (for 0..10V), 5 (for 10..100V), 10 (for 100..Vmax)	for n type
		1 (for 0..-10V), 5 (for -10..-100V), 10 (for -100..Vmax)	for p type
Compliance [A]	=	10u	
Wait [ms]	=	1000	
Amplitude [V]	=	0.8	
Frequency [Hz]	=	1000	

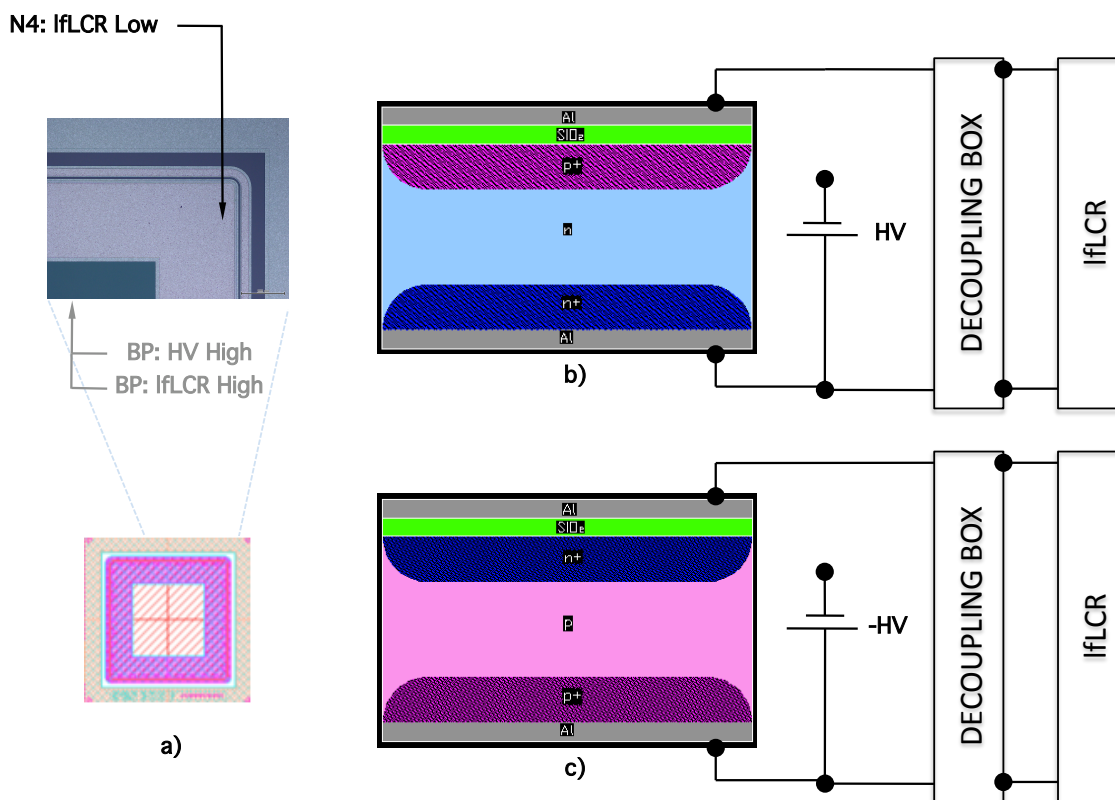**Table 3.3.:** CV diode measurement parameter

Figure 3.10.: a) schematic circuit and lateral sketches of b) N and c) P diode

3.3.3. C-V at mos

The design of this test structure is similar to the design of the diode except of the missing strip implant. MOS is the abbreviation for Metal Oxide Semiconductor where the measured parameter leads to the charge concentration in the oxide.

Measurement parameter

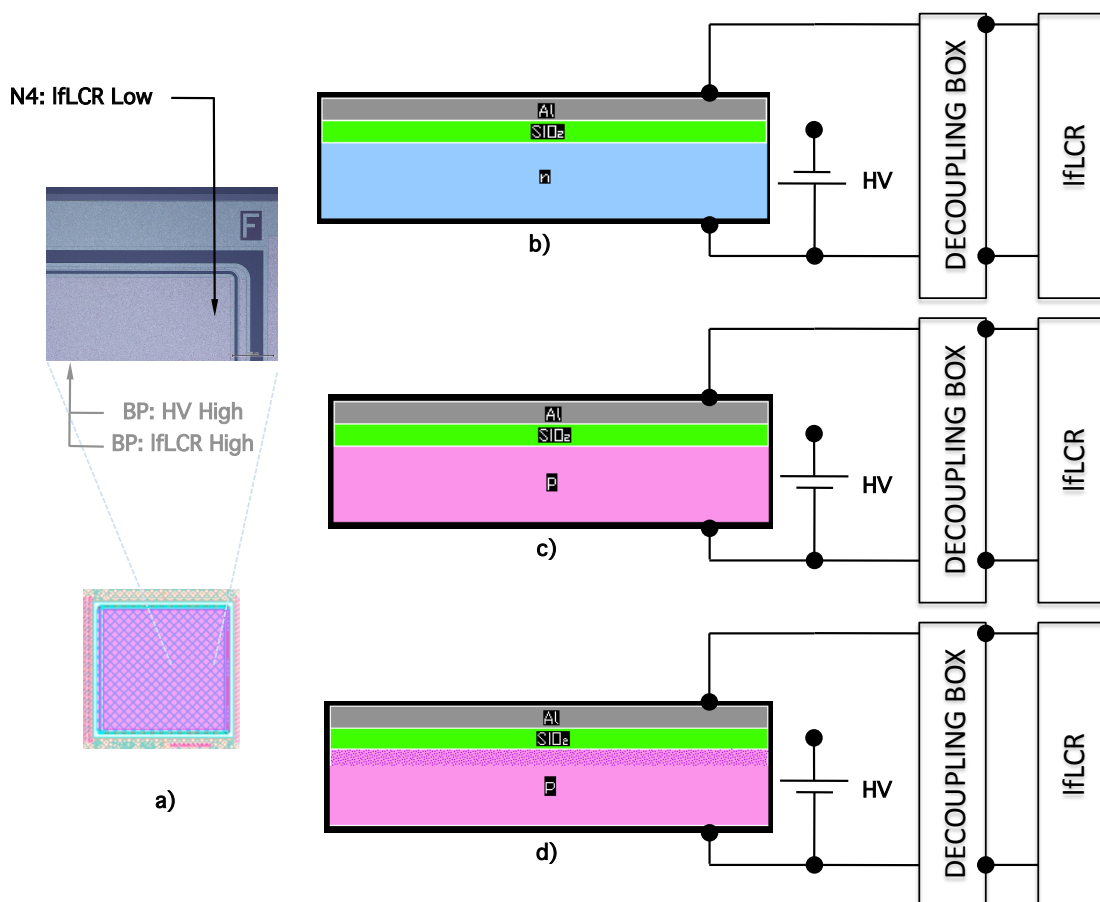|		
Voltage Max [V]	=	15
Start Voltage [V]	=	-10
Stepsize [V]	=	1
Compliance [A]	=	10u
Wait [ms]	=	1000
Amplitude [V]	=	0.8
Frequency [Hz]	=	1000

Table 3.4.: CV mos measurement parameter

Figure 3.11.: a) schematic circuit and schematic lateral sketches of b) N, c) P and d) Y MOS

3.3.4. I-V at gcd

The Gate Controlled Diode GCD consists of a comb-shaped strip implant intertwined with comb-shaped strips made of a MOS structure. The reverse bias is applied with the BIAS SMU and the current is measured with the GATE SMU to determine the interface recombination velocity.

Measurement parameter

BIAS HV (SMU 237)

Voltage Bias [V]	=	-5	for n type
		5	for p type
Compliance [A]	=	10u	

GATE V (SMU 2410)

Start Voltage [V]	=	-20
Voltage Max [V]	=	20
Stepsize [V]	=	1
Compliance [A]	=	10u
Wait [ms]	=	1000

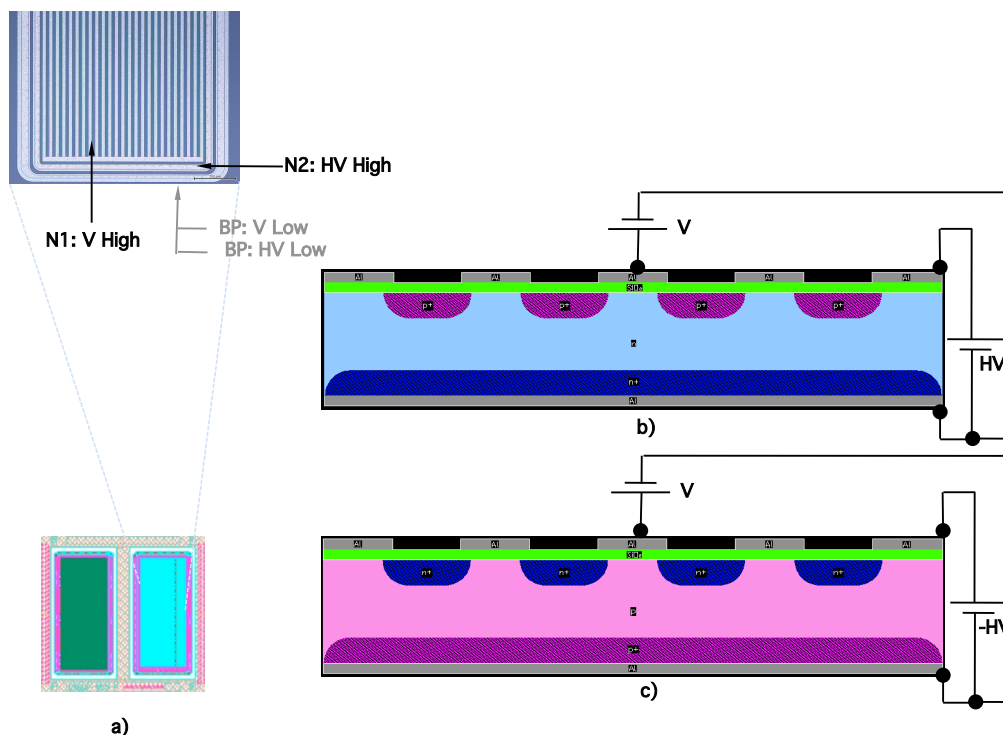**Table 3.5.:** IV gcd measurement parameter

Figure 3.12.: a) schematic circuit and schematic lateral sketches of b) N and c) P GCD

3.3.5. CINT-V at cap ac

The CAP AC test structure consists of the strips used for the detector. The bias ring is connected to the strips with a polysilicon resistor. The measurement of the interstrip capacitance is performed from the center strip to its two neighbors.

Measurement parameter

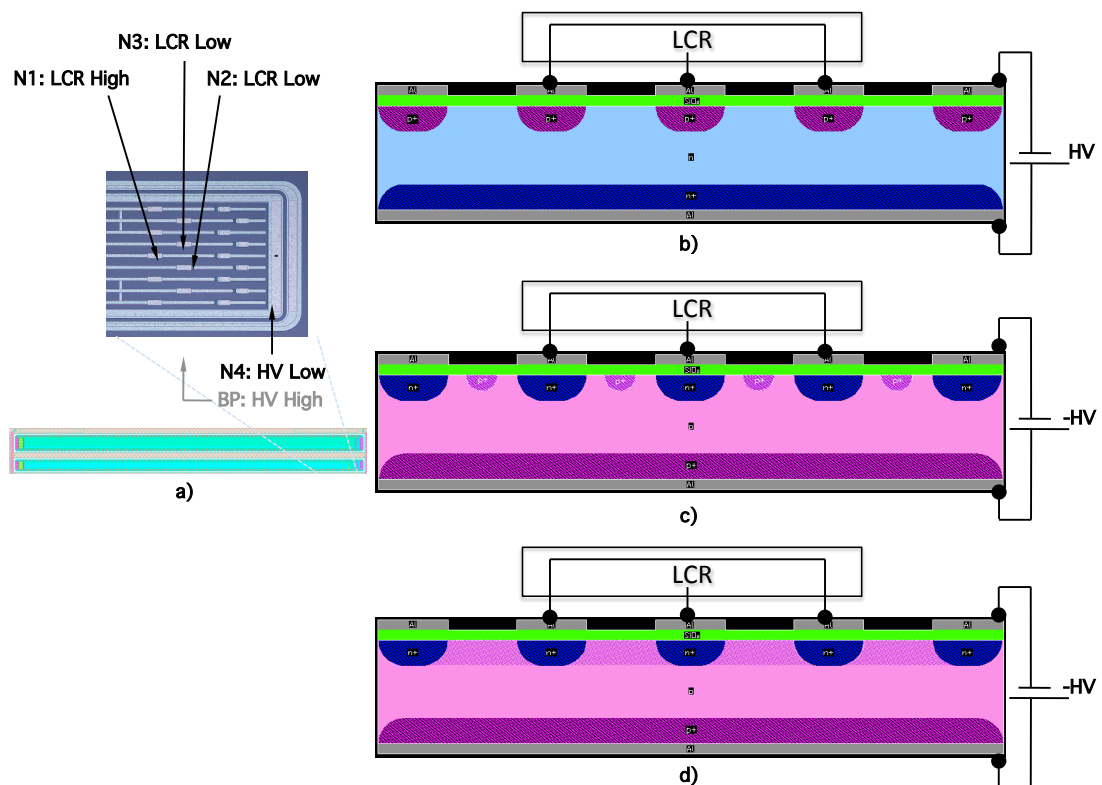|			
Start Voltage [V]	=	0	
End Voltage [V]	=	500	for n type
		-500	for p type
Stepsize [V]	=	1 (for 0..10V), 5 (for 10..100V), 10 (for 100..Vmax)	for n type
		1 (for 0..-10V), 5 (for -10..-100V), 10 (for -100..Vmax)	for p type
Compliance [A]	=	10u	
Wait [ms]	=	1000	
Amplitude [V]	=	0.8	
Frequency [MHz]	=	1	

Table 3.6.: CintV measurement parameter

Figure 3.13.: a) schematic circuit and schematic lateral sketches of b) N, c) P and d) Y CAP AC

3.3.6. RINT-V at cap dc

This test structure is similar to the CAP AC but the strip connection is different. As a polysilicon resistance would distort the interstrip resistance measurement, the strips at CAP DC are isolated from the bias ring.

Measurement parameter

BIAS V (SMU 2410)

Start Voltage Bias [V]	=	0	
Voltage Max [V]	=	180	for n type
		-180	for p type
Stepsize [V]	=	1 (for 0..10V), 5 (for 10..100V), 10 (for 100..Vmax)	for n type
		1 (for 0..-10V), 5 (for -10..-100V), 10 (for -100..Vmax)	for p type
Compliance [A]	=	100u	
Wait [ms]	=	1000	

GATE HV (SMU 237)

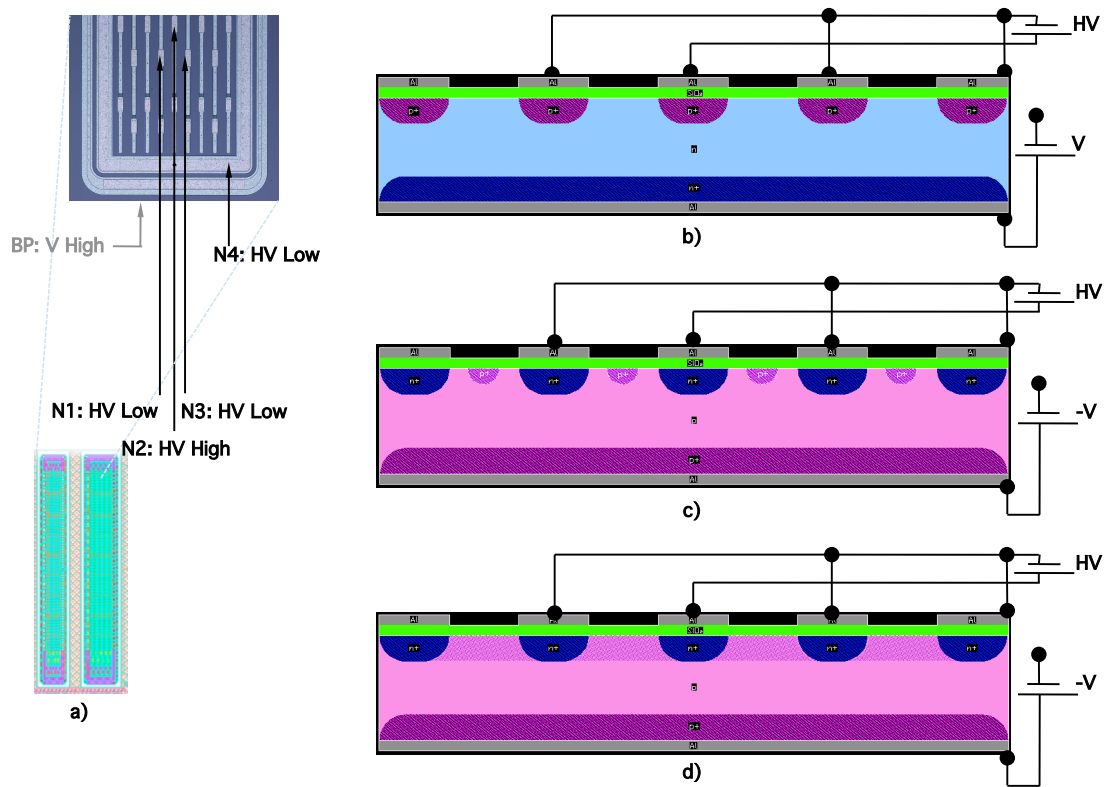|		
Voltage Max [V]	=	2
Voltage Min [V]	=	-2
Stepsize [V]	=	0.5
Compliance [A]	=	10u

Table 3.7.: RintV measurement parameter

Figure 3.14.: a) schematic circuit and schematic lateral sketches of b) N, c) P and d) Y CAP DC

3.3.7. CAC at cap

The dielectric of the strips consists of an oxide layer. The measurement of the coupling capacitance CAC leads to the oxide thickness. At the CAP test structure the strips are isolated from the bias ring.

Measurement parameter

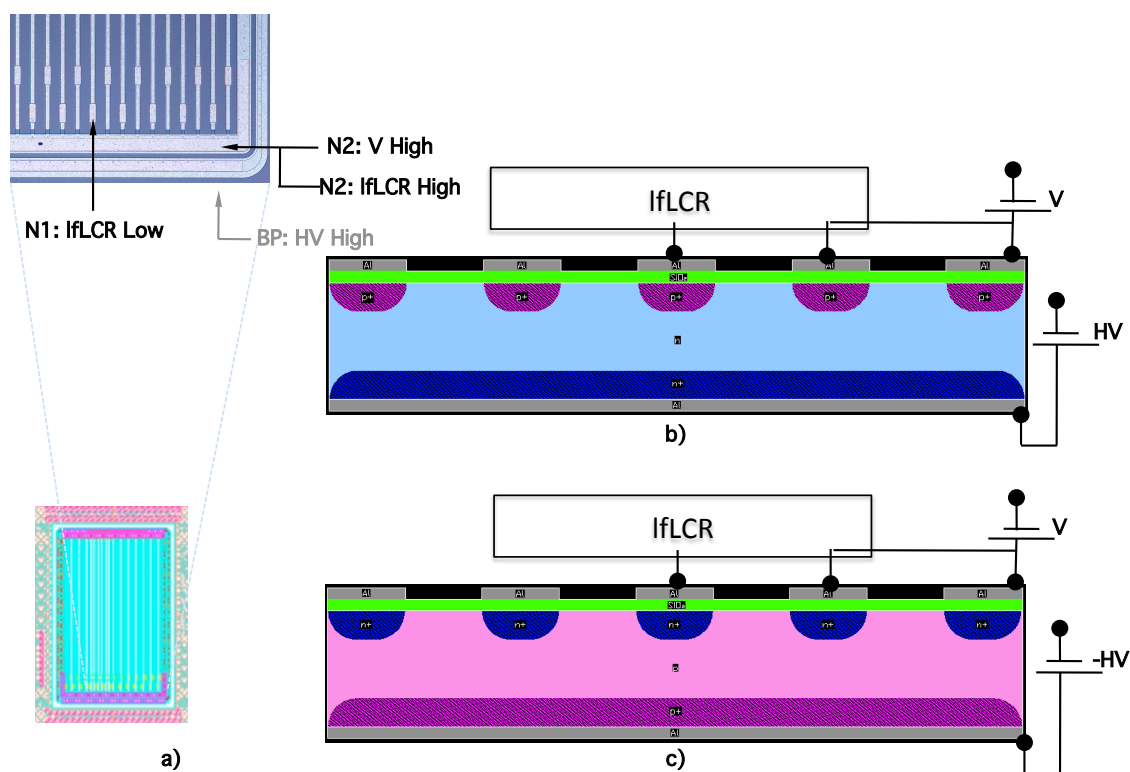|			
Bias Voltage [V]	=	70	for n type
		-70	for p type
Compliance [A]	=	10u	
Amplitude [V]	=	0.8	
Frequency [Hz]	=	1000	

Table 3.8.: CAC measurement parameter

Figure 3.15.: a) schematic circuit and schematic lateral sketches of b) N and c) P CAP

3.3.8. I-V at cap

At the same test structure of the coupling capacitance measurement also the dielectric breakdown voltage of the oxide is determined. The bias voltage is applied with the GATE SMU and the break down voltage is determined due to the current measurement of the BIAS SMU.

Measurement parameter

BIAS V (SMU 2410)

Start Voltage [V]	=	0
Compliance [A]	=	10u

GATE HV (SMU 237)

Voltage Max [V]	=	400	for n type
		-400	for p type
Stepsize [V]	=	10	
Compliance [A]	=	1u	
Wait [ms]	=	1000	

Table 3.9.: breakdown voltage measurement parameter
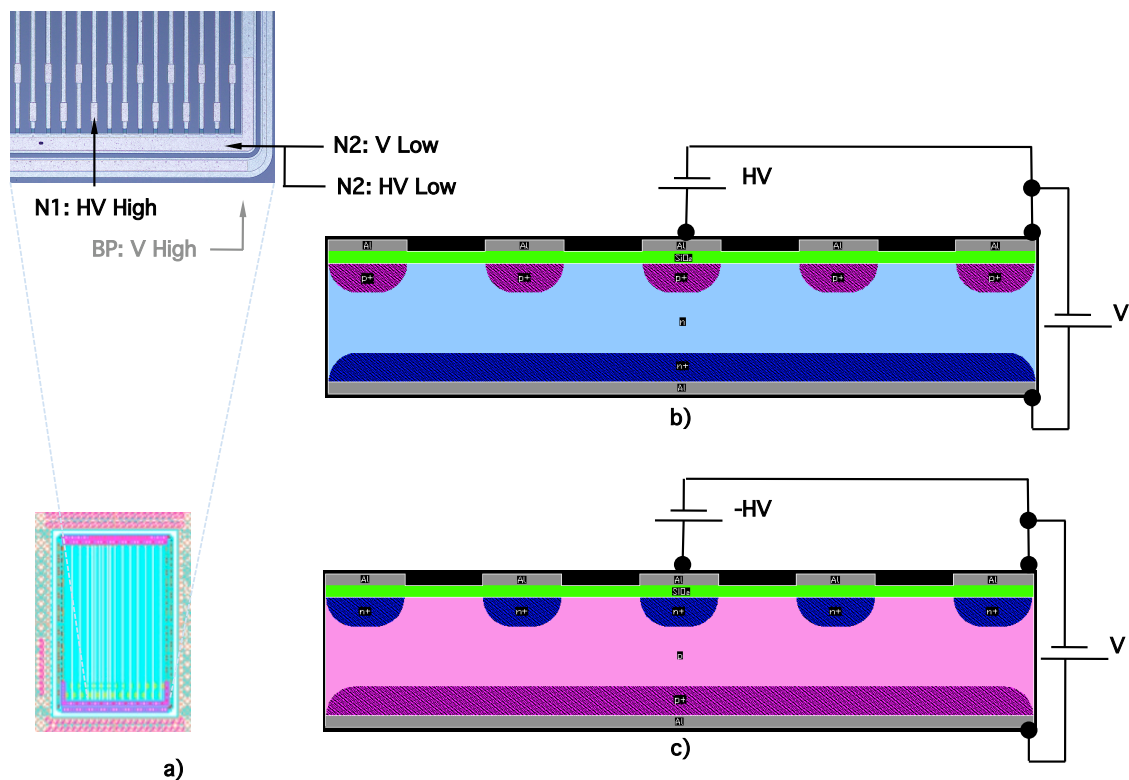

Figure 3.16.: a) schematic circuit and schematic lateral sketches of b) N and c) P CAP

3.3.9. Resistance at sheet

Different resistance values of implants, aluminum and polysilicon material are measured. These are the same materials which are used for the detector. There are two different widths for each resistance measurement to get a sufficient statistic for calculating the resistivity value.

Measurement parameter

Bias Voltage [V]	=	70	for n type
		-110	for p type
Compliance [A]	=	10u	

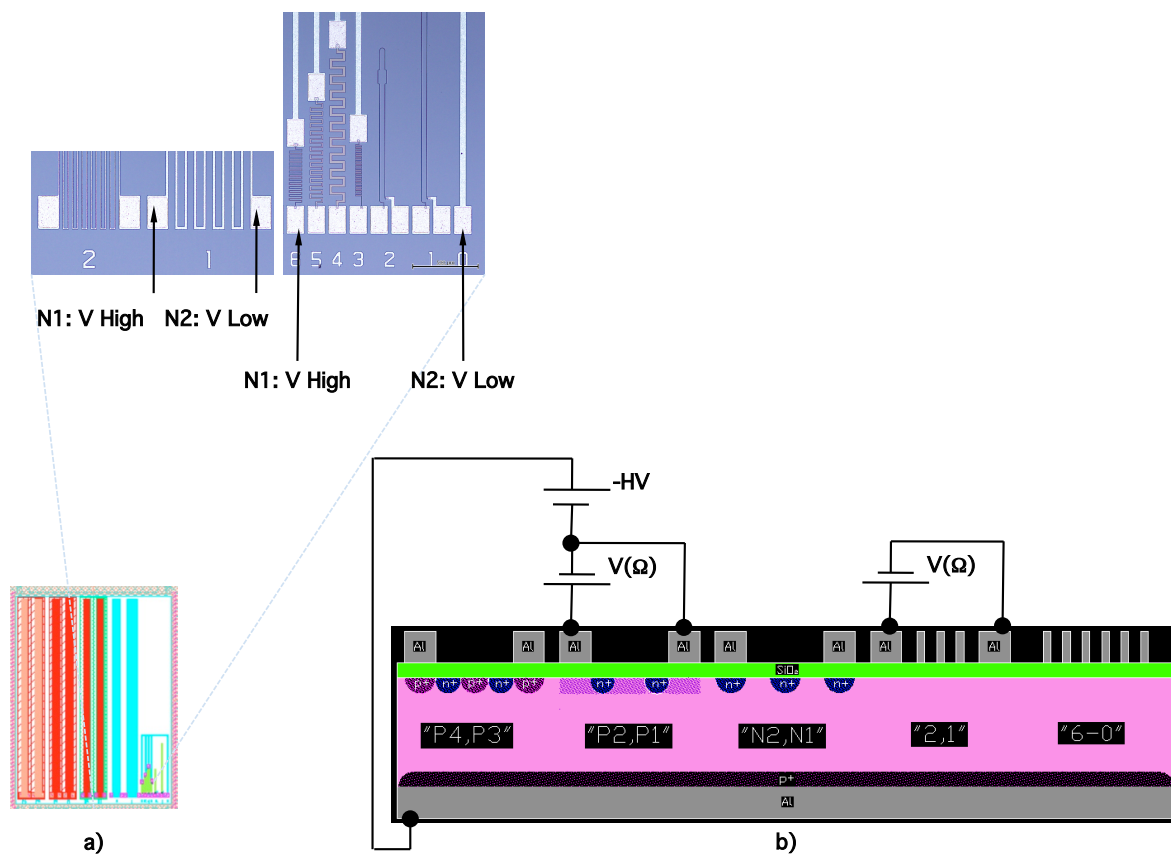**Table 3.10.:** SHEET measurement parameter

Figure 3.17.: a) schematic circuit and schematic lateral sketches of b) Y SHEET

The labeling of the different materials depends on the bulk type, the polysilicon and aluminum have the same digits (2,1 for aluminum and 6-1 for polysilicon).

The polysilicon material has four different widths and additionally two different shapes.

The sub implants, which is the implant that encloses each TS, are called P4,P3 for p types and N2,N1 for the n types.

The p stop and p spray implants are called P2,P1 for p types. On n types there is no comparable material to p stop or p spray. Those so called 2,1 structures have no measurement relevance.

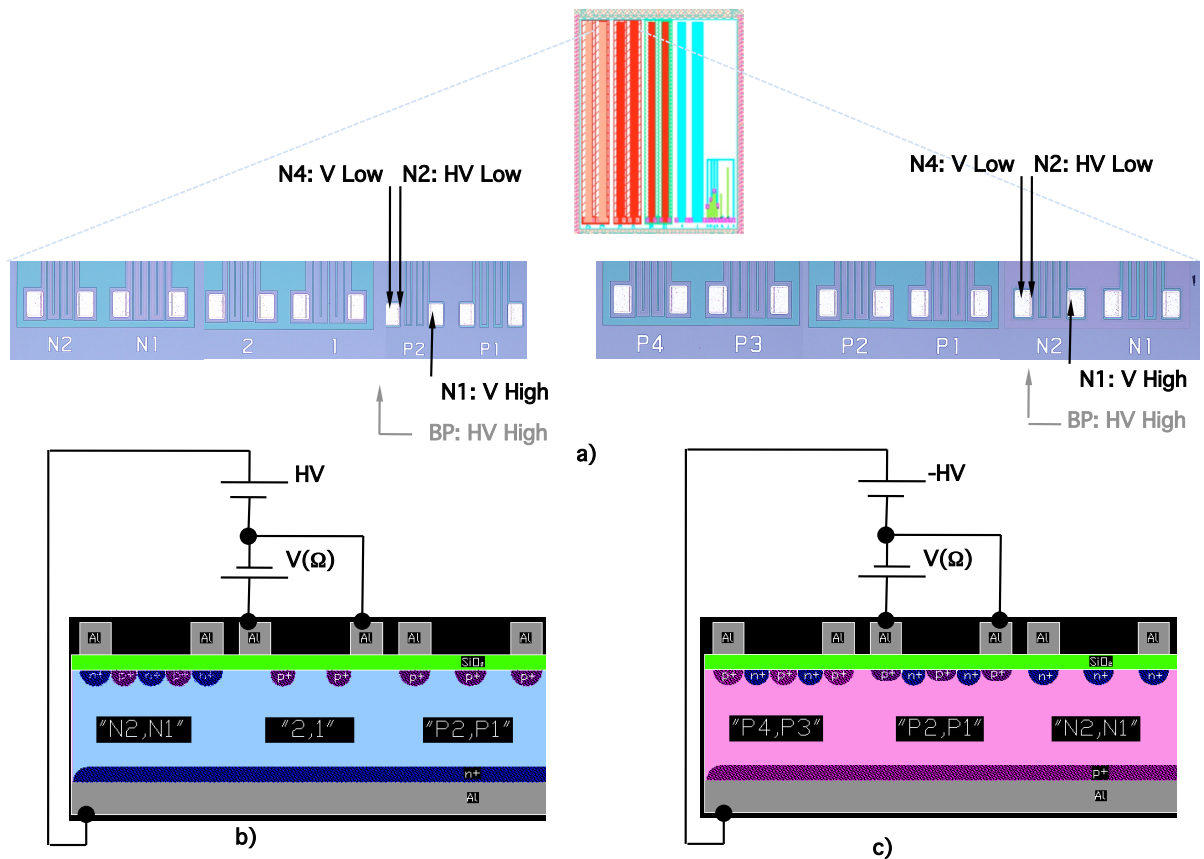The strip implants are called N2,N1 for p type and P2,P1 for n type.

Figure 3.18.: a) schematic circuit and schematic lateral sketches of b) N and c) P SHEET

3.3.10. Resistance at via

The term VIA describes the aluminum connection from the implant layer to the metal pad. The measurement is the same as used for the sheet test structure.

Measurement parameter

Bias Voltage [V]	=	70	for n type
		-110	for p type
Compliance [A]	=	10u	

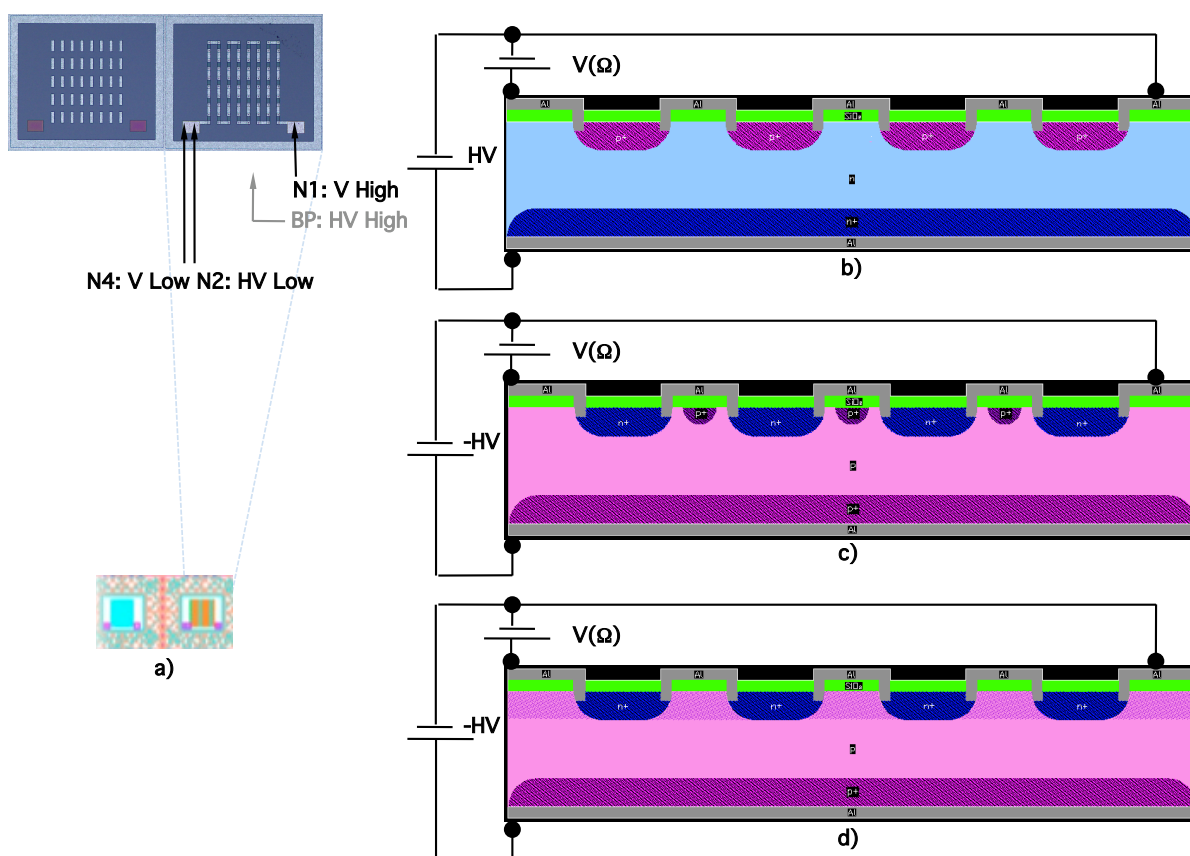**Table 3.11.:** VIA measurement parameter

Figure 3.19.: a) schematic circuit and schematic lateral sketches of b) N, c) P and d) Y VIA1

4. Results of Unirradiated Test Structures

The used measurement circuits and parameters can be found in chapter 3.3. In this chapter, the absolute values of unirradiated Halfmoons are presented.

4.1. Diode

4.1.1. Dark Current (TS diode)

The dark current increases exponentially with the bias voltage V, as given in equation 4.1. The exponential term can be neglected if a negative high voltage is applied. Then I_0 determines the current which correspond to the constant dark current in a detector.

$$I = I_0 \cdot [exp(\frac{eV}{kT}) - 1] \tag{4.1}$$

Diodes break down at a certain voltage, the better the manufacturing process the higher the Break Down Voltage. The maximum voltage used in the measurements is 700V and therefore it is always greater than 700V except for the thin Epi50. The mean value for the thin Epi material is 567 ± 74V. Therefore the maximum used voltage for Epi50 is 550V.
The current decreases with lower temperature as less charge carriers are in the conduction band. This effect can be seen in the results of MCZ P diodes in figure 4.1 where also the wafer dependency is investigated. The results of four different diodes are seen where two of them are from the same wafer. The diodes with the same TS number but different wafer number are indicated with dots. The dark current with the same TS numbers are more identical compared to the current with the same wafer number which indicates an inhomogeneous process on single wafers.

It is expected that the current increases before being saturated because with increasing the reverse voltage, the depletion zone grows until the whole detector is depleted. This is seen on MCZ and Epi materials but not for FZ. The reason for this unexpected IV behavior are defects which has been introduced during the deep diffusion process. The common method for producing thin detectors is wafer bonding where a carrier wafer with low resistivity is bonded with the sensor material. The cheaper method is deep diffusion where the active volume of the detector is less doped compared to the inactive volume. The difference of the effective doping concentration is seen in figure 4.2 where the transition of the effective doping concentration of the common process is sharp compared to deep diffusion.
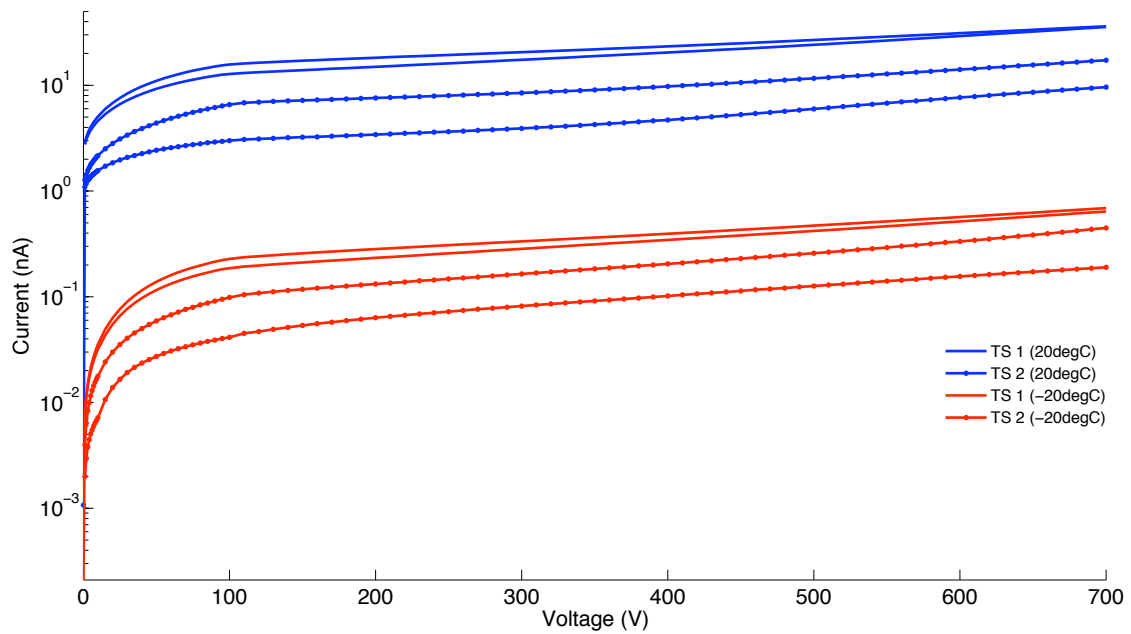
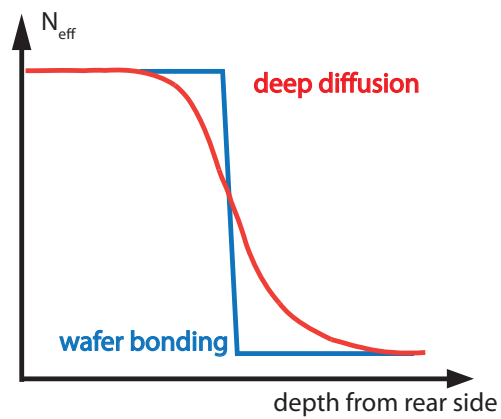**Figure 4.1.:** IV of MCZ P diode, temperature and wafer dependency, T=± 20°C

Figure 4.2.: difference between deep diffusion and wafer bonding [6]

A thicker TS should introduce a higher current due to more charge carriers which is in agreement with Epi and MCZ, whereas the FZ current is higher for thin TS compared to thicker ones. The thickness dependency of FZ P diodes is seen in figure 4.3. A deep hole trap defect was found as possible current generator [6]. The non saturated IV behavior is dominantly seen in the results of the thinnest FZ in figure 4.3, as the thinner the TS the higher defect concentration is.
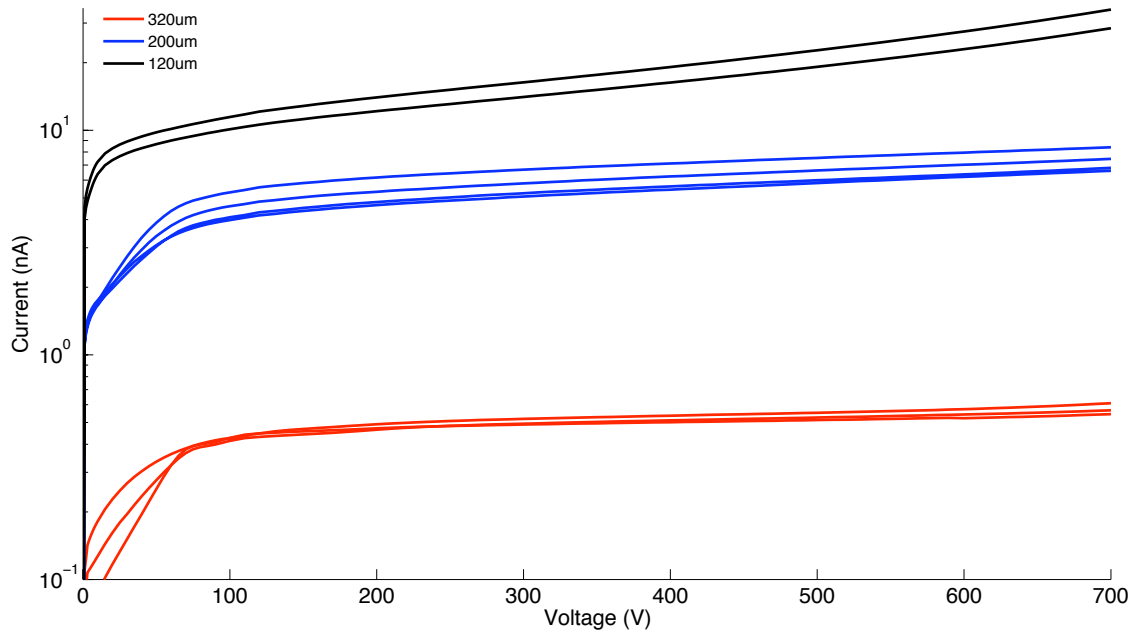

Figure 4.3.: IV of FZ P diode, thickness dependency, T= 20°C

The expected saturation behavior is seen in the results of the 100 um thick Epi diodes in figure 4.4 where also the type difference is investigated. The current of n type diodes are higher compared to p type due to the higher mobility of electrons which is valid for Epi and MCZ material.

The higher resistivity of MCZ compared to FZ or Epi should lead to a lower current when applying the same voltage. The results for Y TS are seen in figure 4.5 but due to thickness dependency only MCZ200 with FZ200 and Epi100 with FZ120 are comparable.
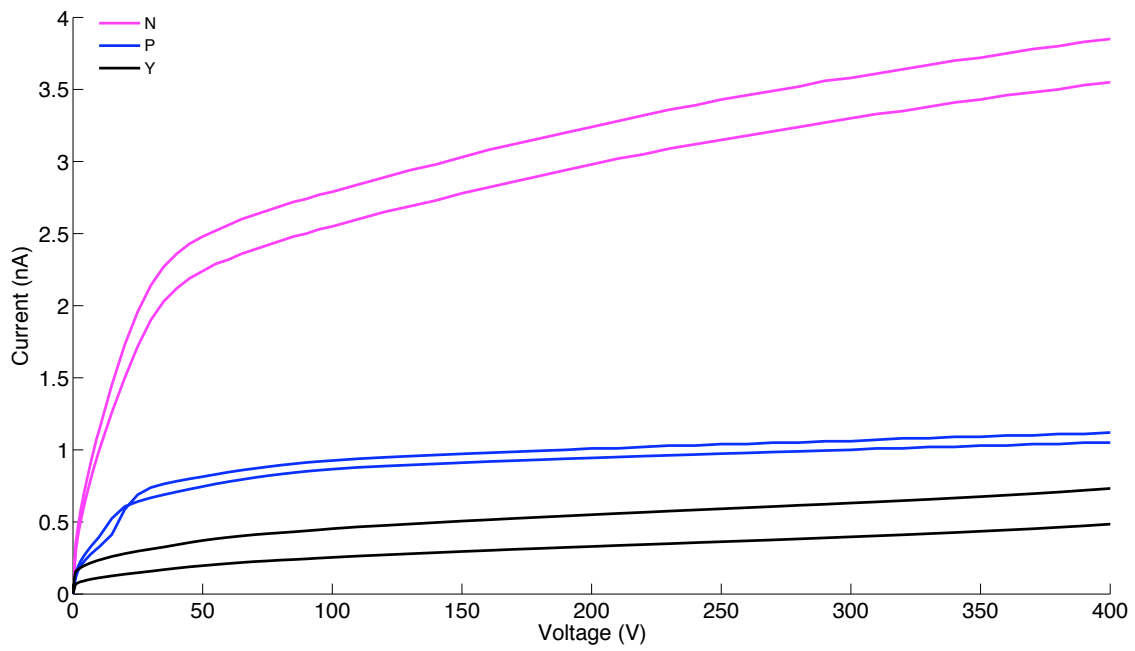
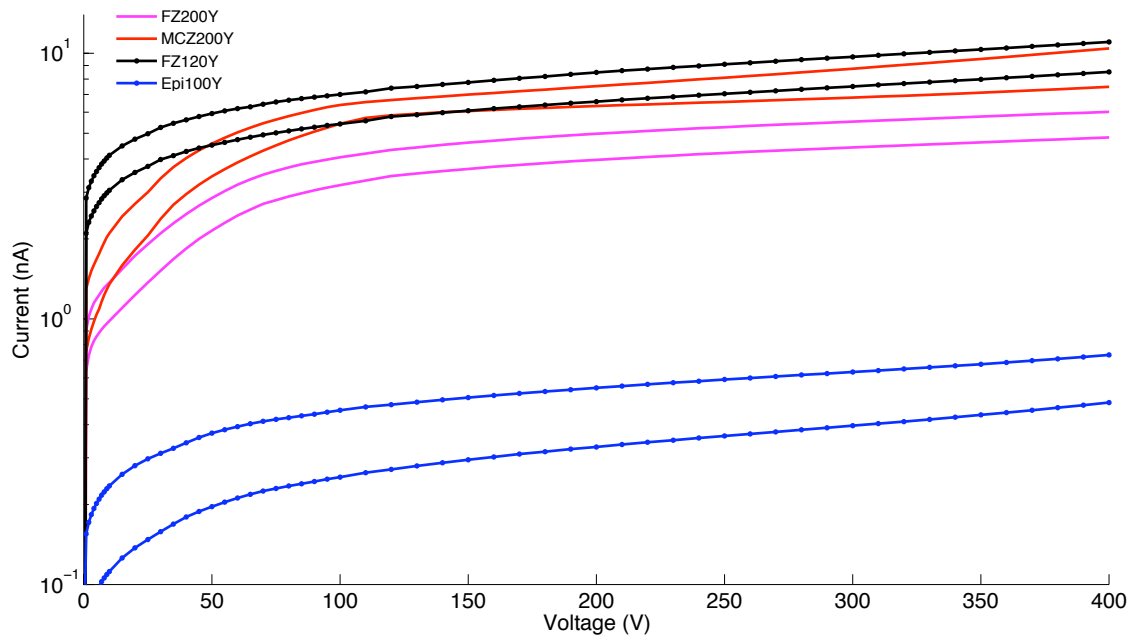**Figure 4.4.:** IV of Epi100 diode, type dependency, T= 20°C

Figure 4.5.: IV of Y diode, material dependency, T= 20°C

4.1.2. Full Depletion Voltage (TS diode)

The capacitance is inverse proportional to the reverse bias voltage V until the bulk is fully depleted of charge carriers. As given in equation 4.2, the capacitance also depends on the mobility μ of the major charge carriers and the resistivity ρ.

$$C = \sqrt{\frac{\varepsilon_0 \cdot \varepsilon_r}{2 \cdot \mu \cdot \rho \cdot V}} \cdot A_{cv} \tag{4.2}$$

The determination for the full depletion voltage is done by plotting $1/C^2$ against the reverse bias voltage. Two linear regions can be distinguished. The first one correspond to the increase of $1/C^2$ as the depletion zone is built up and the second one describes the saturated capacitance. At the intersection, the value for full depletion is extracted.
With the bulk resistivity values given from HPK, the expected depletion voltage can be calculated using equation 4.3.

$$\rho_{bulk} = \frac{d^2}{2 \cdot \varepsilon_0 \cdot \varepsilon_{Si} \cdot \mu \cdot V_{depl}} \tag{4.3}$$

The results for each type and material are listed in table 4.1. The measurement results for thin TS have to be fixed by hand as the depletion voltage extracted from the used fitting method disagree with the expected depletion voltage values. The results are confirmed from other labs. The parameter bulk concentration N_{bulk} and depletion thickness d_{depl} can be calculated with equation 4.4 and the results are listed in table 4.2.

$$N_{bulk} = \frac{2 \cdot \varepsilon_0 \cdot \varepsilon_{Si} \cdot \mu \cdot V_{depl}}{e \cdot d^2}, d_{depl} = \frac{\varepsilon_0 \cdot \varepsilon_r \cdot A_{cv}}{C_{depl}} \tag{4.4}$$

As given in equation 4.4, the depletion capacitance depends on the thickness. The dependency of 320 um and 200 um thick FZ diodes are plotted in figure 4.6 where also the different wave shapes depending on the type are seen.

The wave shapes of Y diodes are smoother compared to P diodes, which is unexpected as the comparable N diodes do not show this strange behavior. This results is seen in the comparison plot of MCZ P and Y diodes in figure 4.7. This is valid for all materials except for the Epi which is seen in figure 4.8 with the results of P diodes. The expected doping concentration of Epi diodes has a sharp transition between the carrier wafer and active volume and this leads to a definite intersection for analysis, as the first linear region has a more rampant slope in the $1/C^2$ plot. The results are independent of temperature which is also seen in figure 4.8.

There are no significant differences in terms of wafer or TS number.

	HPK	expected	measured
	ρ_{bulk}	V_{depl}	V_{depl}
	$[k\Omega cm]$	[V]	[V]
FZP 320um	3 - 8	136 - 363	223.2 ± 7.2
FZP 200um	3 - 8	53 - 142	105.8 ± 5.3
FZP 120um	3 - 8	19 - 51	72.9 ± 34.8
FZN 320um	1.2 - 2.4	146 - 292	186.6 ± 0.5
FZN 200um	1.2 - 2.4	57 - 114	98.4 ± 10.8
FZN 120um	1.2 - 2.4	21 - 41	70.1 ± 28.2
MCZP 200um	> 2	< 213	132.3 ± 39.3
MCZN 200um	> 0.5	< 273	148.5 ± 5.5
EpiP 50um	0.5 - 2	13 - 53	22.4 ± 3.6
EpiP 100um	0.5 - 2	53 - 213	74.9 ± 8.8
EpiN 50um	0.5 - 2	4 - 17	4.4 ± 0.4
EpiN 100um	0.5 - 2	17 - 68	28.5 ± 1.7

Table 4.1.: bulk resistivity and depletion voltage, T= 20°C

	calculated	calculated	calculated
	ρ_{bulk}	N_{bulk}	d_{depl}
	$[k\Omega cm]$	$[cm^{-3}]$	[um]
FZP 320um	4.9	3.3E17	231.2
FZP 200um	4.0	4.5E17	178.7
FZP 120um	2.1	8.9E17	98.5
FZN 320um	1.9	1.3E17	240.9
FZN 200um	1.4	1.6E17	173.4
FZN 120um	0.7	3.0E17	114.9
MCZP 200um	3.2	1.9E17	172.1
MCZN 200um	0.9	6.8E17	170.1
EpiP 50um	1.2	5.3E17	44.7
EpiP 100um	1.4	4.4E17	78.3
EpiN 50um	1.9	3.2E17	44.5
EpiN 100um	1.2	5.2E17	80.7

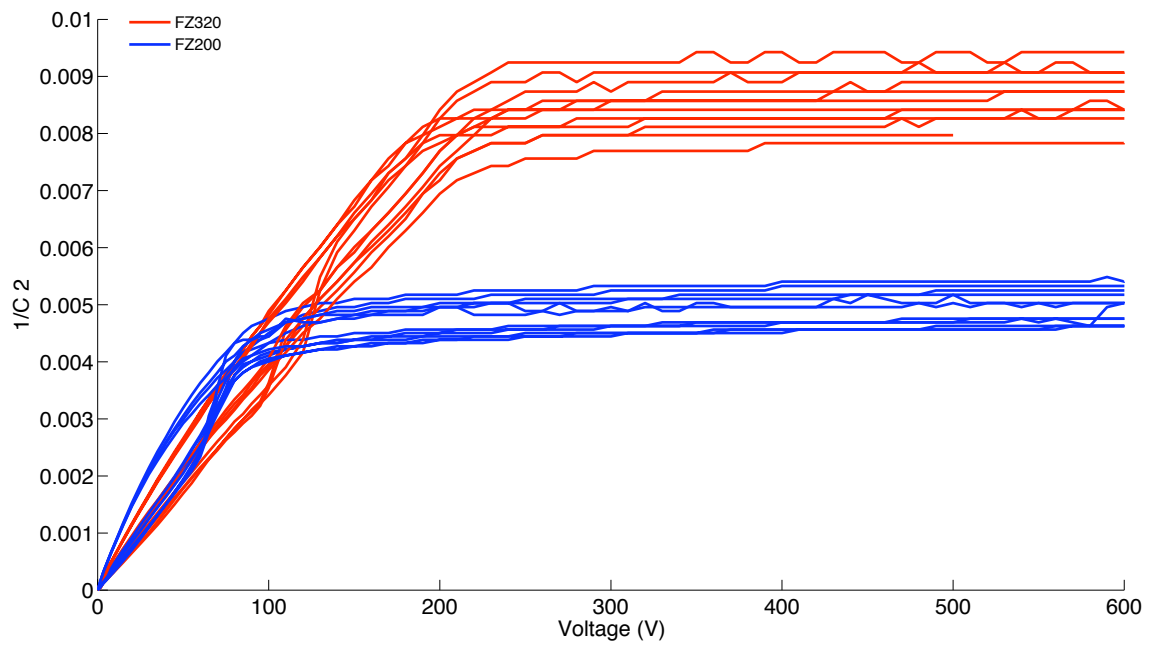**Table 4.2.:** bulk concentration and depletion thickness, T= 20°C

Figure 4.6.: CV of FZ diode, thickness dependency, T=± 20°C
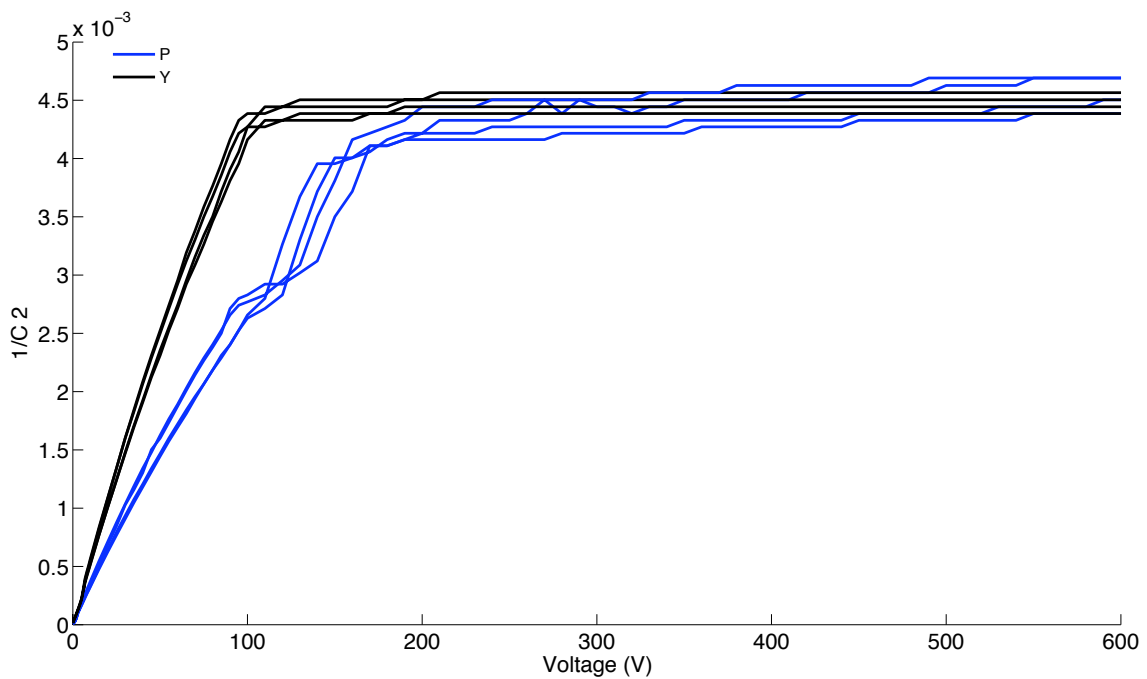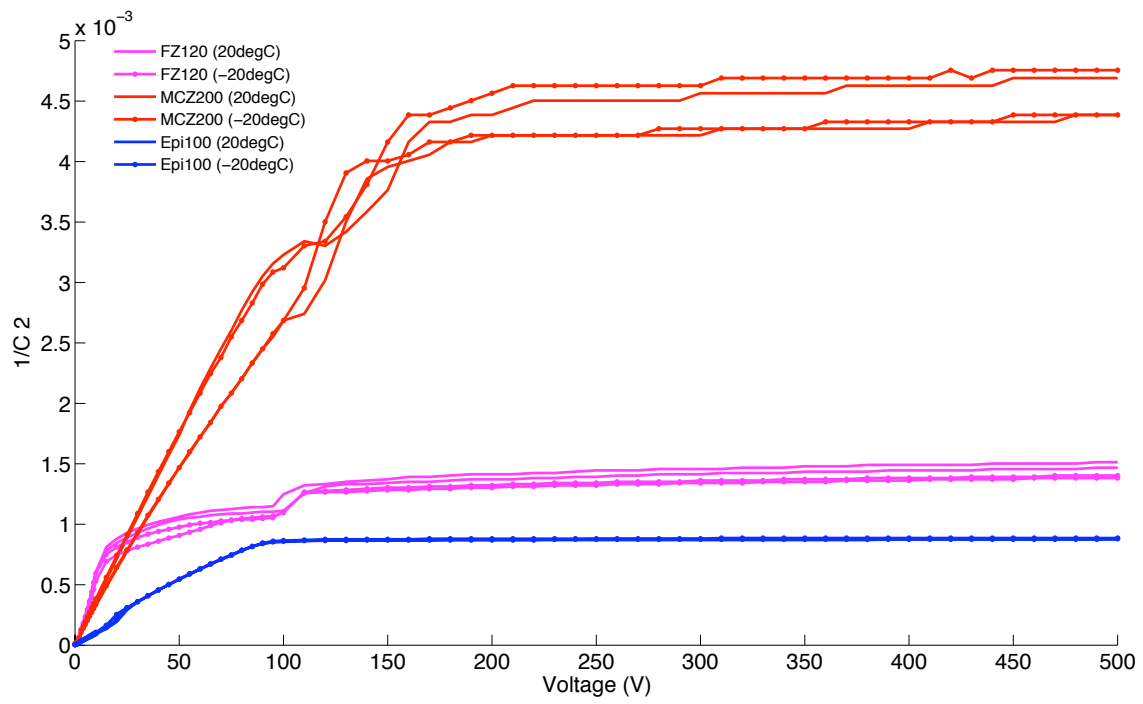

Figure 4.7.: CV of MCZ diode, type dependency, T=20°C

Figure 4.8.: CV of P diode, material and temperature dependency, T=± 20°C

4.2. Surface Current

4.2.1. Interface Recombination Velocity (TS gcd)

The measured current is a superposition of a constant bulk current and a surface current which varies with the applied voltage. For the MOS structure, different conditions are defined which are described in detail in chapter 4.6. In the accumulation condition the electrons, that are attracted by oxide charges, prevent depletion and only the bulk current is measured. In the depletion condition the region of the diode connects with the depletion region of the MOS material underneath the metal, as free electrons are repelled by the negative applied voltage. A sharp increase in the current is measured which correspond to the surface current. A higher negative voltage repels the electrons further into the bulk where the electrons form an inversion layer. Therefore the depletion region breaks down at the inversion condition and the measured current corresponds to a bulk current again.

The current decreases with temperature as already explained in chapter 4.1.1. The current change is also smaller at -20°C which leads to difficulties. The measured current is a few pA and the change is only about a few fA. Therefore measurements are performed at -15°C to have comparable results with irradiated TS. The calculation of the recombination velocity is done for 20°C as the current changes are still a few pA and this leads to high uncertainty.

The absolute values of the interface recombination velocity v_0 are listed in table 4.3 which are calculated with equation 4.5 [3]. I_{surf} correspond to the measured surface current and the intrinsic carrier density n_i for silicon at room temperature is $n_i = 1.45\text{E}10\ cm^{-3}$ [3]. The mean value is about 20 cm/s without the results from p type MCZ material and EpiY.

$$v_0 = \frac{I_{surf}}{e \cdot A_{gcd} \cdot n_i} \tag{4.5}$$

The material dependency is seen in figure 4.9 for N TS where the bulk current is comparable independently of the material. The higher current change of MCZN correspond to a higher surface current.

Figure 4.10 shows the material dependency for P TS and the difference in thickness of the Epi material. The material dependency in the bulk current on the p type bulk might be due to the different thicknesses of each material. The thinner Epi material has a lower bulk current compared to the thicker one.

The thickness dependency on FZ is seen in figure 4.11 where the bulk current is higher for thin TS. This is the same defect effect of deep diffusion processing again.

The type dependency is seen in figure 4.12 for MCZ material where the Y TS have only one current change. This wave shape of Y is caused by the non-uniformed doped p type which is discussed in detail in chapter 4.6.2.

	Surface Current	Velocity
	[pA]	[cm/s]
FZP 320um	80.23 ± 5.71	18.01 ± 1.28
FZP 200um	87.60 ± 28.70	19.66 ± 6.44
FZP 120um	-	-
FZY 320um	93.10 ± 32.50	20.89± 7.29
FZY 200um	105.15 ± 34.20	23.60 ± 7.68
FZY 120um	-	-
FZN 320um	90.10 ± 2.89	20.22 ± 0.65
FZN 200um	78.05 ± 8.60	17.52 ± 1.93
FZN 120um	90.00 ± 14.14	20.20 ± 3.17
MCZP 200um	110.24 ± 26.00	24.74 ± 5.84
MCZY 200um	262.24 ± 46.66	58.85 ± 10.47
MCZN 200um	202.93 ± 13.14	45.54 ± 2.95
EpiP 50um	65.00 ± 7.07	14.59 ± 1.59
EpiY 50um	55.97 ± 8.40	12.56 ± 1.89
EpiN 50um	70.00 ± 0.00	15.71 ± 0.00
EpiP 100um	83.40 ± 7.40	18.72 ± 1.66
EpiY 100um	151.30 ± 29.60	33.96 ± 6.53
EpiN 100um	54.22 ± 5.70	12.17 ± 1.28

Table 4.3.: surface current and recombination velocity, T= 20°C
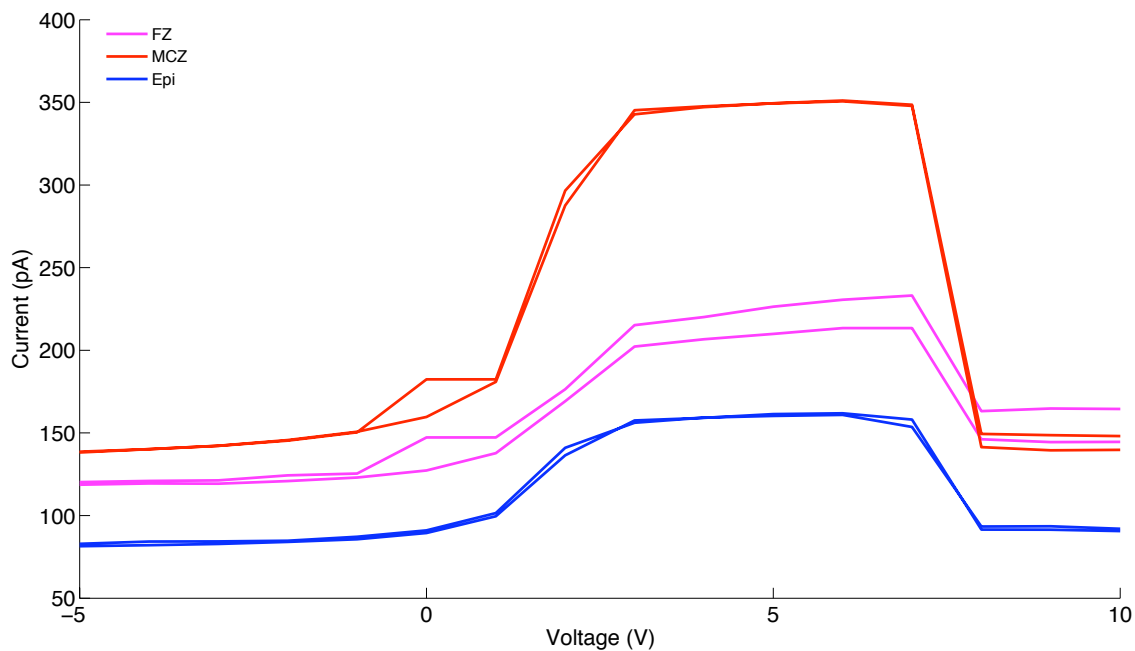

Figure 4.9.: IV of N FZ200, MCZ200, Epi50 gcd, material dependency on N, T= 20°C
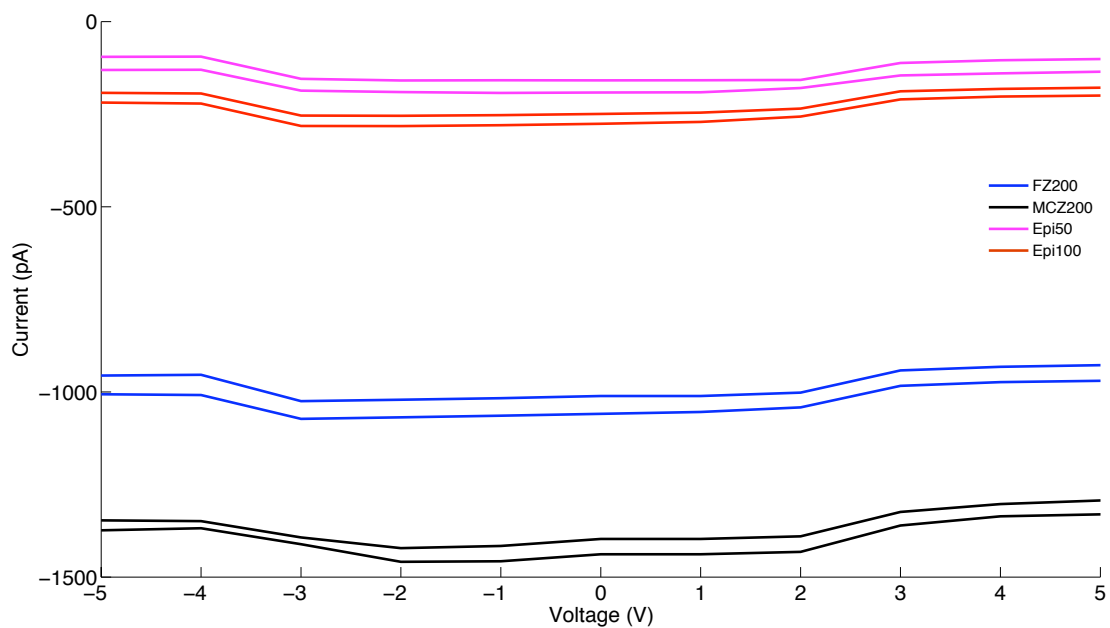
Figure 4.10.: IV of P FZ200, MCZ200, Epi gcd, material and thickness dependency on P, T= 20°C
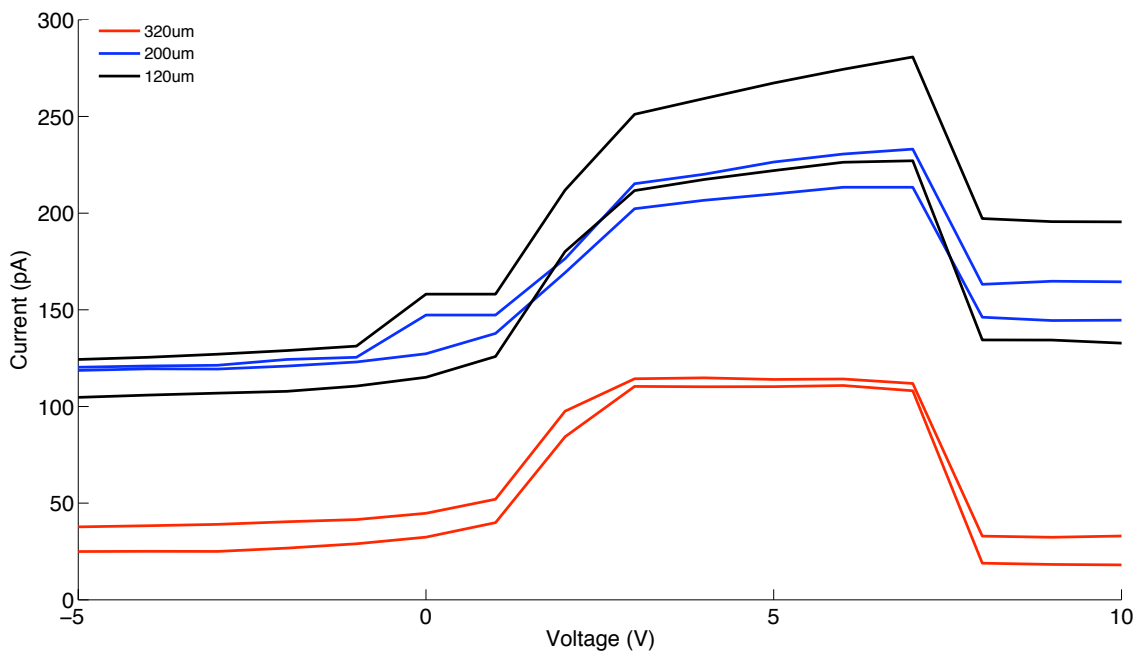

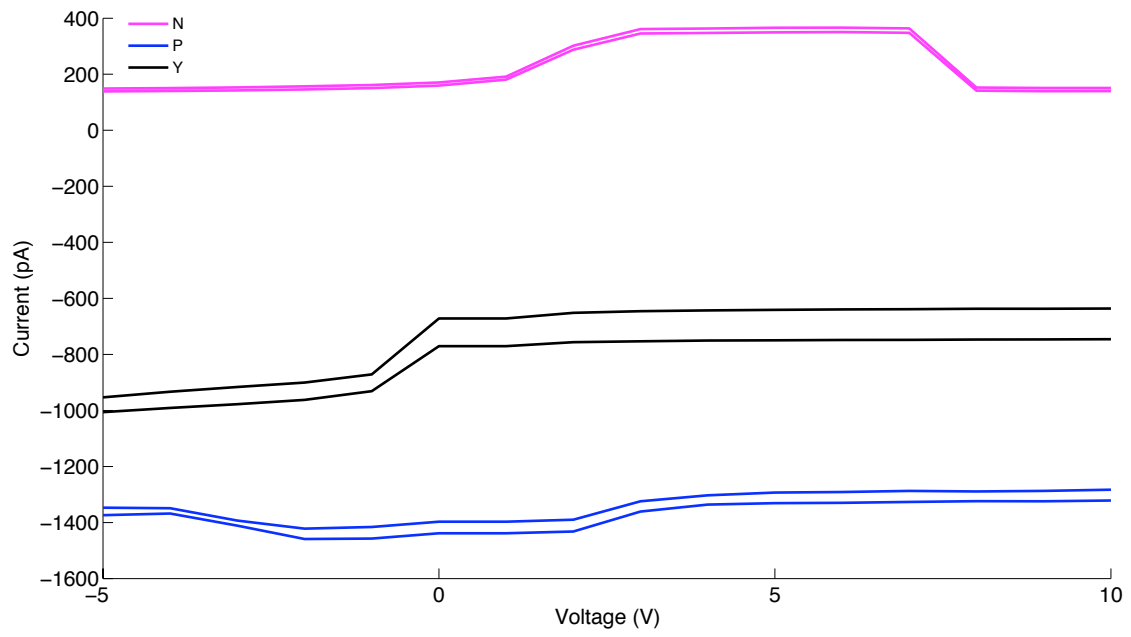**Figure 4.11.:** IV of FZN gcd, thickness dependency, T= 20°C

Figure 4.12.: IV of MCZ gcd, type dependency, T= 20°C

4.3. Strip Scans

4.3.1. Interstrip Capacitance (TS cap ac)

The absolute interstrip capacitance results are listed in table 4.4. There are two different pitches to the neighbor strips, it is either 80 um or 120 um. The absolute capacitance values differ slightly as the smaller 80 pitch lead to a higher capacitance when assuming the plate capacitance model but the wave shapes are identical for both pitches.

	80_{pitch}	120_{pitch}
	$[pF/cm]$	$[pF/cm]$
FZP 320um	0.72 ± 0.15	0.65 ± 0.13
FZP 200um	0.69 ± 0.15	0.61 ± 0.12
FZP 120um	0.54 ± 0.01	0.45 ± 0.01
FZY 320um	0.75 ± 0.15	0.66 ± 0.15
FZY 200um	0.77 ± 0.14	0.59 ± 0.11
FZY 120um	0.57 ± 0.03	0.47 ± 0.03
FZN 320um	0.63 ± 0.12	0.58 ± 0.08
FZN 200um	0.66 ± 0.09	0.55 ± 0.09
FZN 120um	0.51 ± 0.07	0.39 ± 0.03
MCZP 200um	0.71 ± 0.13	0.77 ± 0.09
MCZY 200um	0.64 ± 0.11	0.55 ± 0.11
MCZN 200um	0.61 ± 0.10	0.51 ± 0.08
EpiP 50um	0.23 ± 0.01	0.13 ± 0.00
EpiY 50um	0.28 ± 0.05	0.15 ± 0.03
EpiN 50um	0.30 ± 0.00	0.20 ± 0.01
EpiP 100um	0.41 ± 0.00	0.32 ± 0.01
EpiY 100um	0.41 ± 0.01	0.27 ± 0.01
EpiN 100um	0.47 ± 0.07	0.32 ± 0.01

Table 4.4.: interstrip capacitance results, T= 20°C

The CV characteristic leads to variable values within the first voltage steps as for example the n+ strips on the p bulk are not perfectly isolated from each other. The same can be said for the n bulk and p+ strips. The capacitance value is constant after the area beneath the implant is fully depleted. The FZ material shows a very slight thickness dependency whereas it is more dominant with the Epi material, which is seen in figure 4.13. This thickness dependency is expected as the backplane capacitance C_{bp} has to be taken into account which is indicated in figure 4.14. The value of C_{bp} changes with depletion.
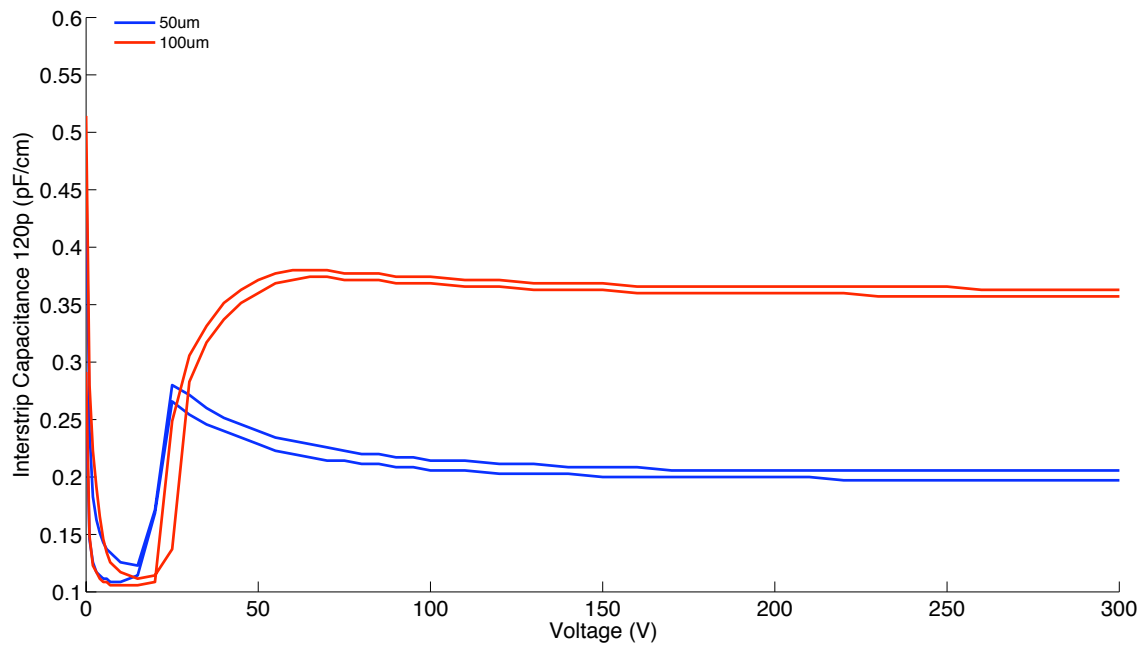
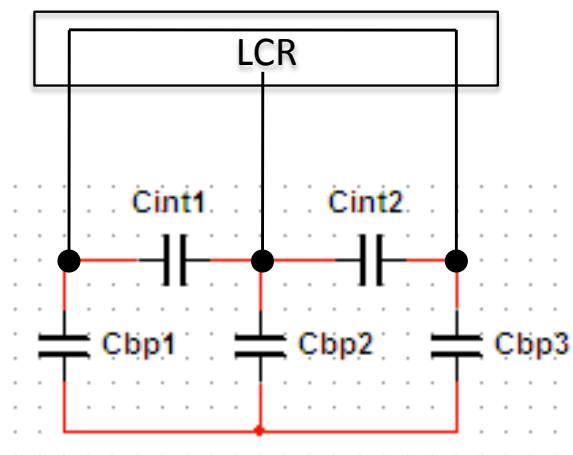**Figure 4.13.:** Cint-V of EpiN, thickness dependency, T= 20°C

Figure 4.14.: equivalent circuit diagram of interstrip capacitance measurement

The material dependency is seen in figure 4.15 for Y TS. The saturated capacitance values of FZ or MCZ are higher by factor of 2 compared to the Epi material but this could also be due to the different thicknesses. The material difference for P TS is seen figure 4.16 where also the temperature independence is seen. The differences in the end capacitance values are caused by inhomogeneous processing. The majority of the result showed higher values for N and P with TS number 2 compared to TS number 1 which is the opposite for Y. This effect is nicely shown in figure 4.17 for FZ.
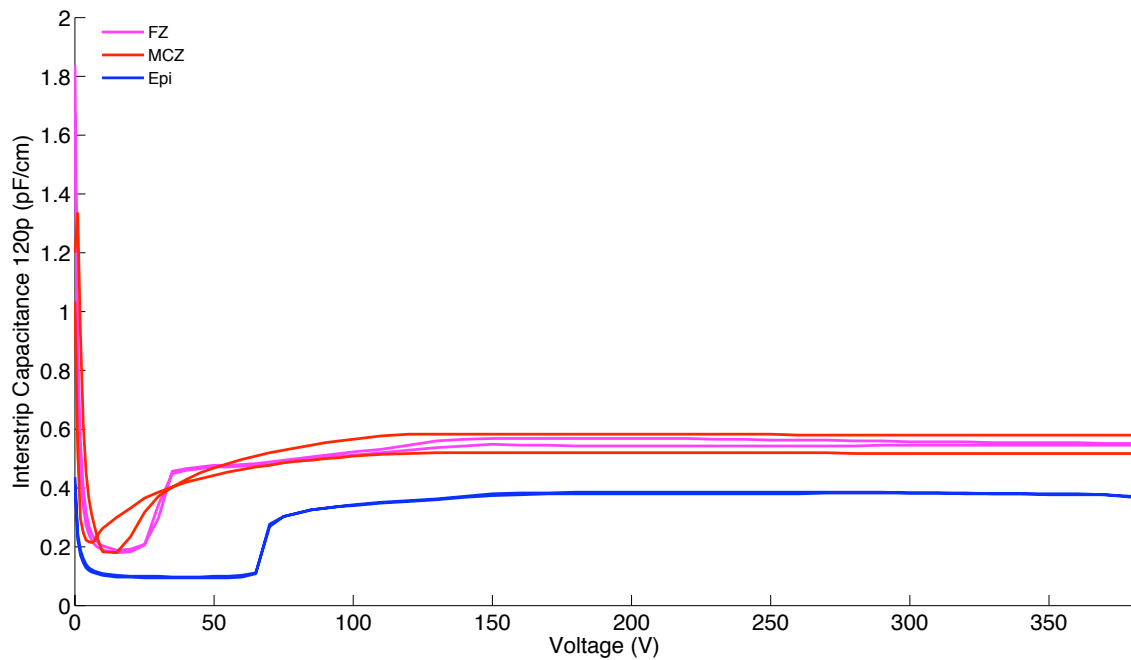

Figure 4.15.: Cint-V of Y FZ200, MCZ, Epi100 TS, material dependency, T= 20°C

The type dependency for Epi and FZ is seen in figure 4.18 and 4.19 where the wave shape also depends on material. The capacitance of the Epi100 material saturates at about 100V for p type and at 50V for n type whereas the saturation on FZ320 material is already at about 10V and does not depend on the bulk type.
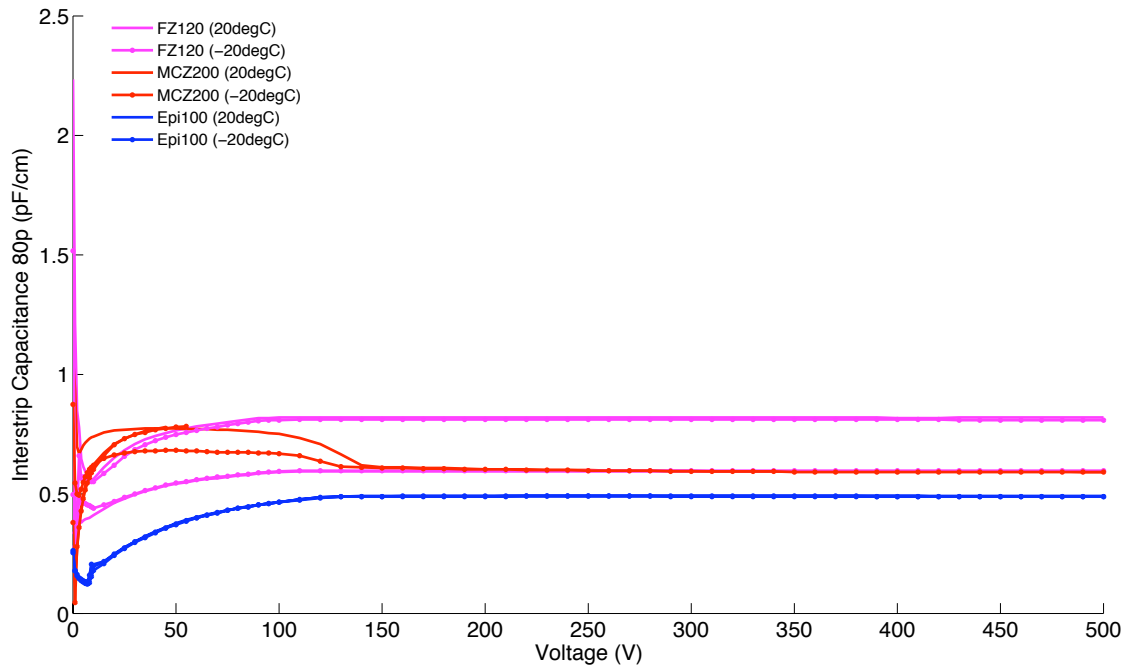
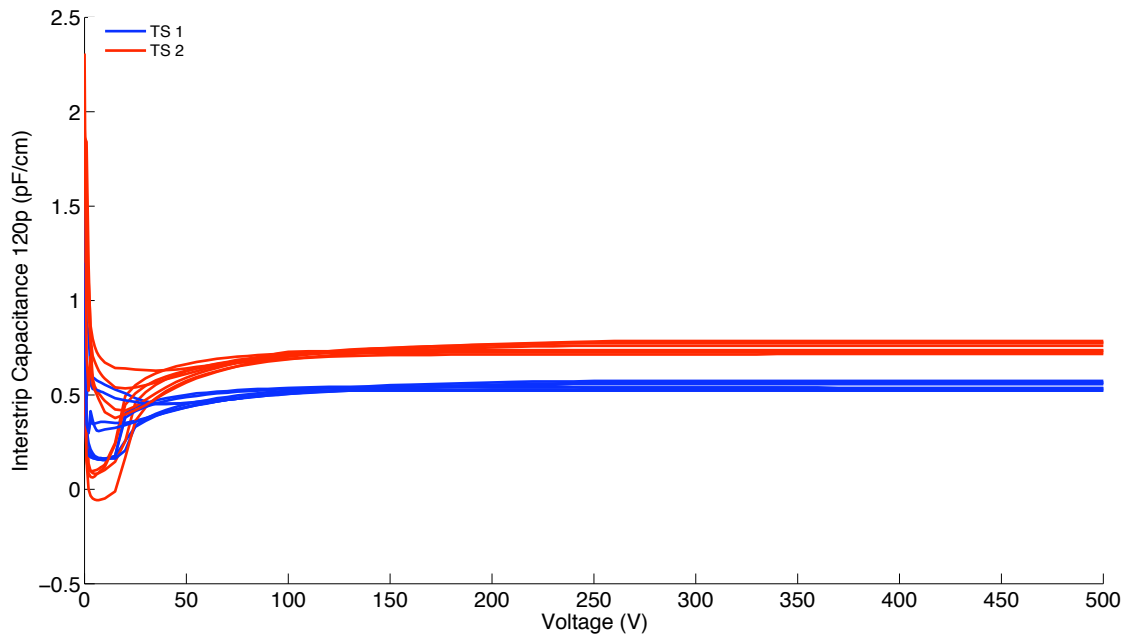**Figure 4.16.:** Cint-V of P TS, material and temperature dependency, T=± 20°C

Figure 4.17.: Cint-V of N and P FZ320, FZ200, wafer dependency, T=± 20°C
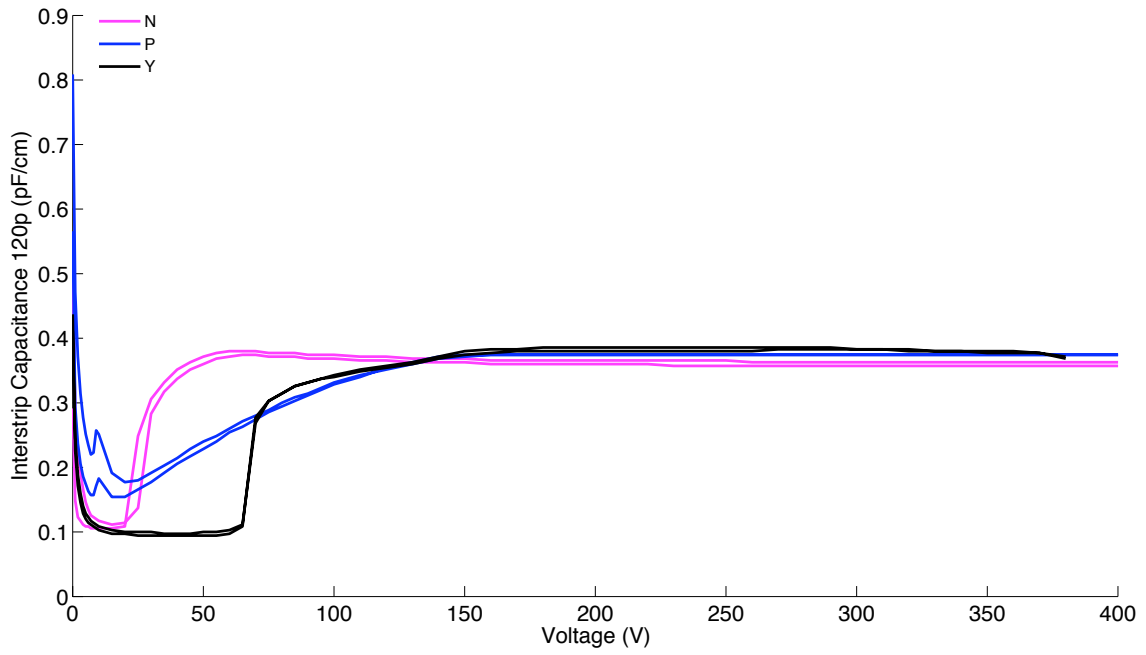
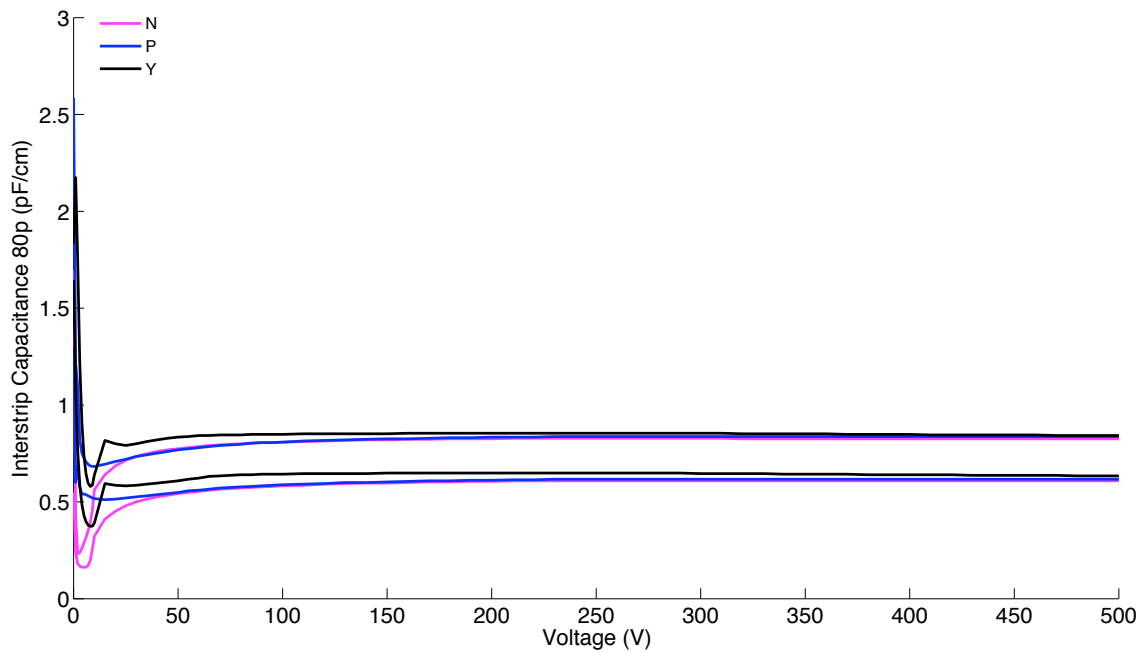**Figure 4.18.:** Cint-V of Epi100, type dependency, T= 20°C

Figure 4.19.: Cint-V of FZ320, type dependency, T= 20°C

4.3.2. Interstrip Resistance (TS cap dc)

The absolute interstrip resistance values are listed in table 4.5 and 4.6. The absolute resistance values are higher at lower temperature as less charge carriers are in the conduction band.

	80_{pitch}	120_{pitch}
	$[k\Omega]$	$[k\Omega]$
FZP 320um	$150E3 \pm 26E3$	$166E3 \pm 60E3$
FZP 200um	105 ± 58	761 ± 139
FZP 120um	31 ± 3	24 ± 2
FZY 320um	$212E3 \pm 193E3$	$167E3 \pm 126E3$
FZY 200um	$13E3 \pm 10E3$	$15E3 \pm 12E3$
FZY 120um	138 ± 21	77 ± 11
FZN 320um	$364E3 \pm 96E3$	$417E3 \pm 122E3$
FZN 200um	$244E3 \pm 67E3$	$275E3 \pm 78E3$
FZN 120um	$269E3 \pm 26E3$	$281E3 \pm 55E3$
MCZP 200um	0.08 ± 0.01	0.08 ± 0.01
MCZY 200um	0.43 ± 0.12	0.45 ± 0.25
MCZN 200um	$167E3 \pm 5E3$	$257E3 \pm 40E3$
EpiP 50um	$183E3 \pm 10E3$	$216E3 \pm 9E3$
EpiY 50um	$393E3 \pm 15E3$	$355E3 \pm 15E3$
EpiN 50um	$374E3 \pm 58E3$	$404E3 \pm 93E3$
EpiP 100um	$83E3 \pm 8E3$	$106E3 \pm 10E3$
EpiY 100um	$122E3 \pm 20E3$	$132E3 \pm 18E3$
EpiN 100um	$292E3 \pm 10E3$	$256E3 \pm 4E3$

Table 4.5.: interstrip resistance results, T= 20°C

The unexpected result of the low MCZ interstrip resistance leads to shorted strips for p types. The same can be said for the thin p type FZ materials whereas the n type resistance value of each material is in the expected range. This discrepancy by three order of magnitudes vanishes for -20°C. The resistance values vary within the first voltage steps, again due to the non fully depleted area beneath the strips whereas the MCZ interstrip resistance stays constant throughout the voltage ramp which is seen in figure 4.21 for Y TS.

There are slight differences for 80 and 120 pitch as a longer resistance should lead to higher absolute values whereas the wave shapes are identical. A similar argument corresponds to the thickness dependency as the resistance to the backplane increases with depletion which is indicated in figure 4.20. The thinner TS should have a slightly higher resistance value. The Epi material confirms this theory whereas the FZ material with the current generated defect of the deep diffusion process does not.

The thickness behavior also depends on type, where the n type FZ show independence, the thicker p type FZ has a higher resistance compared to the thinner ones as seen in figure 4.22 for FZN and 4.23 for FZP.

	80_{pitch}	120_{pitch}
	$[k\Omega]$	$[k\Omega]$
FZP 320um	705E3 ± 155E3	710E3 ± 134E3
FZP 200um	701E3 ± 210E3	713E3 ± 183E3
FZP 120um	236E3 ± 58E3	158E3 ± 88E3
FZY 320um	706E3 ± 166E3	704E3 ± 138E3
FZY 200um	492E3 ± 188E3	633E3 ± 170E3
FZY 120um	300E3 ± 27E3	293E3 ± 64E3
FZN 320um	799E3 ± 154E3	769E3 ± 155E3
FZN 200um	766E3 ± 179E3	756E3 ± 137E3
FZN 120um	403E3 ± 3E3	404E3 ± 122E3
MCZP 200um	250E3 ± 21E3	322E3 ± 68E3
MCZY 200um	222E3 ± 155E3	100E3 ± 131E3
MCZN 200um	741E3 ± 187E3	754E3 ± 120E3
EpiP 50um	391E3 ± 63E3	443E3 ± 14E3
EpiY 50um	511E3 ± 4E3	524E3 ± 9E3
EpiN 50um	564E3 ± 23E3	561E3 ± 2E3
EpiP 100um	466E3 ± 56E3	501E3 ± 39E3
EpiY 100um	495E3 ± 32E3	501E3 ± 6E3
EpiN 100um	502E3 ± 17E3	481E3 ± 38E3

Table 4.6.: interstrip resistance results, T= -20°C
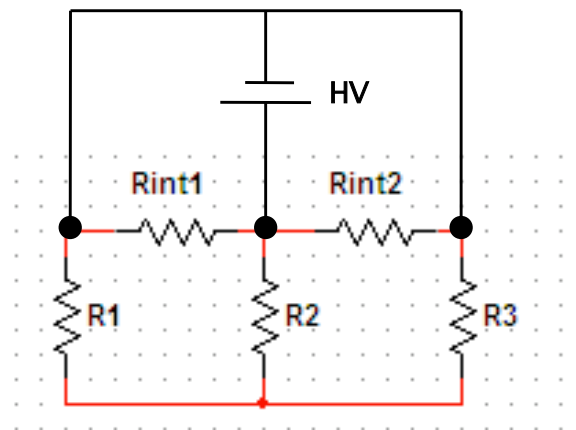

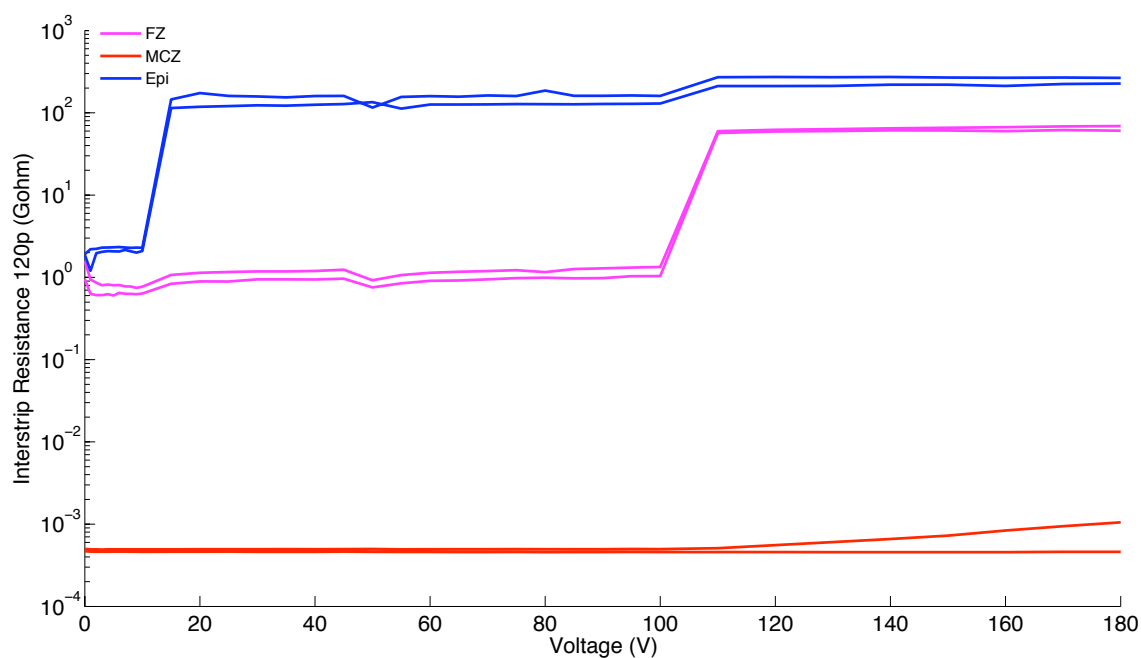**Figure 4.20.:** equivalent circuit diagram of interstrip resistance measurement

Figure 4.21.: Rint-V of Y FZ200, MZC, Epi100, material dependency, T= 20°C

The major difference in type measurement is the missing strip isolation for n types which is seen for the Epi material in figure 4.24 for 50 um and 4.25 for 100 um thick TS. There is a second resistance change for p type TS at about 100V after the depletion zone extended deeper into the bulk and then the values are comparable with n types. The mean value of n types are therefore higher compared to the p types. The Epi material shows this for both P and Y TS whereas the FZ show this more dominant for Y ones which is seen in figure 4.26. The measurement artifact at about 50V for one of the FZ320 results can be ignored.
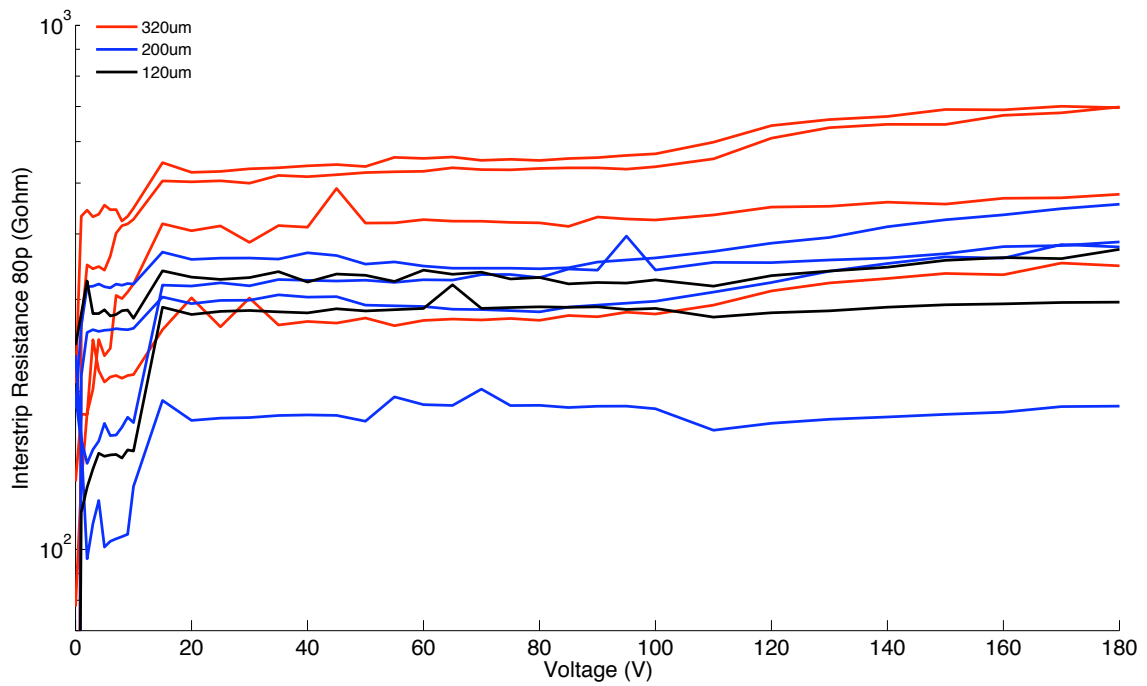
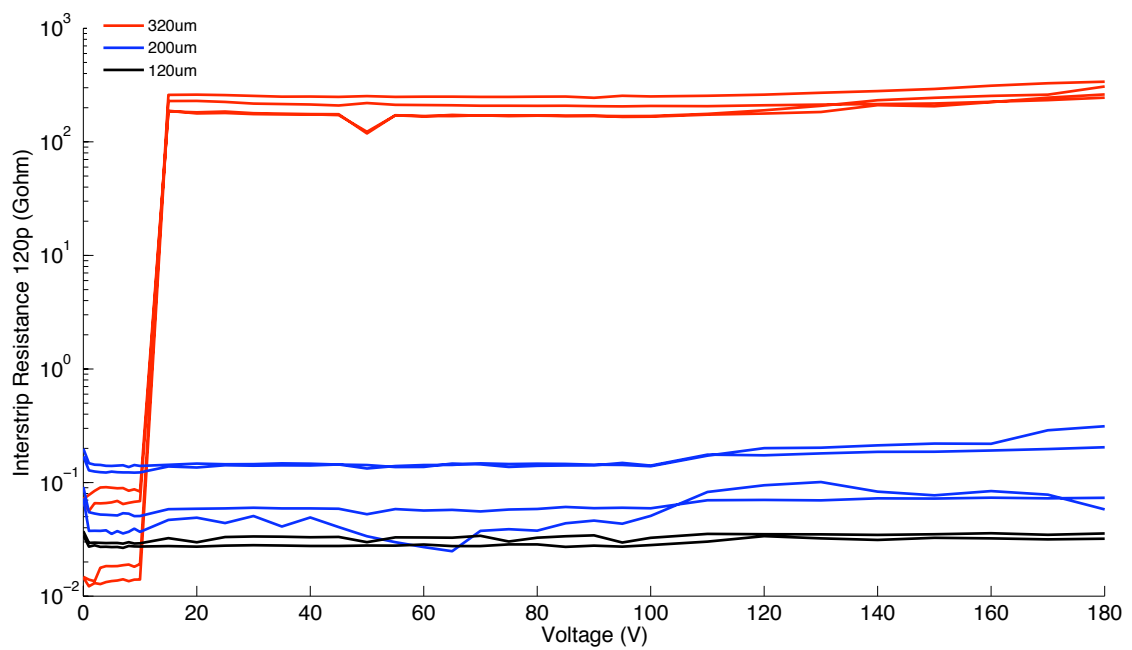**Figure 4.22.:** Rint-V of FZN, thickness dependency, T= 20°C

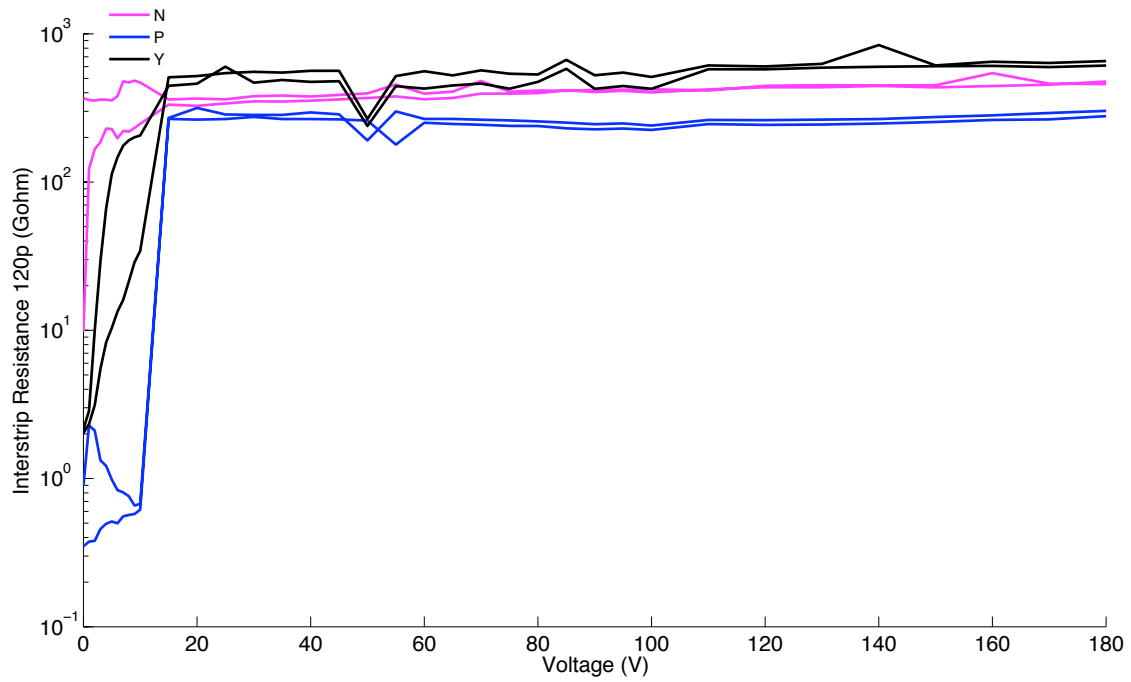**Figure 4.23.:** Rint-V of FZP, thickness dependency, T= 20°C

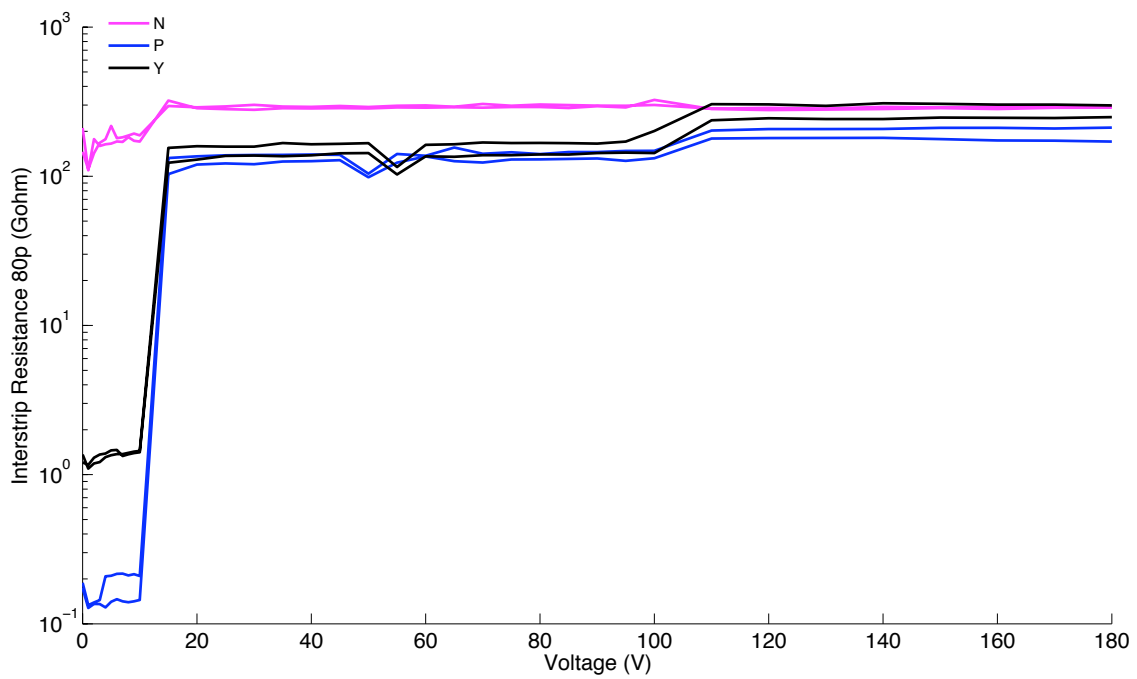**Figure 4.24.:** Rint-V of Epi50, type dependency, T= 20°C

Figure 4.25.: Rint-V of Epi100, type dependency, T= 20°C
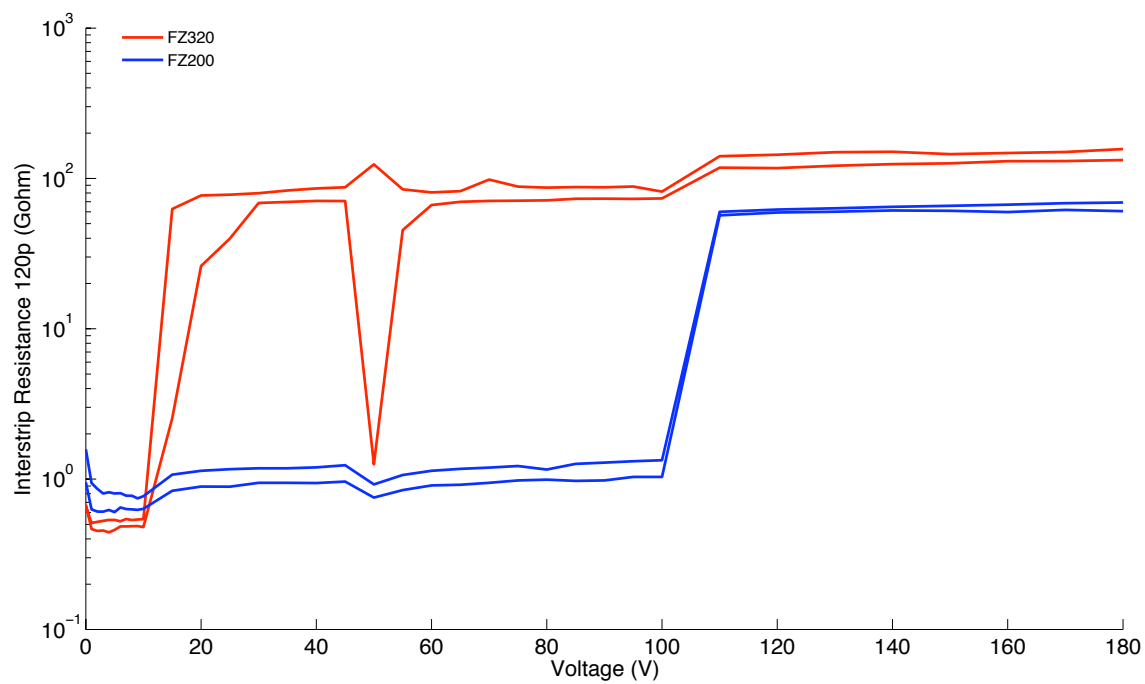
Figure 4.26.: Rint-V of FZY, T= 20°C

4.3.3. Coupling Capacitance (TS cap)

The dielectric of the strips consists of a layer of SiO_2 and a thin layer of Si_3N_4. The oxide thickness d_{O_2} can be calculated with the measured capacitance C_{meas} and equation 4.6 [3] where the thickness of Si_3N_4 layer is assumed with $d_{N_4} = 50$ nm. This leads for all materials to 288.05 ± 9.41 nm and conforms with the result of electron-microscopy of 270 nm, given in [7].

$$d_{O_2} = \varepsilon_0 \cdot \varepsilon_{Si_{O_2}} \cdot \left(\frac{A_{cap}}{C_{meas}} - \frac{d_{N_4}}{\varepsilon_0 \cdot \varepsilon_{Si_3N_4}} \right) \qquad (4.6)$$

The results are listed in table 4.7 which are independent of temperature, material and thickness but there is a slight difference in types. The mean value of the n type capacitance is less than the one of p type due to different mobility of the charge carriers measured at the same frequency.

	T= 20°C	T= -20°C
	[pF]	[pF]
FZP	22.4 ± 0.4	22.4 ± 0.3
FZY	22.2 ± 0.3	22.1 ± 1.1
FZN	21.5 ± 0.8	22.1 ± 0.5
MCZP	22.6 ± 0.1	22.8 ± 0.3
MCZY	22.0 ± 0.5	23.0 ± 1.2
MCZN	21.0 ± 0.2	20.9 ± 0.2
EpiP	21.8 ± 0.4	22.0 ± 0.4
EpiY	22.0 ± 0.3	22.4 ± 0.3
EpiN	21.7 ± 0.2	22.2 ± 0.9

Table 4.7.: coupling capacitance results, T= $\pm$20°C

4.3.4. Dielectric Break Down Voltage (TS cap)

A voltage is applied to the dielectric until breakdown occurs. This measurement causes irreversible damages which cannot be performed on the real detector. The mean value for n type TS cap is $247 \pm 7V$ and $-248 \pm 13V$ for p type. Table 4.8 shows that the results are independent of temperature, material and thickness.

	T= 20°C	T= -20°C
	[V]	[V]
FZP	-251.0 ± 7.4	-238.0 ± 31.2
FZY	-248.0 ± 4.2	-249.0 ± 3.2
FZN	249.0 ± 3.2	241.0 ± 3.2
MCZP	-250.0 ± 0.0	-250.0 ± 0.0
MCZY	-247.5 ± 5.0	-250.0 ± 0.0
MCZN	265.0 ± 5.8	260.0 ± 0.0
EpiP	-250.0 ± 8.2	-245.0 ± 5.8
EpiY	-255.0 ± 12.9	-255.0 ± 12.9
EpiN	252.5 ± 9.6	240.0 ± 0.0

Table 4.8.: dielectric break down results, T= $\pm$20°C

4.4. Resistivity Values

4.4.1. Implants, Aluminum, Polysilicon (TS sheet)

For the aluminum and polysilicon resistance measurement, depletion is not needed as the results are independent of the applied bias voltage whereas the implant resistance changes until the area of the implants is full depleted. A bias ring at the TS sheet is not provided and this causes problems with applying an essential bias voltage. In case of the measurement of the p stop implant on a p bulk, no p-n junction can be generated as there are only contact windows for a p+ in p connection. The same can be said for n implant measurements on n bulk. The mean values are listed in table 4.9.

	T=20°C	T=-20°C	
polysilicon	2.98 ± 0.48	3.50 ± 0.62	$[k\Omega/sq]$
aluminum	27.00 ± 1.65	22.07 ± 1.84	$[m\Omega/sq]$
p+ implant	121.73 ± 0.54	120.42 ± 1.58	$[\Omega/sq]$
n+ implant	30.92 ± 0.37	29.81 ± 0.85	$[\Omega/sq]$

Table 4.9.: sheet resistivity mean value, T= ± 20°C

The n+ and p+ implant results are plotted in figure 4.27 and 4.28 where the p+ implant is only measured on N and the n+ implant only on P and Y. The implant resistivity shows no material or thickness dependency. The slight difference in temperature is seen for n+ implant results where the lower values correspond to the measurement at T= -20°C.

The polysilicon and aluminum results are seen in figure 4.29 and 4.30. The aluminum, as it represents a metal, has a higher resistance at higher temperature whereas the polysilicon resistance, as a highly doped semiconductor, is lower at higher temperature. There is a dominant material dependency for the polysilicon results as the eight highest values in figure 4.30 correspond to the MCZ material.
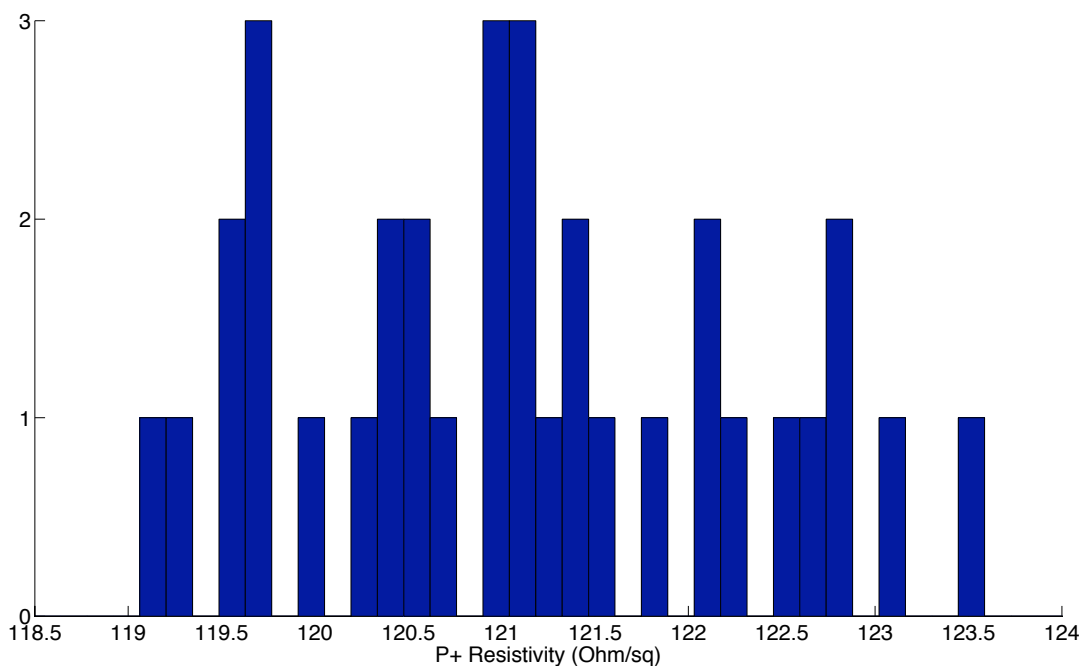
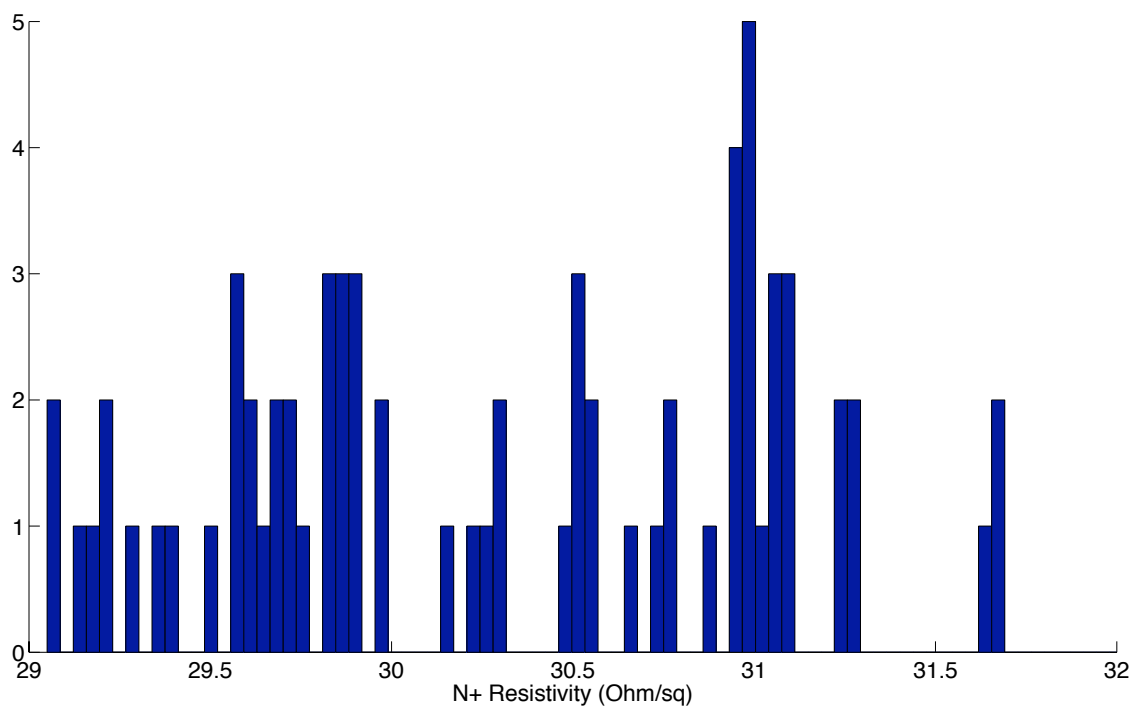**Figure 4.27.:** p+ implant measured on n type, T=± 20°C

Figure 4.28.: n+ implant measured on p type, T=± 20°C
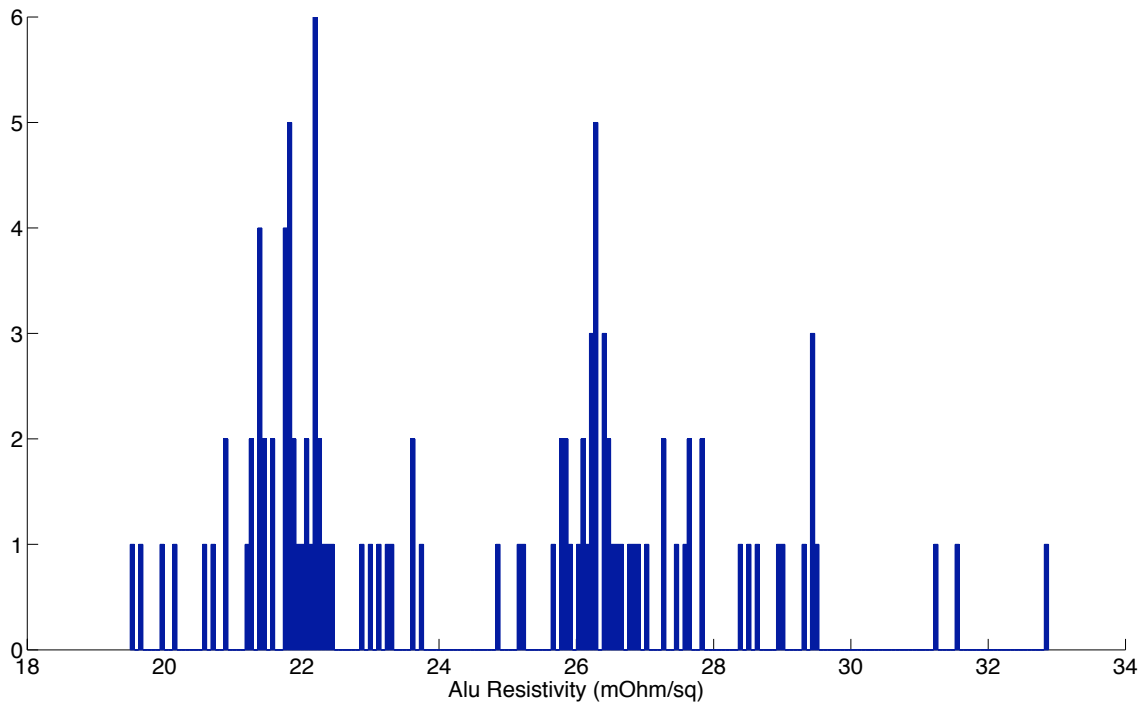
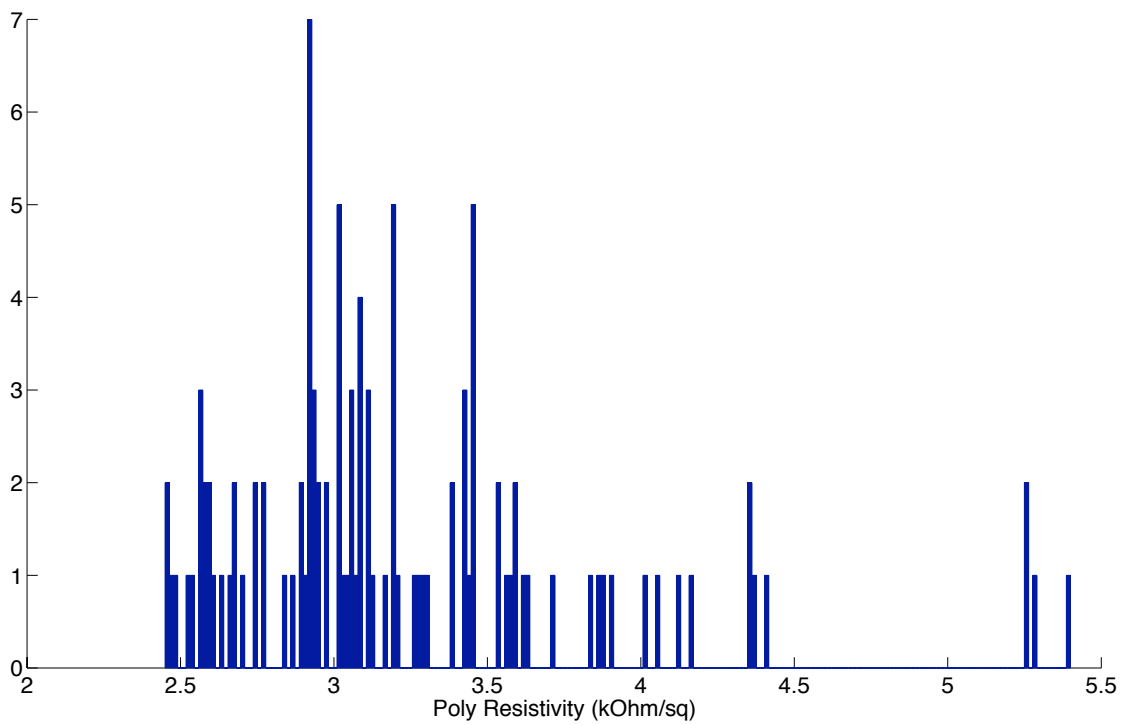**Figure 4.29.:** aluminum resisitvity, T=± 20°C

Figure 4.30.: polysilicon resistivity, T=± 20°C

4.4.2. Via (TS via)

The circuit scheme is equivalent to the implant measurement at TS sheet but the resistance here consists of 40 implants, 40 aluminum pads and 80 VIAs in series. For the determination for one single VIA the resistivity values for implants and aluminum can be taken from the measurement results of TS sheet. Only a rough calculation can be done as especially the implants do not follow the ohmic laws. The values corresponding to one single VIA are seen in table 4.10.

The resistance value for one VIA should be about 67 Ω which is invalid as e.g. the total resistance of the double metal layer taken from VIA2 is only about 10 Ω (as described in chapter 4.5.1). This rough calculation only shows that the different resistance values for each type are sensible.

$$
\begin{aligned}
sq_{implant} &= 151 \\
sq_{aluminumpad} &= 142 \\
\rho_{p+} &= 31 \quad \Omega/sq \quad \text{measured on n type} \\
\rho_{n+} &= 122 \quad \Omega/sq \quad \text{measured on p type} \\
\rho_{aluminum} &= 27 \quad m\Omega/sq \\
R_{n+} &= 18.4 \quad k\Omega \quad \text{measured on p type} \\
R_{p+} &= 4.7 \quad k\Omega \quad \text{measured on n type} \\
R_{aluminum_{pad}} &= 3.5 \quad \Omega
\end{aligned}
$$

$$
\begin{aligned}
R_{VIA1_P} &&&&&&= 42 \quad k\Omega \quad \text{measured on p type} \\
R_{VIA1_N} &&&&&&= 15 \quad k\Omega \quad \text{measured on n type} \\
\text{R per VIA} &= R_{VIA1_P}/80 - R_{n+}/40 - R_{aluminum_{pad}}/40 &&= 64 \quad \Omega \quad \text{measured on p type} \\
\text{R per VIA} &= R_{VIA1_N}/80 - R_{p+}/40 - R_{aluminum_{pad}}/40 &&= 70 \quad \Omega \quad \text{measured on n type}
\end{aligned}
$$

Table 4.10.: rough calculation for one single via resistance

The results of the resistance measurement is seen in figure 4.31 and 4.32, where the measurements on p type show a very high statistical deviation which is not understood. Trends in terms of thickness or material for p type is not stated due to the high uncertainty. There is a material dependency on n types as the MCZ resistance values are higher compared to the FZ and those are higher compared to the Epi. The absolute mean values are listed in table 4.11.

	T=20°C	T=-20°C	
on n type	14.99 ± 0.56	15.20 ± 0.59	$[k\Omega]$
on p type	42.10 ± 5.41	46.27 ± 7.39	$[k\Omega]$

Table 4.11.: via resistance mean value, T= ± 20°C
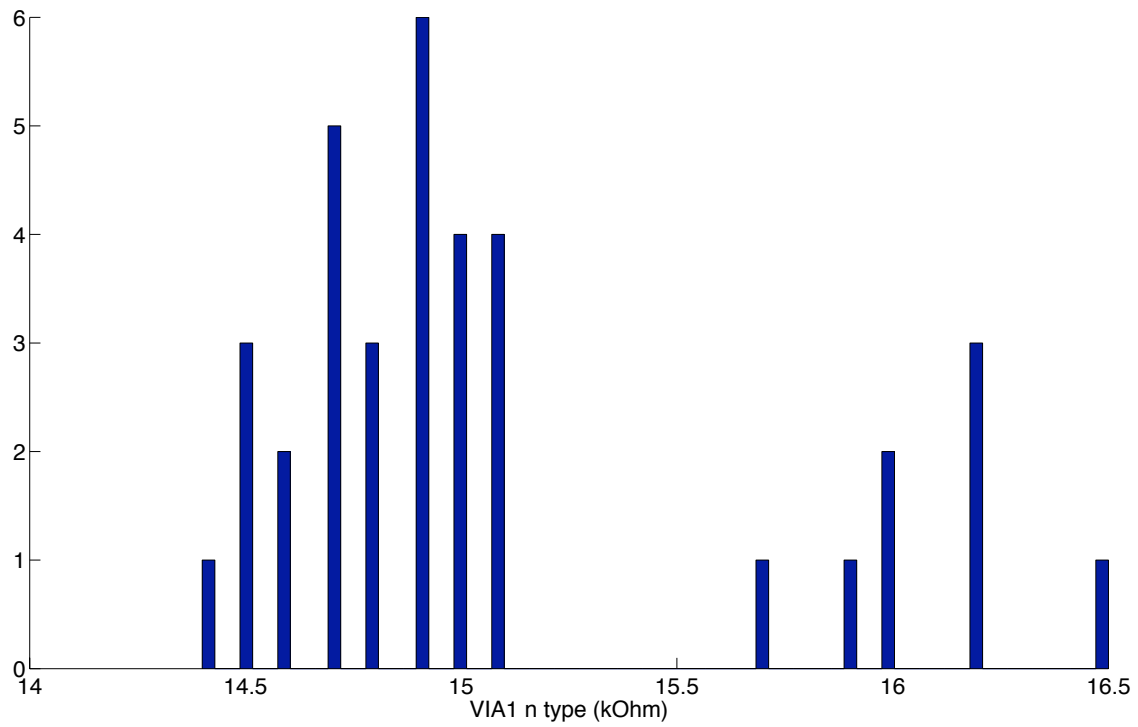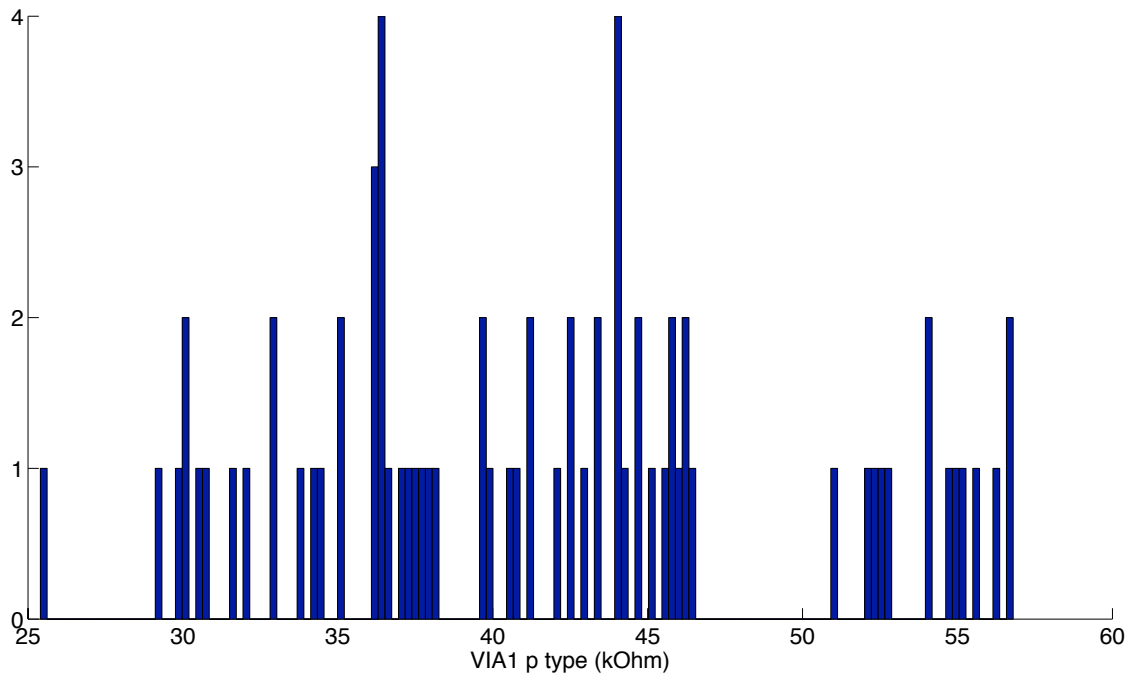
Figure 4.31.: via resistance measured on n type, T=± 20°C

Figure 4.32.: via resistance measured on p type, T=± 20°C

4.5. Double Metal Test Structures

Double metal refers to the *2nd metal* TS in table 1.1 where direct routing on the detector is performed. Additional process steps are introduced as also a second oxide layer for isolating the two metal layer from each other is needed. There are three TS where the results differ from them of non double metal TS, the MOS TS which is described in chapter 4.6.3, an additional TS VIA2 which leads to the aluminum connector between the two metal layers and the aluminum resistivity at the sheet TS measurements.

4.5.1. VIA2

VIA2 is indepent of type as the resistance measurement is aluminum only. This TS consists of a complex resistance network which is seen in figure 4.33. The simulated value of 6Ω leads to the expected value of $2 \cdot R_{aluminum_{pad}} = 7\Omega$ in table 4.10.
The mean value of the VIA2 measurement is $10.60 \pm 1.26\Omega$ (T=20°C), measured with 4 wire sense mode. The contact resistance of a few Ω has to be taken into account when measuring low resistances which leads to the agreement with simulation.

4.5.2. Resistivity Values (sheet)

As given from the design, the second metal layer is only implemented at the contact pads which is indicated in figure 4.34. Therefore the same resistivity value of $27.00 \pm 1.65 m\Omega/sq$ (T=20°C) for aluminum is expected but the mean value for double metal TS is $53.94 \pm 0.87 m\Omega$ /sq (T=20°C). This measurement result is not yet understood.
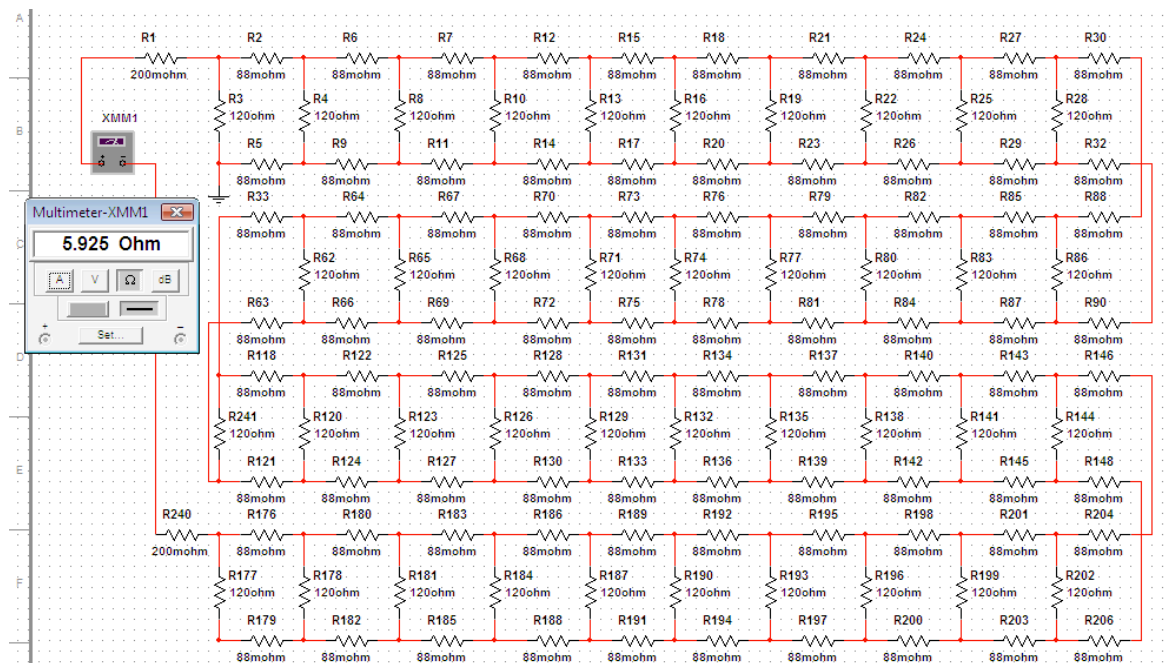
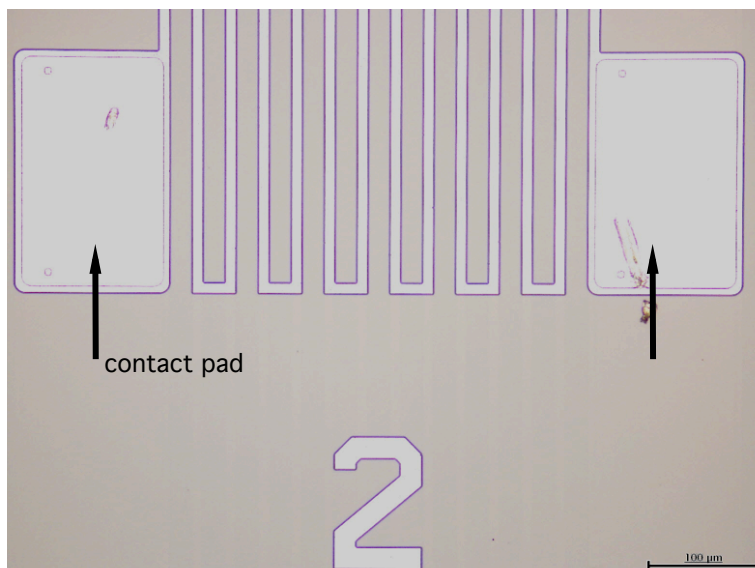**Figure 4.33.:** double metal VIA2 simulation with MULTISIM

Figure 4.34.: photo of double metal aluminum sheet

4.6. Metall Oxide Semiconductor

4.6.1. Charge Oxide Concentration (TS mos)

The oxide of the MOS capacitance is the same SiO_2 oxide layer as used for the coupling capacitance. During manufacturing positive charges can be generated which leads to problems during operation. The interface charges in the oxide react to an applied voltage where the different MOS condition accumulation, flatband and depletion are defined. This is indicated in figure 4.35 where also the circuit scheme for p type bulk is seen. The measurement correspond to two capacitance in series, the semiconductor C_S and the oxide capacitance C_{ox}:

$$\frac{1}{C} = \frac{1}{C_S} + \frac{1}{C_{ox}}$$

(4.7)

Applying a negative voltage, the semiconductor has a higher potential compared to the metal and therefore holes as majority carriers are accumulated beneath the oxide. In this case C_S is much higher compared to C_{ox} and can be neglected. C_S gets smaller with applying a more positive voltage, as the holes are depleted and therefore the capacitance decreases. If no voltage is applied, the conduction and valence band of the semiconductor are not bended. Due to the positive oxide charges this condition of flat bands is shifted away from 0V.

All trends in terms of material, thickness or temperature are the same for N and P. The behavior of Y TS is discussed in the chapter 4.6.2. There is a slight material dependency only in the accumulation condition where the MCZ P capacitance is higher compared to the others. The curves leading to the depletion condition depends on temperature as the temperature dependency of the mobility of the charge carriers is more dominant at the non equilibrium state between flatband and depletion.

The results are seen in figure 4.36 for N TS at different temperature. The two trends seen in depletion leads to different temperature. The wave shape between flatband condition and depletion is not smooth due to non equilibrium states at fast measurements which is seen in figure 4.37 for P TS.

The charge oxide concentration can be calculated with the equation 4.8 where C_{Ox} correspond to capacitance value while accumulation, ϕ to the working function and V_{fb} to the flatband voltage. The assumed values for the working function are taken from figure 10.23 in [10] and it is ϕ_{ntype}= -0.5 V for N TS and ϕ_{ptype}= -0.7 V for P TS. N_{Ox} for N TS leads to 1.75E10 $\pm$ 1.58E9 cm^{-2} and for P to 6.22E10 $\pm$ 1.33E10 cm^{-2}.

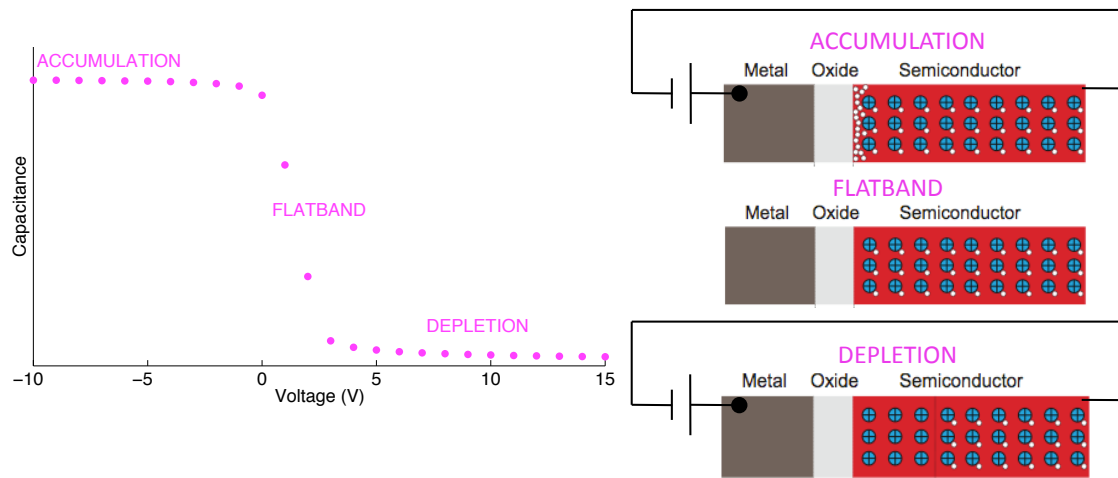$$N_{Ox} = \frac{C_{Ox}}{e \cdot A_{cv}} \cdot (\phi + V_{fb})$$

(4.8)

Figure 4.35.: MOS condition with p type measurement circuit [4]
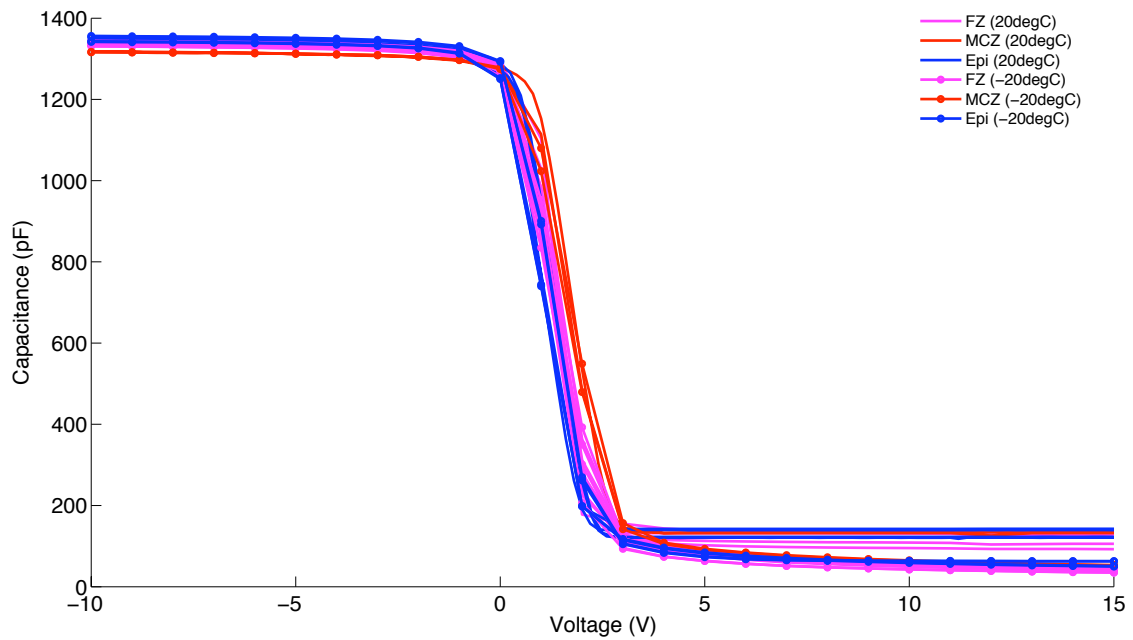
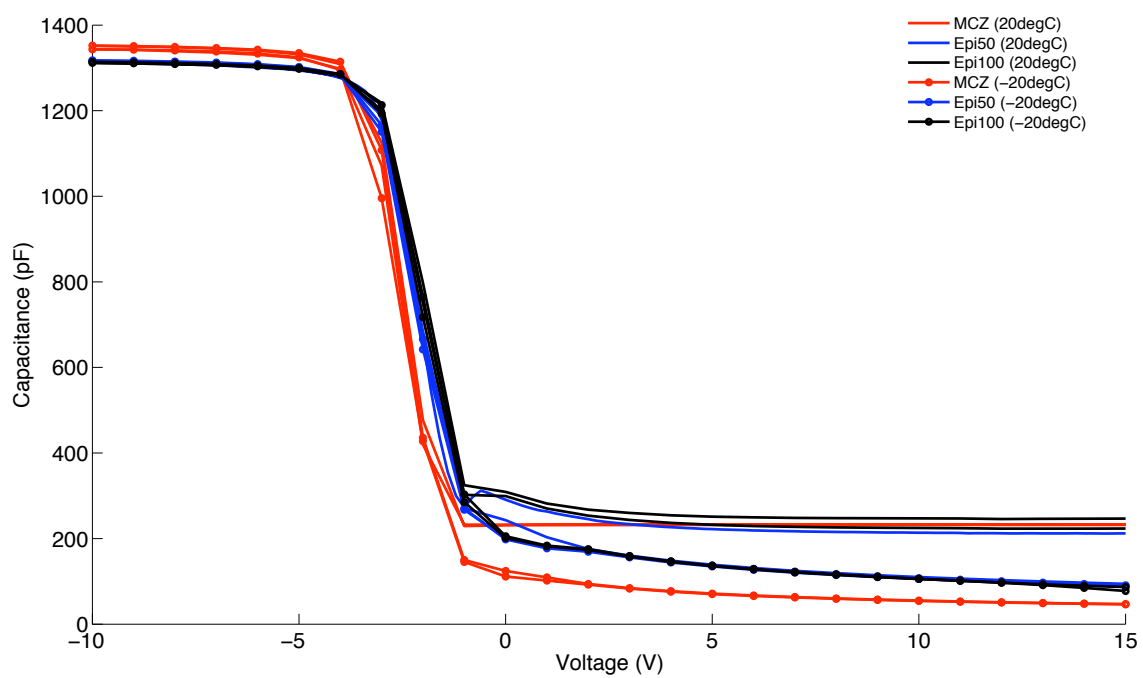

Figure 4.36.: CV mos N, temperature dependency, T=$\pm$ 20°C

Figure 4.37.: CV mos P, material dependency, T=± 20°C

4.6.2. Pspray Thickness (TS mos)

The measurement parameter are the same as listed in the previous section except for voltage step and wait time. For the Y MOS TS, the CV wave shapes depend on how fast the measurements are performed.

In figure 4.38 the different CV curves depending on ramp rates RR are seen where the wave shapes also differ when using the same RR but different voltage steps. The results of the FZ120Y and MCZ200Y are comparable with figure 7.31 in [11]. The doping concentration is higher for the p spray layer compared to the p bulk which introduces more charge carriers. This leads to a higher depletion capacitance with slow measurements where it correspond to an equilibrium state.
The results of FZ320Y and Epi50Y lead to a kink within the CV characteristic where it seems that after this kink it passes over to the CV characteristic of a P MOS TS.

An overview of RR corresponding to fast and slow measurements is listed in table 4.12 for each TS. At high RR there is a kink whereas a slow measurement leads to a smooth wave shape. The wave shapes also differ depending on thickness and material.

	w/o kink	kink
	RR	RR
	[V/s]	[V/s]
Epi50Y	0.01	1
Epi100Y	0.01	1
FZ120Y	0.2	10
FZ200Y	0.2	10
FZ320Y	0.02	10
MCZ200Y	1	10

Table 4.12.: used ramp rates RR corresponding to a kink and without (w/o) a kink in CV mos at T=20°C

The depletion grows a few microns into the semiconductor [10]. The idea is that this kink corresponds to the interface between p spray and p bulk. At low RR, which correspond to a slow measurement, the charge carriers have enough time to reach equilibrium. Fast measurement, using high RR, lead to non-equilibrium. In case of slow measurements the depletion capacitance is much higher compared to the absolute depletion capacitance at fast measurements. Therefore in non-equilibrium case the charge carriers also enter in the p bulk whereas for equilibrium the depletion stays within the p spray layer. An overview of fast and slow measurement is seen in figure 4.39. In non-equilibrium case the capacitance values before the kink refer to the p spray layer and after the kink to the p bulk. The capacitance value at the knee is a parameter for the thickness of p spray and with assuming a plate capacitance this leads to the following equation:

$$C_d = \frac{C_{kink} \cdot C_{ox}}{C_{ox} - C_{kink}} = \frac{\varepsilon_0 \cdot \varepsilon_{Si} \cdot A_{cv}}{d_{pspray}} \tag{4.9}$$
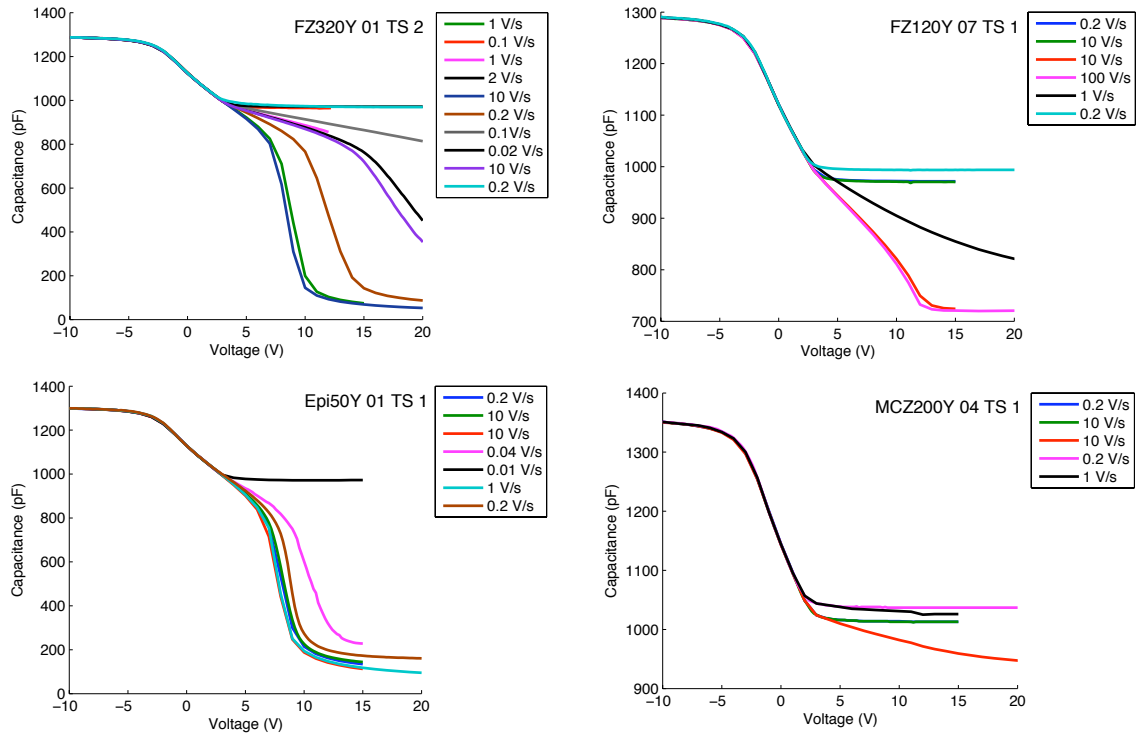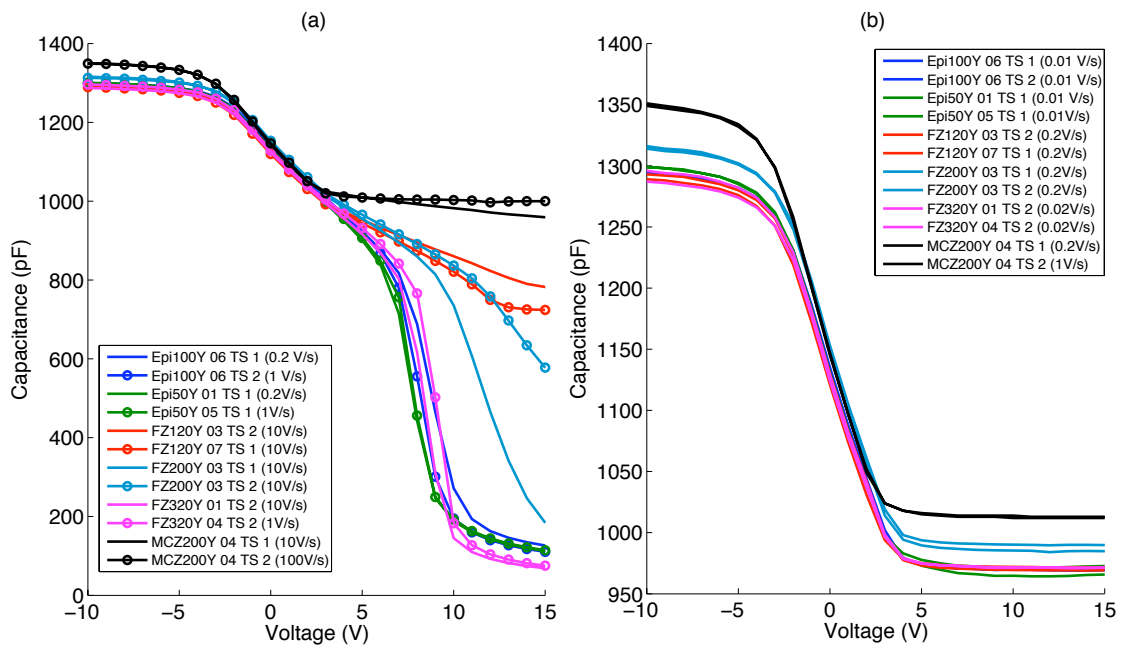
Figure 4.38.: CV mos ramp rate dependency, T=20°C

Figure 4.39.: CV mos comparison of (a) fast and (b) slow measurement, T=20°C

There are three references that this calculation for the thickness is valid. The profile scan from the Spreading Resistance Profiling (SRP) measurement in [7] shows similar values for the thickness. The wave shape in non-equilibrium case depends on the RR due to the different mobility in the different materials whereas the kink corresponds always to the same capacitance value. Also the temperature dependency shows a constant kink value which is seen in figure 4.40. All measurements at T=-20°C show a kink, as very slow measurements would be needed for smooth wave shapes. This temperature effect is very dominant for MCZ and Epi material, as seen in figure 4.40 (b) where the same ramp rates at different temperature causes a smooth shape at T=20°C and kinks at T=-20°C. The temperature dependency of mobility causes this discrepancy. An overview of the calculated thicknesses and RR is listed in table 4.13 with the mean value of the p spray thickness of $1.21 \pm 0.11 \mu m$.
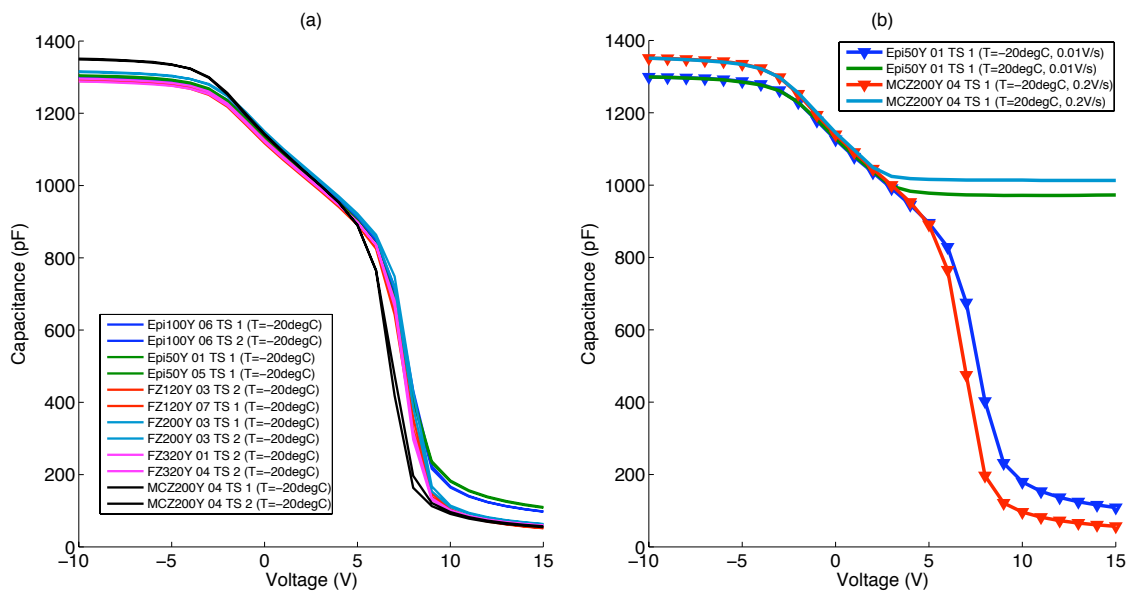

Figure 4.40.: CV mos (a) fast measurement, T=-20°C, (b) the used RR is the same for each temperature, T= ± 20°C

	T=20°C		T=-20°C	
	RR	d	RR	d
	[V/s]	[um]	[V/s]	[um]
Epi50Y_01_TS_1	0.2	1.11	1	1.14
Epi50Y_05_TS_1	1	1.10	1	1.14
Epi100Y_06_TS_1	0.2	1.21	1	1.12
Epi100Y_06_TS_2	1	1.34	1	1.10
FZ120Y_07_TS_1	10	-	10	1.11
FZ120Y_03_TS_2	10	-	10	1.16
FZ200Y_03_TS_2	10	1.21	10	1.12
FZ200Y_03_TS_1	10	1.28	10	1.32
FZ320Y_01_TS_2	10	1.28	1	1.12
FZ320Y_04_TS_2	1	1.47	1	1.13
MCZ200Y_04_TS_1	10	-	0.2	1.37
MCZ200Y_04_TS_2	100	-	1	1.37

Table 4.13.: overview of used ramp rate RR and calculated p spray thickness d

4.6.3. Double metal (TS mos)

The double metal capacitance C_{dm} has to be taken in account in equation 4.7 and so the measured capacitance leads to

$$\frac{1}{C} = \frac{1}{C_S} + \frac{1}{C_{ox}} + \frac{1}{C_{dm}} \tag{4.10}$$

The design picture of the double metal mos TS is seen in figure 4.41. The top layer consists of two aluminum pads where the smaller pad connects to the non DM mos TS and the pad with the greater area to the mos TS with the additional oxide layer. Apart from measuring two different mos structures, the double metal capacitance C_{dm} can be determined. The results are listed in table 4.14 which are measured at 1 kHz. This leads to a mean value of 674.0 ± 10.6 pF.
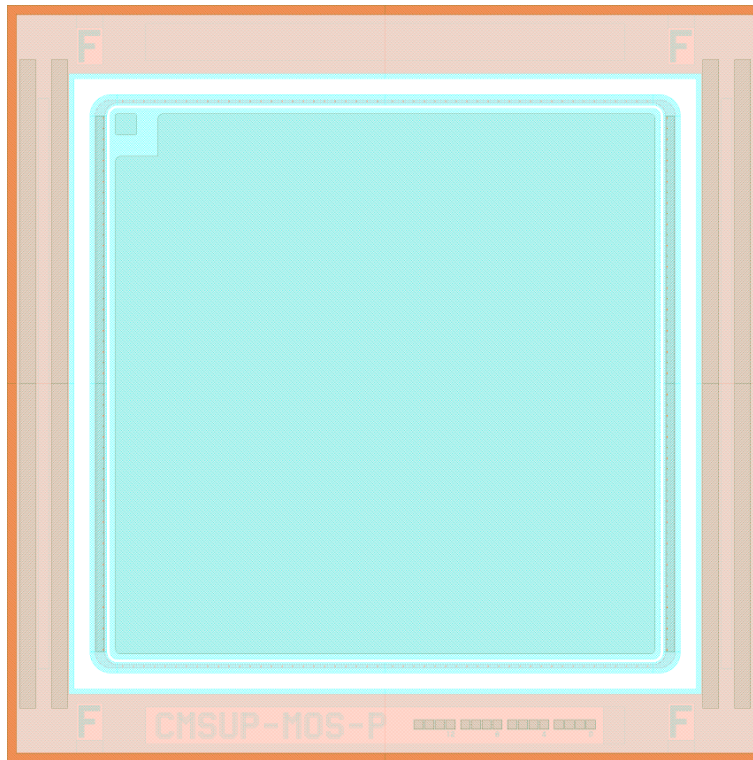

Figure 4.41.: design picture of double metal mos TS

	C_{dm}
	[pF]
F200DN 02 TS 2	685
F200DN 04 TS 1	667
F200DP 04 TS 1	673
F200DP 04 TS 2	689
F200DY 08 TS 1	664
F200DY 04 TS 1	666

Table 4.14.: double metal capacitance C_{dm}, T=20°C

The double metal CV results are seen in figure 4.42 where the mean value of the flatband voltage for N is about $5V$ and for P $-4V$. This flatband voltage of $-4V$ compared to the typically $-1V$ points to a higher C_{ox}. The measured capacitance value in accumulation is dominated by C_{dm} as the expected C_{ox} is about 1 nF. This situation is even worse at the other conditions as the semiconductor capacitance is not neglectable anymore. The capacitance changes during the voltage ramp is less than compared to results of non double metal TS.

With equation 4.10 and the measurement results, C_{ox} can be determined as for the accumulation condition C_S can be neglected. The mean value of the measured capacitance is 450 pF and this leads to $C_{ox} = 1354$ pF which is comparable with the C_{ox} results in figure 4.36 and 4.37.
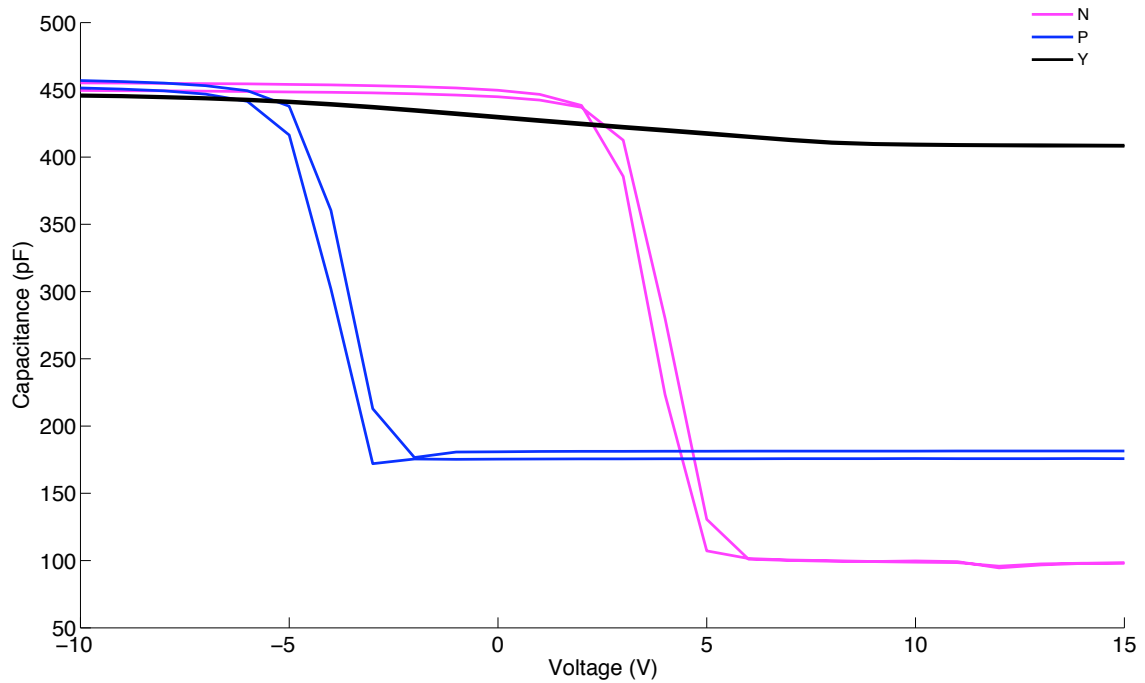

Figure 4.42.: CV mos of FZ double metal TS, T=20°C

5. Results of Irradiated Test Structures

The irradiation sources within the campaign are the nuclear reactor in Ljubljana and the synchrotron in Karlsruhe. Prospective neutron irradiation can also be performed at the reactor at the ATI (*Atominstitut*) in Vienna. As first investigation with the new irradiation facility mainly diodes are irradiated to have a comparison with literature. All equations and fitting parameters are taken from [5].

5.1. Irradiation Facility

The reactor type at ATI is a TRIGA Mark II, which stands for Training- Research- Isotope Production and General Atomic. The maximum thermal power is 250kW continuous and 250MW pulsed for 40ms. Neutrons have to be slowed down by a moderator in order to enhance the possibility for fission. There are 80 fuel elements in the reactor core. Those elements consist of a aluminum or steel cladding, 8% uranium fuel and 92% zirconium-hydride moderator. The fuel temperature during continuous operation is 200°C and about 360°C in pulsed operation. The maximum neutron flux is $1 \cdot 10^{13} cm^{-2} s^{-1}$ at 250kW and $1 \cdot 10^{16} cm^{-1}$ at 250MW [13]. The reactor remains sub-critical if the neutrons from a start-up source are absorbed. To increase the power, the number of fission has also to increase by taking the control rods out of the core. There are three control rods which consists of boron carbide. It takes roughly one minute to reach 250kW.

5.2. Diode Irradiation

The initial irradiation test was performed only on diodes. Two different irradiation tubes are tested, the wet tube ZBR (*Zentrales Bestrahlungs Rohr*) and the dry tube TBR (*Trockenes Bestrahlungs Rohr*). At the ZBR the diodes are mounted with a cord and this causes varying neutron flux. Also the flux at ZBR is unknown from ATI at that moment and therefore the analysis is only done with the irradiated diodes from TBR.
The irradiation time was 20 minutes and 50 seconds at a thermal power of 100 kW. The diodes are annealed for four minutes and 60 minutes at 80°C and have been measured after each time window. The annealing at 30°C during and after irradiation is negligible.
The measurement parameter are the same as given chapter 4.1.1 but for a better comparison with literature, the guard ring of the diode is connected with the ground potential. The hardness factor can be calculated with the IV results before and after irradiation which is shown in figure 5.1. The current after irradiation increases as expected and in this case by the order of four magnitudes. The

equivalent neutron fluence is calculated with equation 2.3. The mean values of the four diodes for
the two different annealing times are:

$$
\begin{aligned}
\Phi_{eq4min} &= 2.98e^{12}cm^{-2} \\
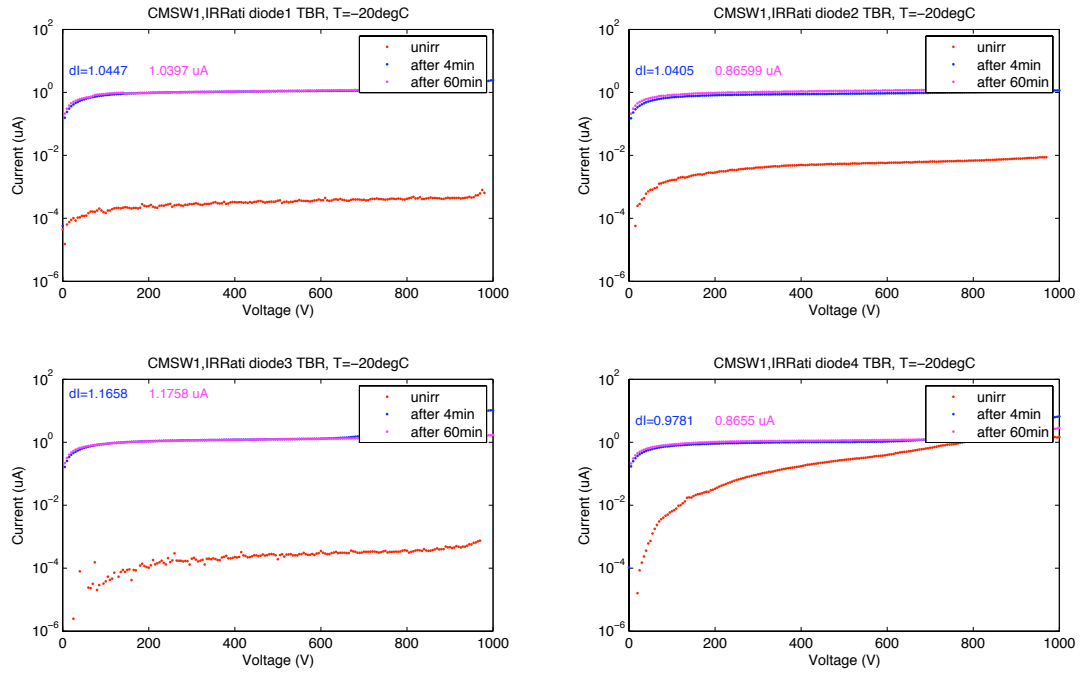\Phi_{eq64min} &= 4.17e^{12}cm^{-2}
\end{aligned}
$$

Figure 5.1.: IV analysis before and after irradiation, T=-20°C

The depletion voltage U_{depl} changes due to the differences of mobility and resistivity after irradia-
tion which is seen in figure 5.2. With the depletion voltage extracted from CV plots, the effective
doping concentration N_{eff} can be determined with equation 2.9.
N_{eff} is determined by the defects within the band gap and therefore depends on the used fluence
and annealing. The effective doping concentration can also be calculated with equation 2.5 where
Φ_{eq} is given from the current change ΔI from IV measurements.
This leads to an agreement between IV and CV measurements:

$$
\begin{aligned}
|\Delta N_{effCV}| &= 1.34e^{12}cm^{-3} \\
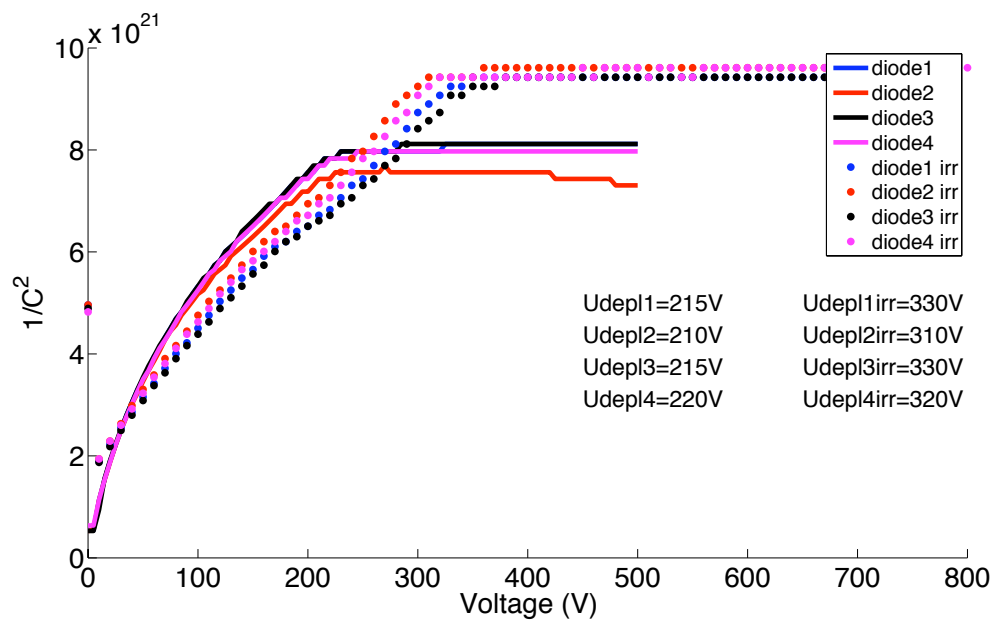|\Delta N_{effIV}| &= 2.67e^{12}cm^{-3}
\end{aligned}
$$

Figure 5.2.: CV analysis before and after irradiation, T=-20°C

5.3. Halfmoon Irradiation

An overview of the irradiation parameters is seen in table 5.1 where also the low fluency dry tube W (*Weberbestrahlungsrohr*) has been used. The irradiation in the W tube is dominated by thermal neutrons compared to spectrum in the *Trocken Bestrahlungs Rohr* TBR tube. The TBR is located nearer the reactor core and therefore more dominated by fast neutrons.

TS	tube	time	power	fluency
		[min]	[kW]	[cm-2]
FZ120N 06 TS 2	TBR3	25	100	1.30E15
FZ120N 09 TS 2	TBR2	10	100	4.70E14
FZ200N 03 TS 1	TBR2	25	100	1.18E15
FZ200N 03 TS 2	W2	10	100	1.44E14
FZ320N 03 TS 1	TBR1	25	100	1.04E15
FZ320N 08 TS 1	TBR1	10	100	4.18E14
30221541401206	TBR5	10	20	0.99E14
30221541401207	W1	10	20	0.29E14
30221541401208	TBR5	10	30	1.48E14
30221541401210	W1	10	30	0.43E14
30221541401211	TBR5	10	50	2.47E14
30221541401213	TBR5	10	70	3.46E14
30221541401214	TBR5	15	250	1.85E15
30221541401215	W1	15	250	5.40E14

Table 5.1.: overview of the second irradiation at ATI

5.3.1. Increase of Dark Current

The second irradiation was done with Halfmoons where the calculation differs from that above as different fluencies are used. The slope of the current change over fluence corresponds to the current related damage rate α.

The expected value for α is taken from figure 2.8 with the same annealing steps as described in the previous section. The hardness factor has to be taken into account as the slope in figure 5.3 is represented by $\alpha = \Delta I / V \cdot \Phi \cdot \kappa$. The unirradiated measurements of IV diode are always performed without a guardring connection. There is also an investigation only with the FZ labeled diodes whether there are major differences in the analysis results depending on the measurements with and without ground connection. The IV curves are identical after 4 minutes of annealing and differ in absolute current values after 60 minutes of annealing. The dark current of guard ring connected diodes are lower compared to the non-connected ones and the diodes break down earlier. The κ value can be compared in more detail as α depends on annealing temperature and there is a slight difference in terms of guard ring connection.

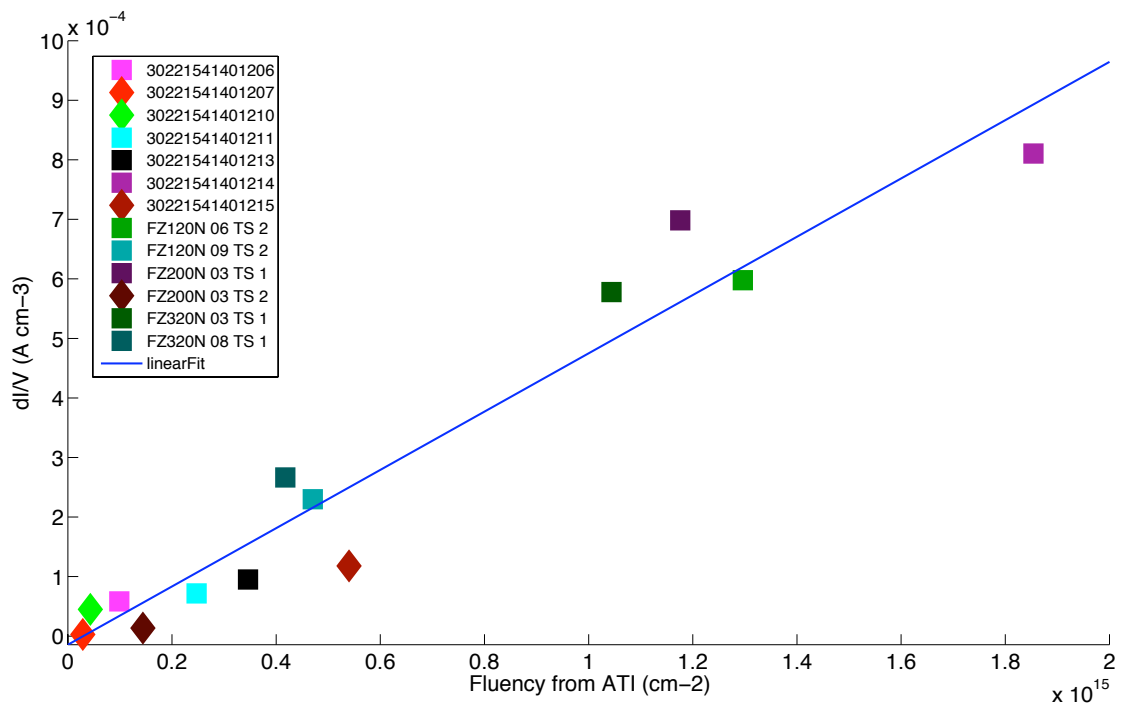|		
α_{64min} (expected)	=	3.1E-17 A/cm
$slope_{64min}$ (from FIT)	=	5.9E-19 A/cm
with guardring connection	(only FZ labeled diodes)	
κ_{TBR}	=	0.020 ± 0.0022
κ_W	=	0.0028 ± 0.0003
without guardring connection	(only FZ labeled diodes)	
κ_{TBR}	=	0.018 ± 0.0024
κ_W	=	0.0029 ± 0.0004

Figure 5.3.: measured current related damage value, T=-20°C

5.3.2. Change of Depletion Voltage

The effective doping concentration N_{eff} is also compared at different fluencies. The result is seen in figure 5.4 where the simplified equations 2.5 - 2.9 for the fit are used and stable annealing N_c is not taken into account. The results only from the TBR irradiation are taken for fitting as the neutron spectrum differs for the different tubes and this would lead to a further uncertainty for analysis. The change of the effective doping concentration can be compared with figure 2.10 taken from literature.

The data points with the standard labeling starting with FZ do not fit with fitting parameters given in literature due to two reasons. First, more measurements have to be done in order to improve the statistic. Second, the defects of the deep diffusion process for the thin FZ shows strange behavior even for unirradiated TS.

The measurement results of the change on the depletion voltage are listed in table 5.2. With the irradiated Halfmoons for the CMS upgrade, type inversion can be verified as further test structures were irradiated. The expected type inversion is seen on IV measurements at the sheet TS, as now the n+ in p depletion is possible. The still remaining n type of FZ200N 03 TS 2, which has been irradiated at the low fluency tube W, was also verified at the sheet TS.
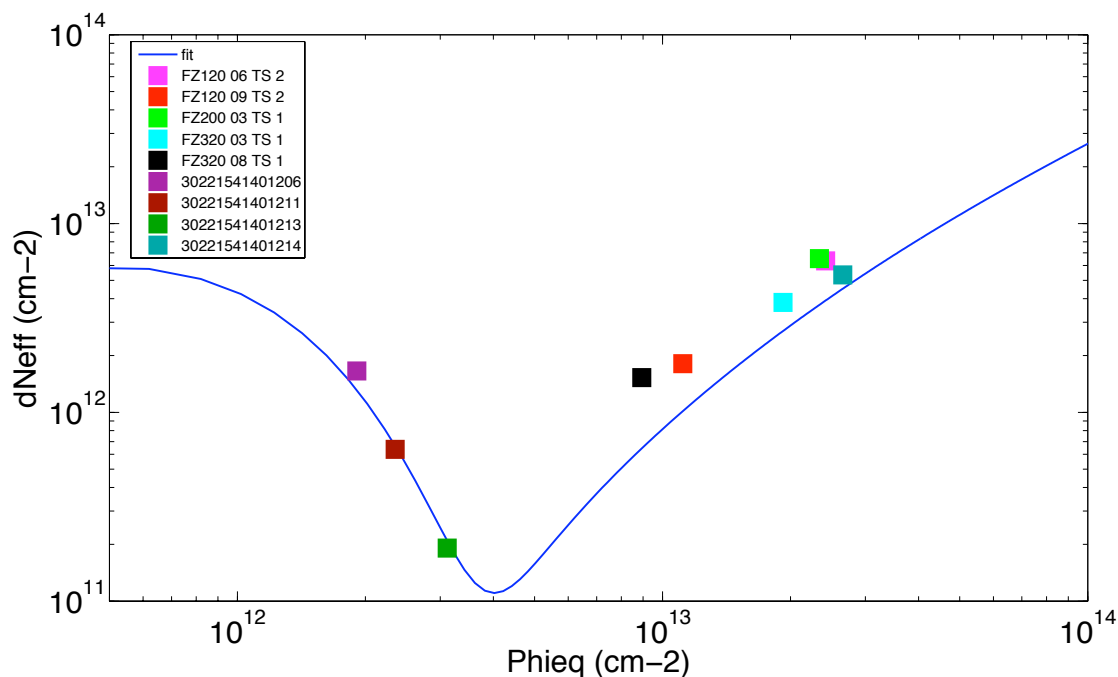

Figure 5.4.: measured change of the effective doping concentration, T=-20°C

TS	tube	fluency	U_{depl}	$U_{depl_{irr}}$
		[cm-2]	[V]	[V]
FZ120N 06 TS 2	TBR3	1.30E15	90	70
FZ120N 09 TS 2	TBR2	4.70E14	90	20
FZ200N 03 TS 1	TBR2	1.18E15	110	200
FZ200N 03 TS 2	W2	1.44E14	120	110
FZ320N 03 TS 1	TBR1	1.04E15	210	300
FZ320N 08 TS 1	TBR1	4.18E14	200	120
30221541401206	TBR5	0.99E14	220	130
30221541401207	W1	0.29E14	220	230
30221541401208	TBR5	1.48E14	220	330
30221541401210	W1	0.43E14	190	95
30221541401211	TBR5	2.47E14	220	50
30221541401213	TBR5	3.46E14	220	15
30221541401214	TBR5	1.85E15	220	420
30221541401215	W1	5.40E14	220	80

Table 5.2.: overview of changes in depletion voltage Udepl, T=-20°C

5.3.3. MOS Irradiation

The extraction of MOS parameters after irradiation is not possible as the significant change of the capacitance is not seen. In figure 5.5 the changes in the CV characteristic depending on different fluence steps are seen. The dotted results correspond to the irradiation in the W tube, the lines to the TBR tube. The results with the same neutron spectrum should be compared.

The higher the fluence the more charge traps are introduced. The MOS capacitance decreases with fluence due to trapped charge carriers. The flatband voltage of unirradiated TS is about 1V compared to one of the irradiated result of about 4V. This higher flatband voltage points to additional oxide charges produced by irradiation.
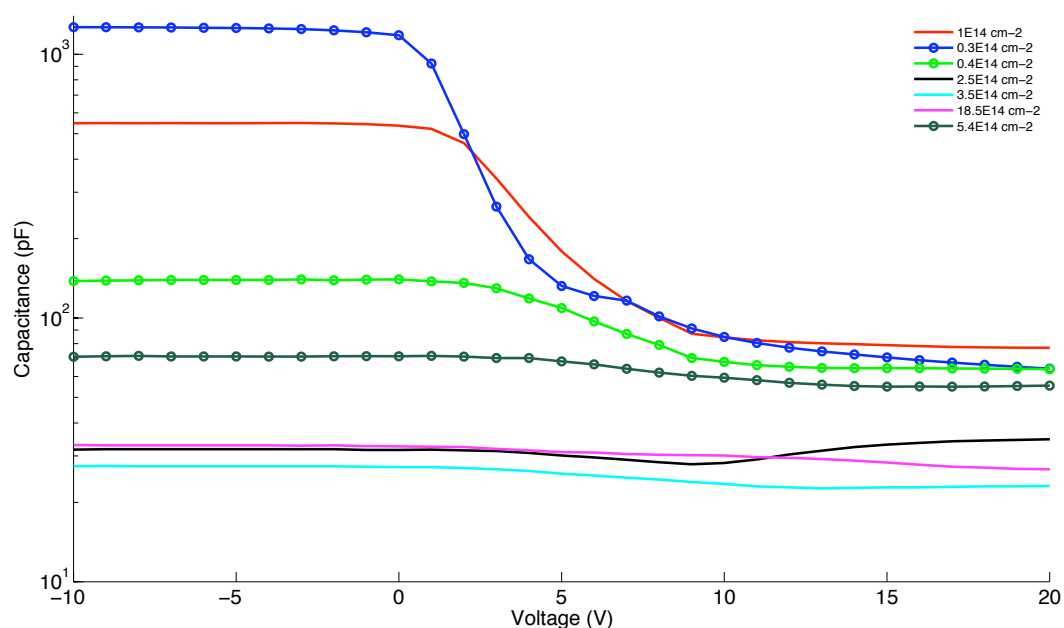

Figure 5.5.: CV mos N, irradiated at different fluxes and neutron spectra, T=-20°C

6. Conclusion

6.1. Summary

Different detector technologies for the high luminosity upgrade of LHC were investigated in this thesis. Before the electrical characterization, the measurement setup had to be improved as it introduced high noise at low temperatures. This required a detailed investigation on noise sources.
Especially when measuring at low temperatures, there are some actions to keep the leakage current low. All equipment from the measurement and cooling system should be in operation, a constant dry air flow should be provided, some time should be waited after re-closing the measurement box and the motor control of the microscope should be switched off.

Although a lot of measurements had been performed the results are not conclusive yet. There are unexpected and strange behaviors where further investigations are needed.
The diodes with the deep diffusion process show an unexpected behavior in terms of the dark current. The saturation in the IV characteristic is missing and thicker test structures have a lower dark current compared to the thinner ones. An additional order of wafers with the physical thickness of 200um and 120um should show expected results.
Although the resistivity values of the bulk are in the expected range for each material compared to the values given from HPK, the CV characteristic of P diodes for MCZ and FZ material is not yet understood.

The different saturation behavior of interstrip measurements was also unexpected. The values within the first voltage steps vary as the strips are not perfectly isolated from each other but the saturated value for the interstrip capacitance depends on the material, e.g. the Epi100 strips are separated after 100V whereas the FZ320 are already isolated at 10V.
The low interstrip resistance values for p type MCZ and thin FZ leads to shorted strips at 20°C. The wave shapes of the MCZ resistance stays constant throughout the voltage ramp whereas the P and Y test structures of the FZ and Epi material have two changes in the interstrip resistance.

The unexpected kink of the p spray MOS structures led to interesting studies of the CV characteristics. The kink only occurs with high ramp rates at room temperature and is always present at low temperatures. The wave shapes do not only depend on the absolute ramp rate value but also differ when using the same absolute ramp rate value with different wait time values and different voltage steps. The CV characteristic also depends on the thickness and the material.

The VIA measurements on p types show a very high statistical deviation whereas the uncertainty of n types is low. The manufacturing process which leads to the unexpected resistivity value of the second metal aluminum sheet test structures is also unknown.

Two measurement results indicate an inhomogeneous process on single wafers. The end capacitances of the interstrip measurements differ for the test structures from the same wafer but have the same absolute value compared to the test structures with the same TS number from different wafers. The same can be said for IV measurements on diodes. The ramp of the dark current over the applied voltage shows more identical results with the same TS number compared to the same wafer number.

The final topic of this thesis is the first attempt to use the reactor at ATI as a new possibility for future irradiation of semiconductor devices. The *Trocken Bestrahlungs Rohr* TBR tube is the best place of irradiation but for lower fluencies the *Weberbestrahlungsrohr* W tube has to be used. The interplay between irradiation time and the thermal power of the reactor is also known for reaching specified fluencies now.

6.2. Outlook

The irradiation campaign within CEC investigates the radiation hardness of the different materials. Neutron irradiation takes place in Ljubljana (Slovenia) and proton irradiation in Karlsruhe (Germany). The used fluence within the campaign is chosen from the expected fluence from CMS. As the fluence depends on the radial distance from the intersection point different irradiation steps are performed. The sequence consists of the irradiation with neutrons, short annealing with measurements, proton irradiation and annealing studies afterwards. The same will be performed with proton irradiation first.

There are two main steps for the future. First, the results presented in this thesis has to be understood in more detail and has to be verified with more statistic. Second, the irradiation investigations need to be focused on the differences in the material and also on the differences of proton and neutron irradiation.

For verifying the Metal Oxide Semiconductor MOS results also more statistic is needed. The irradiation investigations has to be performed for further low fluence steps. The unexpected results of the kink in the CV characteristic of the p spray test structures would need high doping areas in a thicknesses range less than 2um to confirm the calculation.
After the behavior is completely understood for the MOS test structure, the IV behavior at the GCD test structure can be studied in more detail.
For the prospective design of sheet test structures, a bias ring for depleting the implants should be implemented.

The measurement setup in Vienna could be improved in terms of the peltier element cooling. At the moment the used temperature of the cooling liquid SilOil is -10°C. The cooling performance of the existing tubes are not so efficient when the active side of peltier elements reaches -20°C. The SilOil is hygroscopic and absorbs moisture from air which forms ice crystals at low temperatures from time to time. Heating up to temperature higher 100°C boils the water out of the SilOil. The cross section of the tubes has to increase to improve the cooling performance for the peltier elements. Then higher temperatures of the SilOil, e.g. 3°C, could be used for simplifying the setup.

The irradiation at ATI needs more experiences in terms of dosimetry. In this thesis the used Halfmoons led to a high number of uncertainties even before irradiation. The different thicknesses and different processing of the Halfmoon complicated the irradiation studies. The next step is going to be an irradiation study on diodes from the same wafer with the same processing. This results could be compared with the irradiation of the same diodes at Ljubljana.
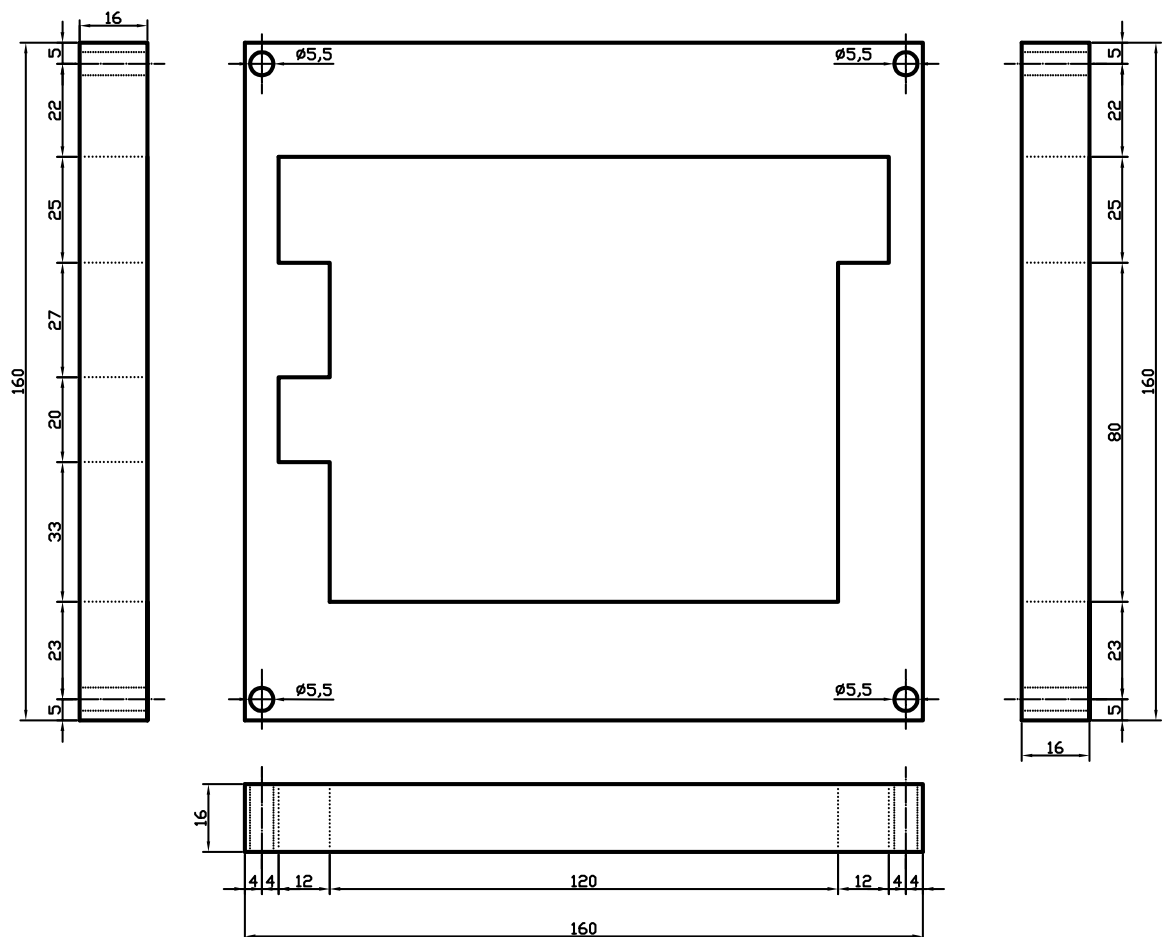
Bibliography

[1] R. Schmidt et al., *Protection of the CERN Large Hadron Collider*, NewJournal of Physics *8* (2006) 290, 2

[2] M. Krammer, http://www.hephy.at/lehre/lehrveranstaltungen/ unterlagen/teilchendetektoren-krammer 2009 7, 8, 10

[3] T. Bergauer, *Process Quality Control of Silicon Strip Detectors for the CMS Tracker*, Diploma Thesis 2004 24, 45, 60

[4] M. Dragicevic, *The New Silicon Strip Detectors for the CMS Tracker Upgrade*, Dissertation 2010 3, 4, 5, 70

[5] M. Moll, *Radiation Damage in Silicon Particle Detectors*, Dissertation 1999 11, 12, 14, 15, 79

[6] A. Junkes, *Influence of radiation induced defect clusters on silicon particle detectors*, Dissertation 2011 12, 13, 14, 38, 39

[7] W. Treberspurg, *Material Analysis of Silicon Strip Sensors*, Diploma Thesis 2011 60, 74

[8] G. Auzinger, *Design of a Cooling Device for the Qualification of Irradiated Silicon Sensors*, Diploma Thesis 2010 3, 17

[9] A. Dierlamm, *Status of Irradiation*, Sensor Meeting Tracker Week 21.7.2011

[10] E. Nicollian, *MOS (Metal Oxide Semiconductor) Physics and Technology*, A Wiley Interscience Publication 1982 69, 72

[11] D. Schroder, *Semiconductor Material and Device Characterization*, A Wiley Interscience Publication 2006 72

[12] *CMS experiment*, http://cms.web.cern.ch/cms/Detector/Designed/index.html 2

[13] *The TRIGA Mark II Reactor*, http://www.ati.ac.at/index.php?id=113 79

[14] *special ceramics*, http://www.bce-special-ceramics.de/hochleistungskeramik/vergleich.php 18
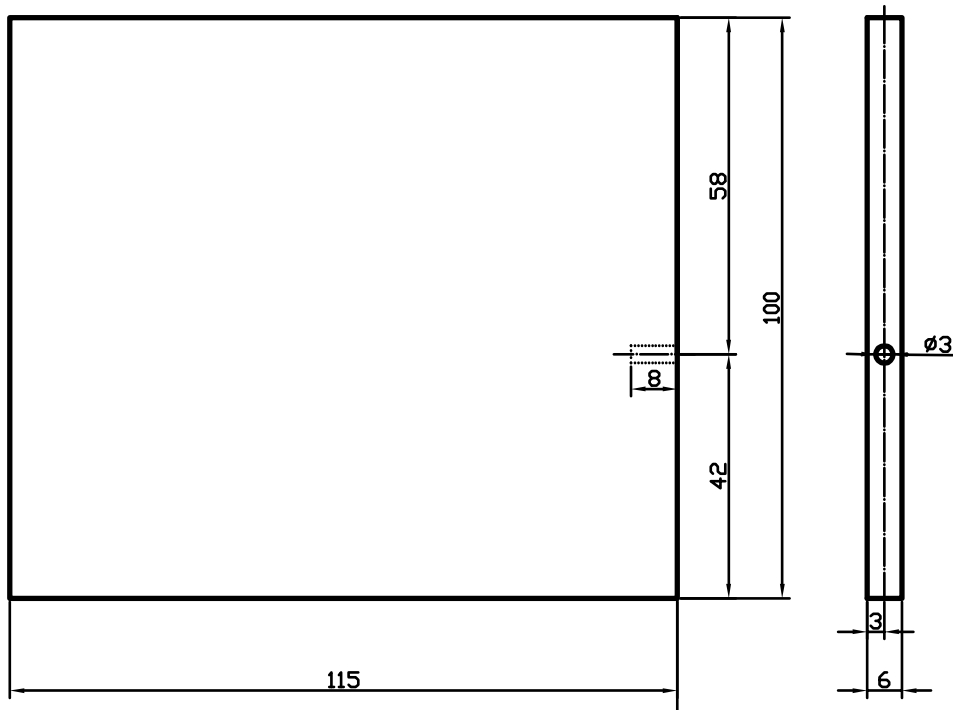
Appendix A.

Appendix

A.1. Drawings

Frame
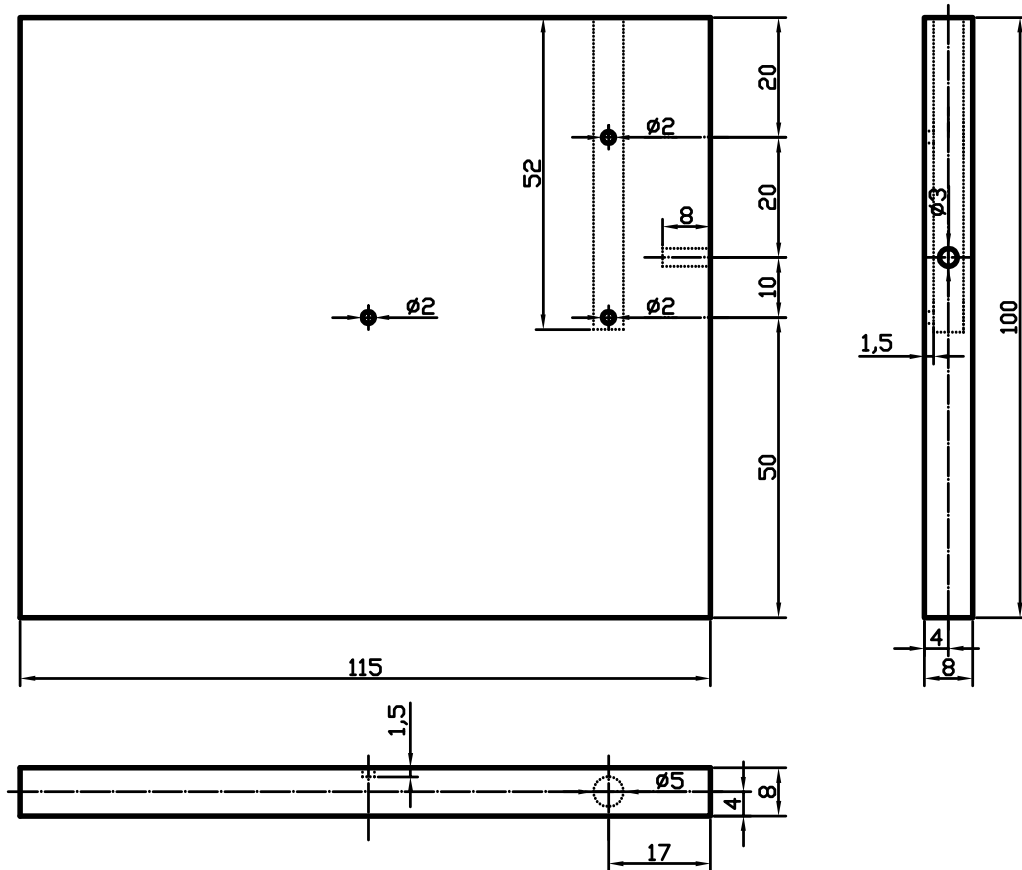Cold Chuck Redesign Maria Bernard-Schwarz, 2011

Figure A.1.: CAD drawing of the new frame

Guard Plate
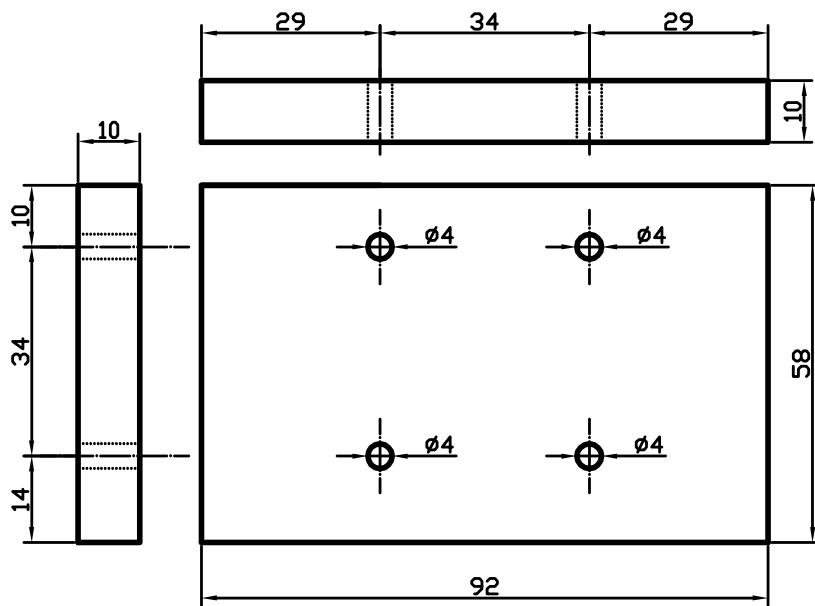Cold Chuck Redesign Maria Bernard-Schwarz, 2011

Figure A.2.: CAD drawing of the new guard plate

Sense Plate

Cold Chuck Redesign Marla Bernard-Schwarz, 2011

Figure A.3.: CAD drawing of the new sense plate

Buck
Cold Chuck Redesign Maria Bernard-Schwarz, 2011

Figure A.4.: CAD drawing of the new buck

A.2. Abbreviations

A.2.1. Physical Constants

$$
\begin{aligned}
e &= 1.6022 \cdot 10^{-19} C & (\textit{unit charge}) \\
\mu_e &= 1400 \, \tfrac{cm^2}{Vs} & (\textit{electron mobility}) \\
\mu_h &= 450 \, \tfrac{cm^2}{Vs} & (\textit{hole mobility}) \\
\\
\varepsilon_0 &= 8.854 \cdot 10^{-14} \tfrac{F}{cm} & (\textit{vacuum relative permittivity}) \\
\varepsilon_{Si} &= 11.8 & (\textit{silicon relative permittivity}) \\
\varepsilon_{Si_{O_2}} &= 3.9 & (\textit{silicon dioxide relative permittivity}) \\
\varepsilon_{Si_3N_4} &= 7.5 & (\textit{silicon nitride relative permittivity})
\end{aligned}
$$

Table A.1.: physical constants

A.2.2. Test Structure Parameter

$$
\begin{aligned}
A_{cv} &= 25.8 \cdot 10^{-2} cm^2 & (\textit{area DIODE and MOS Structure}) \\
A_{cap} &= 199.67 \cdot 10^{-5} cm^2 & (\textit{area CAP Structure}) \\
A_{gcd} &= 191.8 \cdot 10^{-5} cm^2 & (\textit{area GCD Strcuture}) \\
\\
d_{Si_3N_4} &= 50 \cdot 10^{-7} cm & (\textit{assumption for silicon nitride thickness}) \\
\\
implant2 &= 5870 & (\textit{square number for N2,P2,P4}) \\
implant1 &= 2940 & (\textit{square number for N1,P1,P3}) \\
Al2 &= 13758 & (\textit{square number for aluminum 2}) \\
Al1 &= 4916 & (\textit{square number for aluminum 1}) \\
6 &= 606 & (\textit{square number for polysilicon 6}) \\
5 &= 306 & (\textit{square number for polysilicon 5}) \\
4 &= 156 & (\textit{square number for polysilicon 4}) \\
3 &= 453 & (\textit{square number for polysilicon 3}) \\
2 &= 967 & (\textit{square number for polysilicon 2}) \\
1 &= 1860 & (\textit{square number for polysilicon 1})
\end{aligned}
$$

Table A.2.: TS parameter

A.2.3. Text Abbreviations

LHC	...	Large Hadron Collider
SLHC	...	Super Large Hadron Collider
CMS	...	Compact Muon Solenoid
CEC	...	Central European Consortium
HPK	...	Hamamatsu Photonics K.K.
ATI	...	Atominstitut Vienna
TBR	...	high fluency dry irradiation tube (TrockenBestrahlungsRohr)
ZBR	...	wet irradiation tube (ZentralesBestrahlungsRohr)
W	...	low fluency dry irradiation tube (Weberrohr)
SMU	...	Source Measure Unit
IV	...	Current Voltage Ramp
CV	...	Capacitance Voltage Ramp
CINT	...	Interstrip Capacitance
RINT	...	Interstrip Resistance
RR	...	Ramp Rate
RH	...	Relative Humidity
sq	...	Square Number
TS	...	Test Structure
N	...	n type bulk with p^+ strips
P	...	p type bulk with n^+ strips and pstop strip isolation
Y	...	p type bulk with n^+ strips and pspray strip isolation
FZ	...	Floating Zone
MCZ	...	Magnetic Czochralski
Epi	...	Epitaxial
DM	...	Double Metal
Halfmoon	...	set of TS
irr	...	irradiated
TS CAP	...	isolated strip TS (for Coupling Capacitance and Dieelctric Break Down Voltage)
TS CAP DC	...	DC coupled strip TS (for Interstrip Resistance)
TS CAP AC	...	AC coupled strip TS (for Interstrip Capacitance)
TS GCD	...	Gate Control Diode TS
TS MOS	...	Metal Oxide Semiconductor TS
BP	...	BackPlane
HV	...	SMU 237
V	...	SMU 2410
lfLCR	...	lowfrequency LCR meter (100Hz - 100kHz)
LCR	...	LCR meter (75kHz - 30MHz)
N1, N2, N3, N4	...	needle 1, needle 2,needle 3, needle 4

Table A.3.: used abbreviations

A.3. Acknowledgements